

NUMERICAL SIMULATION OF EFFECTS OF CLADDING  
AND SUPERIMPOSED HYDROSTATIC PRESSURE  
ON FRACTURE IN METALS UNDER TENSION

NUMERICAL SIMULATION OF EFFECTS OF CLADDING  
AND SUPERIMPOSED HYDROSTATIC PRESSURE  
ON FRACTURE IN METALS UNDER TENSION

By

XIAOXIAN CHEN, B.A.Sc.

A Thesis

Submitted to the School of Graduate Studies

In Partial Fulfillment of the Requirements

For the Degree

Masters of Applied Science

McMaster University

©Copyright by Xiaoxian Chen, June 2009

Masters of Applied Science  
(Mechanical Engineering)

McMaster University  
Hamilton, Ontario

TITLE: Numerical simulation of effects of cladding and  
superimposed hydrostatic pressure on fracture in metals  
under tension.

AUTHOR: Xiaoxian Chen

SUPERVISOR: Dr. Peidong Wu

NUMBER OF PAGES: xii, 94

## **ABSTRACT**

In this study, detailed numerical works are carried out to investigate cladding and superimposed hydrostatic pressure on fracture in metals under tension by using finite element software ABAQUS/Explicit. It is concluded that both cladding and superimposed hydrostatic pressure delay void nucleation and void growth, which results in increasing fracture strain in metals under tension.

The influence of cladding on delaying fracture in metals under tension is numerically studied by employing Gurson-Tvergaard-Needleman (GTN) damage model. It is found that cladding has a significant effect on enhancement in materials' ductility due to the fact that cladding increases necking strain which in turn delays the void nucleation and growth. Topological arrangement of cladding in axisymmetric tensile round bars shows no noticeable effect on necking but significantly affects fracture strain.

The influence of superimposed hydrostatic pressure is numerically investigated on sheet metals under plane strain tension by using GTN damage model. It is found that superimposed hydrostatic pressure has no noticeable effect on necking but significantly delays fracture initiation due to the fact that superimposed hydrostatic pressure delays or completely eliminates the nucleation, growth and coalescence of microvoids or microcracks.

## ACKNOWLEDGEMENTS

For development of my research work and writing of this thesis, I would like to express my sincerest gratitude to my supervisor Dr. Wu for your patient instruction, insightful advice and continuous encouragement. Most importantly, you teach me how to think, logically and innovatively.

I would also like to thank Dr. Embury from Material Science department of McMaster University, for several valuable discussions and enlightening suggestions.

To my colleagues in finite element research group, Nick Trutwin, Huamiao Wang, Jing Peng and Dr. Bin Chen, I would like to thank all of you for your support and selfless help.

Last but not the least, I will thank my girlfriend Hanting and my parents. Without your consistent love and support, I will not be where I am today. I am always in your debt.

Many thanks to Novelis Inc., NSERC and McMaster University for research funding and financial support.

## TABLE OF CONTENTS

ABSTRACT.....	iii
ACKNOWLEDGEMENTS.....	iv
TABLE OF CONTENTS.....	v
LIST OF FIGURES.....	vii
Chapter 1 Introduction.....	1
1.1 Laminated metal composites.....	1
1.1.1 Overview.....	1
1.1.2 Some examples of laminated structures.....	1
1.1.3 Processing techniques.....	5
1.2 Novelis Fusion Technology.....	6
1.2.1 Overview.....	6
1.2.2 Manufacturing process.....	7
1.2.3 Experimental results on the interfacial strength of composite materials ..	8
1.2.4 Applications.....	9
1.3 Effects of superimposed hydrostatic pressure on fracture.....	11
1.3.1 Overview.....	11
1.3.2 Experimental work.....	11
1.3.3 Numerical work.....	15
1.4 Thesis outline.....	16
Chapter 2 Gurson damage model.....	17
2.1 Damage models.....	18
2.1.1 Macroscopic damage models.....	18
2.1.2 Microscopic damage models.....	20
2.2 Gurson damage model.....	21
2.2.1 Original form of Gurson yield function.....	21
2.2.2 Gurson-Tvergaard-Needleman (GTN) damage model.....	23
2.3 Recent development of the Gurson model.....	25
2.3.1 A dilatational plasticity theory for viscoplastic materials.....	26
2.3.2 Modification of Gurson model for shearing effect in ductile fracture....	26
2.4 Gurson model in finite element software ABAQUS.....	29

Chapter 3 Enhanced ductility in clad round tensile bars.....	30
3.1 Introduction.....	30
3.2 Problem formulation and method of solution .....	31
3.3 Results and discussions.....	33
3.4 Summary .....	51
Chapter 4 Enhanced ductility in clad tensile sheets.....	52
4.1 Introduction.....	52
4.2 Problem formulation and method of solution .....	53
4.3 Results and discussions.....	55
4.4 Summary .....	68
Chapter 5 Effects of superimposed hydrostatic pressure on fracture in tensile sheets	69
5.1 Introduction.....	69
5.2 Problem formulation and method of solution .....	71
5.3 Results and discussions.....	73
5.4 Summary .....	87
Chapter 6 Conclusions and future work.....	88
BIBLIOGRAPHY.....	89

## LIST OF FIGURES

Figure 1.1: Laminated metal composites in ancient times. (a) Achilles' shield, (b) Indonesian Kris. [Wadsworth et al. (2000)].....	2
Figure 1.2: Large laminated metal pipes manufactured in the Ukraine. (a) Overall view, (b) Sheet configuration. [Wadsworth et al. (2000)].....	3
Figure 1.3: Laminated structures of Beijing Aquatics Center. (a) Overview, (b) ETFE cladding.....	3
Figure 1.4: Charpy V-notch impact test for 12-layer laminated composite of UHCS/mild steel in crack arrester orientation and for mild steel and UHCS monolithic steels. [Wadsworth et al. (2000)] .....	4
Figure 1.5: Laminated metal composite target impacted by hardened steel projectile travelling at 400m/s. [Wadsworth et al. (2000)] .....	4
Figure 1.6: Schematic diagram of a new method for casting composite ingots (Novelis Fusion Technology). [Alcan (WO 2004/112992 A3)] .....	8
Figure 1.7: Microstructure of AA1200/AA2124 composite material. [Wagstaff et al. (2006)].....	9
Figure 1.8: (a) Tensile test of AA1200/2124; (b) Bending test of AA4045/AA5754 [Wagstaff et al. (2006)] .....	9
Figure 1.9: New BMW 7-series door incorporating Novelis Fusion Technology. [Novelis Fusion - BMW 7 series] .....	10
Figure 1.10: Schematic diagram of a typical fluid-based high pressure deformation apparatus. [Lewandowski and Lowhaphandu (1998)].....	12
Figure 1.11: Schematic diagram of a typical gas-based high pressure deformation apparatus. [Lewandowski and Lowhaphandu (1998)].....	12
Figure 1.12: The appearance of the fractured tensile bars tested under applied pressure, Kao et al. (1990). .....	13
Figure 1.13: High-Fe5754 sample tested at various superimposed hydrostatic pressures. [Gimple et al. (2001)].....	14
Figure 2.1: Yield surface dependence on the hydrostatic tension for various void volume fractions $f$ .....	22
Figure 2.2: Schematic diagram of void nucleation, void growth and void coalescence	



.....	23
Figure 2.3: Deformation sequence for a copper sample with a rectangular array of holes oriented at (a) 15° (b) 45° with respect to the tensile axis. I(a) and I(b): Underformed sample; II(a) and II(b): Sample right at the coalescence event; III(a): Coalescence occurring by internal necking between the voids; III(b): Strong shearing between the voids and its effect on the shape of the holes. [Weck et al. (2006)].....	27
Figure 3.1: 3D view of a bilayer clad round bar .....	31
Figure 3.2: Schematic representation of a round tensile bar with a ductile cladding ring. (a) Undeformed state, and (b) deformed state. ....	33
Figure 3.3: Uniaxial stress and strain curves of the core and clad materials. ....	34
Figure 3.4: Mesh A with 28×42 quadrilateral elements (28 in the radius direction and 42 in the axial direction), each built up with four linear triangular elements (CAX3 in ABAQUS/Explicit). ....	35
Figure 3.5: Predicted normalized force $F^*$ and tensile strain $\varepsilon = \ln(1 + U/L_0)$ curve for a round bar of the core material ( $\Gamma = 0$ ).....	37
Figure 3.6: Predicted normalized minimum cross-sectional area at the middle-plane $A^*$ and tensile strain $\varepsilon = \ln(1 + U/L_0)$ curve for the round bar of the core material ( $\Gamma = 0$ ).....	37
Figure 3.7: Deformed meshes at various deformation stages for the round bar of the core material ( $\Gamma = 0$ ). (a) $\varepsilon = 0.227$ , (b) $\varepsilon = 0.262$ , (c) $\varepsilon = 0.268$ , and (d) $\varepsilon = 0.271$ . ....	39
Figure 3.8: Predicted normalized force $F^*$ and tensile strain $\varepsilon = \ln(1 + U/L_0)$ curve for a round bar of the clad material ( $\Gamma = 100\%$ ). ....	40
Figure 3.9: Predicted normalized minimum cross-sectional area $A^*$ at the middle-plane and tensile strain $\varepsilon = \ln(1 + U/L_0)$ curve for the round bar of the clad material ( $\Gamma = 100\%$ ).....	40
Figure 3.10: Deformed meshes at various deformation stages for the round bar of the clad material ( $\Gamma = 100\%$ ). (a) $\varepsilon = 0.405$ , (b) $\varepsilon = 0.407$ , (c) $\varepsilon = 0.408$ , and (d) $\varepsilon = 0.410$ .....	41

Figure 3.11: Predicted normalized force $F^*$ and tensile strain $\varepsilon = \ln(1 + U/L_0)$ curves for round tensile bars with various cladding thickness ratio $\Gamma$ .....	42
Figure 3.12: Predicted normalized minimum cross-sectional area $A^*$ at middle-plane and tensile strain $\varepsilon = \ln(1 + \Delta L/L_0)$ curves for round tensile bars with various cladding thickness ratio $\Gamma$ .....	43
Figure 3.13: Predicted strain to necking $\varepsilon_u$ for round tensile bars with various volume fraction of cladding $\Lambda$ .....	44
Figure 3.14: Predicted crack path of the fractured tensile bars with various thickness fraction of cladding $\Gamma$ .....	45
Figure 3.15: Predicted crack profile of fractured tensile bars with various thickness fraction of cladding $\Gamma$ . Thin black lines are based on Mesh B while thick red lines are calculated from Mesh C. ....	46
Figure 3.16: Predicted normalized fracture strain $\varepsilon_f^*$ in round tensile bars with various volume fraction of cladding $\Lambda$ .....	46
Figure 3.17: Predicted hydrostatic stress $\sigma_H$ at the centre of neck in round tensile bars with various thickness fraction of cladding $\Gamma$ .....	47
Figure 3.18: Predicted triaxiality $T = \sigma_H/\sigma_e$ at the centre of neck under various thickness fraction of cladding $\Gamma$ .....	48
Figure 3.19: Predicted void volume fraction $f$ at the centre of neck in round tensile bars with various thickness fraction of cladding $\Gamma$ .....	48
Figure 3.20: Predicted effect of cladding ring position $R_i/R_0$ on fracture strain $\varepsilon_f$ in round tensile bars with fixed volume fraction of cladding $\Lambda = 37.6\%$ . The inserted small figure shows the topological arrangement of the cladding ring (shaded area). ....	50
Figure 3.21: Predicted effect of cladding ring position $R_i/R_0$ on necking strain $\varepsilon_u$ in round tensile bars with fixed volume fraction of cladding $\Lambda = 37.6\%$ .....	50
Figure 4.1: Schematic diagram of a sheet under plane strain tensile loading (a) Undeformed state; (b) Deformed state.....	54
Figure 4.2: Uniaxial stress and strain curves of the core and clad materials. ....	55
Figure 4.3: Mesh B with $90 \times 60$ quadrilateral elements (90 in the $X$ -direction and 60 in	

the $Y$ -direction), each built up with four linear triangular elements (CPE3 in ABAQUS/Explicit); for bilayer baseline case, 48 in core layer and 12 in clad layer in the $Y$ -direction.....	57
Figure 4.4: Normalized tensile force $F^*$ and true strain $\varepsilon$ curve; Crack formation in mono-layer sheet of core material ( $n=0.1$ ); Mesh B.....	58
Figure 4.5: Normalized minimum cross-sectional area $A^*$ and true strain $\varepsilon$ curve; Tensile strains at various stage I, II, III, IV and V are 0.118, 0.122, 0.126, 0.127 and 0.128, respectively; Mesh B.....	58
Figure 4.6 Predicted normalized force $F^* = F / (\sigma_{y\_core} \times A_0)$ and tensile strain $\varepsilon = \ln(1 + \Delta L / L_0)$ curve for monolayer sheet of core material ( $n=0.1$ ). ....	60
Figure 4.7: Predicted normalized minimum cross-sectional area $A^* = A_{min} / A_0$ and tensile strain $\varepsilon$ curve for monolayer sheet of core material ( $n=0.1$ ).....	60
Figure 4.8: Predicted normalized force $F^* = F / (\sigma_{y\_clad} \times A_0)$ and tensile strain $\varepsilon$ curve for monolayer sheet of clad material ( $n=0.2$ ).....	61
Figure 4.9: Predicted normalized minimum cross-sectional area $A^*$ and tensile strain $\varepsilon$ curve for monolayer sheet of clad material ( $n=0.2$ ). ....	61
Figure 4.10: Predicted crack shapes of fractured tensile sheets by using different meshes.....	62
Figure 4.11: Predicted normalized force $F^* = F / (A_0^{core} \times \sigma_y^{core} + A_0^{clad} \times \sigma_y^{clad})$ and tensile strain $\varepsilon$ curve for various thickness fraction of cladding $\Gamma$ by using Mesh B.....	63
Figure 4.12: Predicted normalized minimum cross-sectional area $A^*$ and tensile strain $\varepsilon$ curve for various thickness fraction of cladding $\Gamma$ by using Mesh B.....	64
Figure 4.13: Predicted uniform strain and thickness fraction of cladding $\Gamma$ curve. ...	65
Figure 4.14: Predicted crack formation under various thickness fraction of cladding $\Gamma$ curve by using Mesh B. ....	66
Figure 4.15: Predicted crack formation under various thickness fraction of cladding $\Gamma$ curve by using Mesh D. ....	67
Figure 4.16: Predicted gained fracture strain $\varepsilon_f^*$ and thickness fraction of cladding $\Gamma$	

curve.....	68
Figure 5.1: The appearance of the fractured tensile AA5754-O sheets under applied pressure, Gimple (2001).....	70
Figure 5.2: Schematic diagram of a sheet under plane strain tensile loading (a) Undeformed state; (b) Deformed state.....	72
Figure 5.3: Mesh A with 90×60 quadrilateral elements (90 in the X-direction and 60 in the Y-direction), each built up with four linear triangular elements (CPE3 in ABAQUS/Explicit).....	74
Figure 5.4: Predicted normalized force $F^* = F/(\sigma_y A_0)$ and tensile strain $\varepsilon = \ln(1 + \Delta L/L_0)$ curve for the monolayer sheet under atmospheric pressure ( $p = 0$ ).....	75
Figure 5.5: Predicted normalized minimum cross-sectional area $A^* = A_{min}/A_0$ and tensile strain $\varepsilon = \ln(1 + \Delta L/L_0)$ curve for the monolayer sheet under atmospheric pressure ( $p = 0$ ).....	76
Figure 5.6: Predicted crack evolution of monolayer sheet by using Mesh A and Mesh B under atmospheric pressure $p = 0$ .....	77
Figure 5.7: Predicted crack evolution of monolayer sheet by using Mesh A under various superimposed hydrostatic pressure.....	78
Figure 5.8: Predicted crack evolution of monolayer sheet by using Mesh B under various superimposed hydrostatic pressure.....	79
Figure 5.9: Predicted shear bands under various superimposed hydrostatic pressures before fracture by using Mesh A.....	80
Figure 5.10: Predicted normalized applied force $F^* = F/(\sigma_y A_0)$ and tensile strain $\varepsilon = \ln(1 + \Delta L/L_0)$ curves for monolayer sheet under superimposed hydrostatic pressure $p = -\alpha\sigma_y$ by using Mesh B.....	82
Figure 5.11: Predicted normalized minimum area $A^* = A_{min}/A_0$ and tensile strain $\varepsilon = \ln(1 + \Delta L/L_0)$ curves for monolayer sheet under superimposed hydrostatic pressure $p = -\alpha\sigma_y$ by using Mesh B.....	82

Figure 5.12: Predicted hydrostatic stress  $\sigma_H$  at the centre of the neck under superimposed hydrostatic pressure  $p = -\alpha\sigma_y$  by using Mesh B. ....84

Figure 5.13: Predicted void volume fraction  $f$  at the centre of the neck under superimposed hydrostatic pressure  $p = -\alpha\sigma_y$  by using Mesh B. ....84

Figure 5.14: Predicted contour plots of effective plastic strain and void volume fraction by using Mesh A. ....85

Figure 5.15: Predicted effect of superimposed hydrostatic pressure  $p = -\alpha\sigma_y$  on fracture strain  $\varepsilon_f$ . ....86

Figure 5.16: Predicted uniform strain under various superimposed hydrostatic pressure  $p = -\alpha\sigma_y$ . ....87

## Chapter 1 Introduction

### 1.1 Laminated metal composites

#### 1.1.1 Overview

In industry, there is an increasing demand on materials to serve as a multifunctional design role. This requires making tradeoffs in material properties as has been done with different alloying elements and clad materials. Laminated metal composites (LMC) are of the most interest for applications in many diverse fields in that they combine properties of their component parts to obtain composite properties which may be new or unique or they make it easier and less costly to obtain certain properties than is possible with monolithic materials. Laminated metal composites consist of alternating metal or metal containing layers bonded together with discrete or “sharp” interfaces. These are distinguished from graded materials which have diffuse interfaces. Laminated metal composites can dramatically improve many properties including fracture toughness, fatigue behavior, impact behavior, wear, corrosion, and damping capacity or provide enhanced formability or ductility for otherwise brittle materials. Numerous investigations have examined the mechanical behavior of laminated metal composites and were reviewed by Lesuer et al. (1996), Wadsworth et al. (2000), Vermeeren (2003), Botelho (2006), Kim and Yu (1997) and Alexander and Bernstein (1984). Laminated metal composites have a wide commercial market. Their potential applicability is still accelerating. In this chapter, several interesting historical applications of laminated metal composites will be presented, followed by a brief description of conventional LMC processing and newly released “Novelis Fusion Technology”.

#### 1.1.2 Some examples of laminated structures

The earliest known reference of laminated metal composites is probably that of Achilles’ shield recorded in “The Iliad of Homer”, in which Achilles’ shield is described as having five layers: bronze/tin/gold/tin/bronze (see Fig. 1.1a). During combat, the superior performance of the laminate was demonstrated by the fact that Aeneas’ bronze spear penetrated the first two layers but stuck in the gold layer.

Indonesian krisses are another famous example of laminated metal composites that are usually forged to have repetitive curves along their length. Fig. 1.1b shows a typical Indonesian kris made with composite of nickel-iron and plain carbon steel.

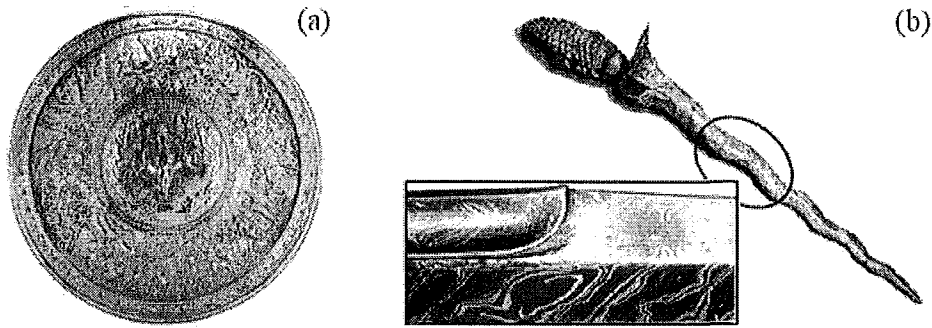


Figure 1.1: Laminated metal composites in ancient times. (a) Achilles' shield, (b) Indonesian Kris. [Wadsworth et al. (2000)]

Modern laminated metal composites are manufactured for a number of reasons but mainly for an improvement in mechanical properties and cost efficiency. Perhaps the first widely practical application is that developed in the former Soviet Union for large pipes, pressure vessels and gun tubes for fracture critical control. In all these applications, internal interfaces between layers limit crack propagation through several different mechanisms. Fig. 1.2 shows the laminated structure of large pipes manufactured by the Paton Welding Institute in the Ukraine. Thin sheets of steel are tightly wrapped together and welded to form concentric shells that resist through-thickness crack propagation. In addition to the obtained through-thickness toughness from concentric shells, toughness in the longitudinal direction of the pipe is also achieved by introducing periodic circumferential segments.

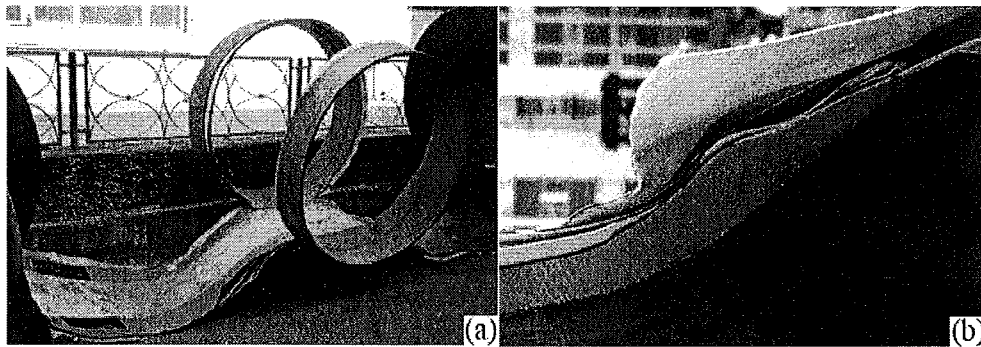


Figure 1.2: Large laminated metal pipes manufactured in the Ukraine. (a) Overall view, (b) Sheet configuration. [Wadsworth et al. (2000)]

Laminated structures are developed for those applications in many diverse fields. Polymer-metal laminated structures are becoming increasingly more popular in architecture, electronics and other industries. Fig. 1.3a shows the Beijing Aquatics Center used in the 2008 Olympic Games. It is the largest ETFE (Ethylene Tetrafluoroethylene) clad structure in the world with over  $100,000m^2$  of ETFE pillows that are only 0.001 inch in total thickness. ETFE cladding (see Fig. 1.3b) is a fluoropolymer that was designed to have high corrosion resistance and high strength over a wide temperature range and allows more light and heat penetration than traditional glass. Numerical investigations of ductility in metal-polymer structure have been successfully studied by recent researchers [Li et al. (2006) and Xue et al. (2007)].

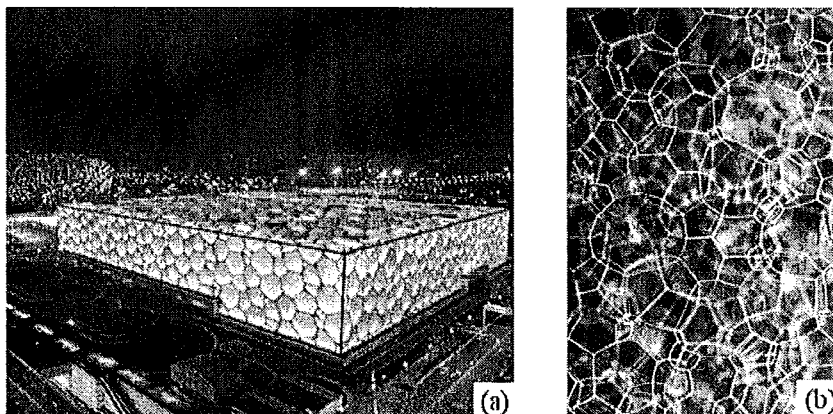


Figure 1.3: Laminated structures of Beijing Aquatics Center. (a) Overview, (b) ETFE cladding.



Moreover, the following impact tests show how laminated structures enhance the fracture toughness. Fig. 1.4 shows that laminated composite exhibits a very high notch impact resistance in Charpy V-notch impact test. Fig. 1.5 presents the ballistic impact of laminate plates that can increase the amount of energy absorbed during impact and thus improve the materials resistance to penetration and perforation.

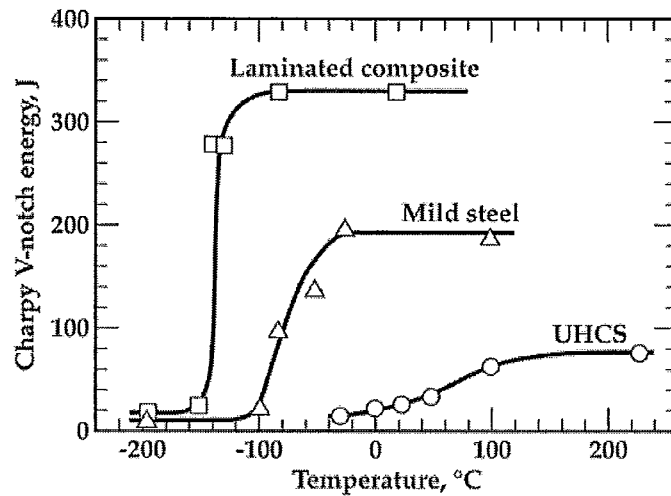


Figure 1.4: Charpy V-notch impact test for 12-layer laminated composite of UHCS/mild steel in crack arrester orientation and for mild steel and UHCS monolithic steels. [Wadsworth et al. (2000)]

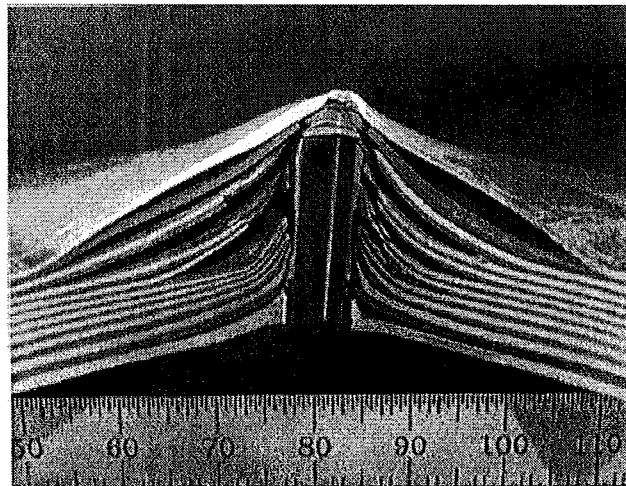


Figure 1.5: Laminated metal composite target impacted by hardened steel projectile travelling at 400m/s. [Wadsworth et al. (2000)]

### 1.1.3 Processing techniques

The processing of laminated metal composites can be roughly categorized as bonding techniques and deposition techniques. Bonding techniques usually have solid state component materials bonded together at the interfaces, which could be further classified into several subgroups, for instance, adhesive bonding, melt bonding, infiltration, diffusion bonding, reaction bonding and deformation bonding. Deposition techniques usually form layers of component materials by atomic or molecular scale transport of the component materials, for example, in sputtering, evaporation, chemical or physical vapor deposition, electroplating, or spray deposition. Particularly, spray deposition techniques involve direct deposition of molten metals of the component materials into a laminate form. In industry, metal clad laminate structures draw a lot of attention. Clad metals are usually produced by bonding techniques such as diffusion bonding and deformation bonding. More specifically, pressing, rolling, explosion and coextrusion deformation bonding techniques are employed in industrial processing. The roll bonding technique is the most economic and productive manufacturing process for large size flat clad metal sheets and foils. In the conventional roll bonding manufacturing process, two or more sheets, plates, or strips of metals/alloys are stacked together and passed through a pair of rolls until proper deformation has been achieved to form a bond between interfaces. Generally there are two types of roll bonding: hot roll bonding and cold roll bonding. Hot roll bonding is a process that involves external heating, while no external heat is applied during cold roll bonding. Cold roll bonding has several advantages over hot roll bonding such as a more uniform individual layer thickness ratio, good surface quality and lower cost [Chen et al. (2005)]. However, roll bonding techniques usually produce laminate metal composites with some defects which can lead to such problems as increased susceptibility to delamination. A new processing technique for manufacturing laminate metal composites “Novelis Fusion Technology” was developed in Novelis Inc. in 2006 and will be introduced in the next section.

## 1.2 Novelis Fusion Technology

### 1.2.1 Overview

With the invention of the electrolytic process in 1886, the manufacturing of aluminum became economically feasible for the first time. By 1938, conventional direct chill casting (DC) allowed aluminum to make its first serious incursion into specialized steel applications and continuous casting technologies of the 1950s further brought aluminum into full and direct competition with steel sheet in many applications. Continuing this trend in 2006, Novelis Fusion Technology, a new innovative method of direct chill casting, opened the door to new, premium applications for aluminum, increasing the demand for aluminum products. In fact, it is forecasted that the world aluminum consumption is projected to grow by an average of 6% per year, to 52.4 million tons approximately by 2013 [ABARE Data]. This is due, in large part, to the weight savings offered by aluminum over steel and with the introduction of fusion technology. This demand can only continue to increase.

Aluminum sheet combined with small quantities of other elements such as copper, manganese, silicon, magnesium etc. (known as aluminum alloy) highly improves its strength and formability. However, these elements might influence the quality of the alloy in some other aspects; For example magnesium is a highly reactive metal that will oxidize the product's surface and diminish its quality. Therefore, single-alloy sheet products appear unable to fulfill the combination of mechanical properties and high surface quality. One alternative is to clad another metal layer onto the single-alloy sheet, yielding the combination of properties from the two alloys. However, conventional aluminum cladding techniques (e.g. roll bonding) have three major drawbacks in manufacturing: 1) Traditional cladding processes are very costly and labor-intensive; 2) Oxidation between layers causes product imperfections; 3) Choices of clad/core alloy combinations are extremely limited. Excitingly, the newly released Novelis Fusion Technology is able to overcome all these drawbacks. Compared to conventional aluminum cladding techniques, Novelis Fusion Technology has the following three advantages: 1) Novelis Fusion Technology is able to simultaneously cast multiple alloy layers into a

single aluminum rolling ingot, which makes the production of multi-alloy aluminum ingots commercially achievable; 2) Perfect metallurgical bonds between layers are attainable; 3) Extensive alloy combinations are permitted and obtainable.

### 1.2.2 Manufacturing process

The process of manufacturing clad alloys by Novelis Fusion Technology will be briefly introduced in this section. Fig. 1.4 shows the apparatus for the casting of a composite metal ingot comprised of two separately formed layers. An open ended annular mould has a feed end and an exit end and divider wall to divide the feed end into two separate feed chambers. The first alloy liquid stream is fed into the first chamber. The body of the first alloy liquid stream gradually cools so that a self-supporting surface is generated and adjacent the lower end of the divider wall, which forms a semi-solid zone. Into the second feed chamber is fed a second alloy liquid flow having a lower liquidus temperature than the first alloy. A semi-solid zone is also formed when the second alloy liquid flow cools down. The upper surface of the second alloy liquid flow is maintained at a position below the lower end of the divider wall. Simultaneously, the temperature of the self-supporting surface is maintained between the liquidus and solidus temperature of the first alloy when the surface of the second alloy liquid flow contacts this self-supporting surface. The interface layer between the two alloys is then reheated to between the liquidus and solidus temperatures. Two alloy streams are thus jointed together due to this very strong interface layer. It is noted that this apparatus is also able to cast more than a layer composite metal by introducing more feed chambers.

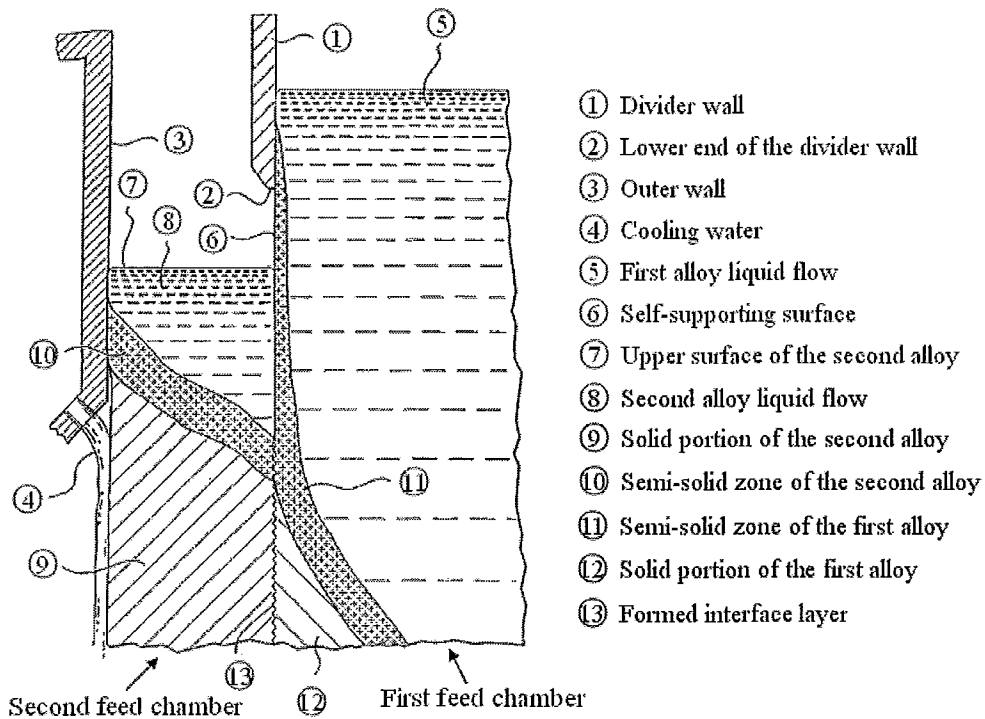


Figure 1.6: Schematic diagram of a new method for casting composite ingots (Novelis Fusion Technology). [Alcan (WO 2004/112992 A3)]

### 1.2.3 Experimental results on the interfacial strength of composite materials

One of the most significant achievements that Novelis Fusion Technology has obtained is for casting composite ingots a substantially continuous and strong metallurgical bond between alloy layers. Several mechanical experiments were calculated for testing the strength of the fusion bond between alloys. Fig. 1.5 shows the microstructure of the AA1200/AA2124 composite material. It is observed that the interface appears to be well bonded, planar and extremely clean, with little evidence of porosity.

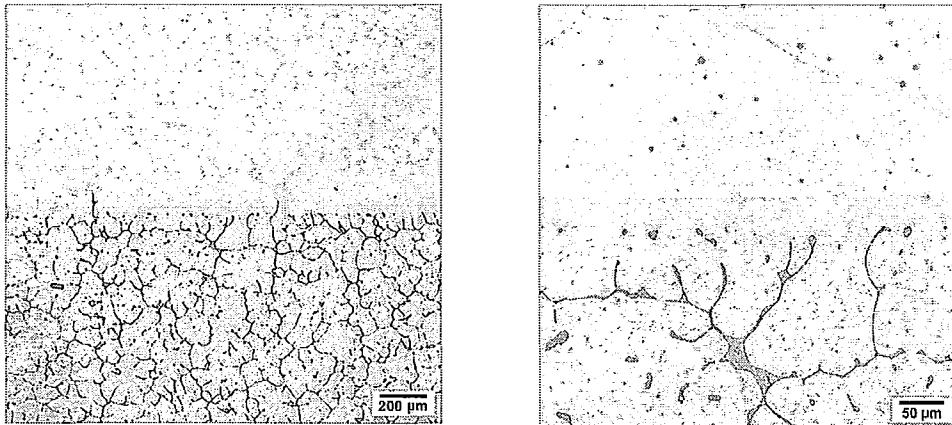


Figure 1.7: Microstructure of AA1200/AA2124 composite material. [Wagstaff et al. (2006)]

Figure 1.6a presents a composite tensile sample made of two aluminum alloys. The interface is marked for clarity. The experiment shows that tensile failure occurs in the lower strength AA1200 while the interface remains sound. Another way of investigating the strength of the interface is by bending. It is demonstrated in Fig. 1.6b that the crack propagates into the core alloy rather than producing extensive delamination of the interface during bending in an AA4045/AA5754 composite.

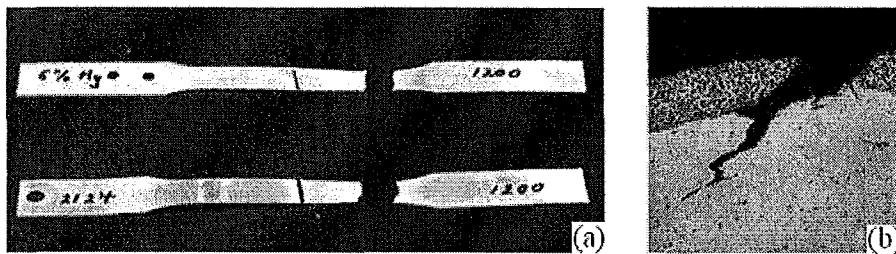


Figure 1.8: (a) Tensile test of AA1200/2124; (b) Bending test of AA4045/AA5754 [Wagstaff et al. (2006)]

#### 1.2.4 Applications

One of the recent successful applications of Novelis Fusion Technology is in the BMW 7-series door inner panels. There are two major challenges BMW faced in their door inner design for the 7-series vehicles. The first challenge was that high deep-drawing capability is required for the door design which can be met by only a few single alloys. However, these alloys do not have the necessary corrosion

resistance. The other challenge was to incorporate a window frame in the door design to decrease door weight. The traditional solution was to do away with the window-frame to avoid multi-part assembly which is substantially cost inefficient however results in a heavier door. Novelis Fusion Technology offered a unique solution for BMW by producing composite alloys with the desired requirements in terms of sufficient elongation performance and corrosion resistance, allowing BMW to design a one piece door inner including a window frame (see Fig. 1.7).

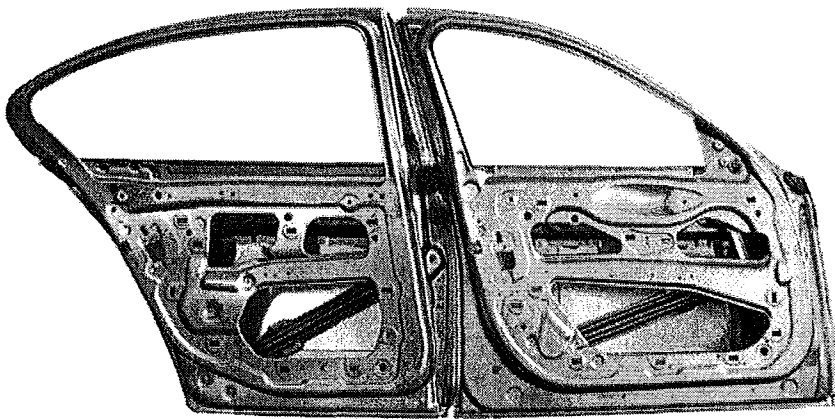


Figure 1.9: New BMW 7-series door incorporating Novelis Fusion Technology.  
[Novelis Fusion - BMW 7 series]

Besides the automotive sheet with both strength and improved formability to enable new design options, there are some other examples of potential applications for Novelis Fusion Technology: 1) Architectural applications with a superior surface finish and enhanced strength; 2) Household appliances with a variety of attractive finishes and better dent resistance; 3) Underground pipes with maximum corrosion resistance combined with high strength; 4) Rail cars with high load-carrying capacity and better wear resistance; 5) Electronics cases that are highly durable and feature a high-tech appearance; 6) Boat hulls with enhanced corrosion resistance without compromising strength.

### 1.3 Effects of superimposed hydrostatic pressure on fracture

#### 1.3.1 Overview

The pioneering research work was done by Bridgeman who documented the influence of superimposed hydrostatic pressure on various monolithic metals in large plastic flow and fracture [Bridgeman (1952)]. Following Bridgeman's work, many researchers [Pugh and Green (1964), French et al. (1973), French and Weinrich (1975), Weinrich and French (1976), Brownrigg et al. (1983), Korbel et al. (1984), Spitzig and Richmond (1984), Ashby et al. (1985), Kao et al. (1989,1990), Liu and Lewandowski (1993), Gimple et al. (2001), Wu et al. (2009), Peng et al. (2009)] have developed extensive investigations on how superimposed hydrostatic pressure affects the mechanical behavior of various monolithic materials, most of which were reviewed by Lewandowski and Lowhaphandu (1998). The general conclusion is that the ductility of materials is considerably increased under a superimposed hydrostatic pressure. However, there were reported some exceptions by researchers that ductility of some materials are not affected by superimposed hydrostatic pressure [Bridgeman (1953)] or even decreased [Hu (1956)]. In this section, some important experimental work of superimposed hydrostatic pressure on round tensile bars and tensile sheets will be summarized. Recent numerical work on the corresponding topics will be included as well.

#### 1.3.2 Experimental work

Substantial experiments have been designed for studying the influence of superimposed hydrostatic pressure on the mechanical behavior (e.g. ductility) of monolithic materials. High pressure mechanical testing is usually conducted using high pressure media including liquids and gases. Fig. 1.8 shows the schematic diagram of a typical oil-based high pressure deformation apparatus, in which mechanical testing with superimposed hydrostatic pressure is able to be conducted. The specimen is typically inserted into the load train assembly, followed by pressurization of the fluid (e.g. oil), and the subsequent tension testing of the specimen at the desired level of superimposed hydrostatic pressure. In the tests, the high pressure fluid has access to all surfaces of the specimen. Gas-based systems as



schematically shown in Fig. 1.9 typically utilize a pressure intensifier to generate pressure that is contained within a multi-walled pressure vessel. In gas-based systems, pressure fluctuations during mechanical testing are much less than those of the oil-based systems.

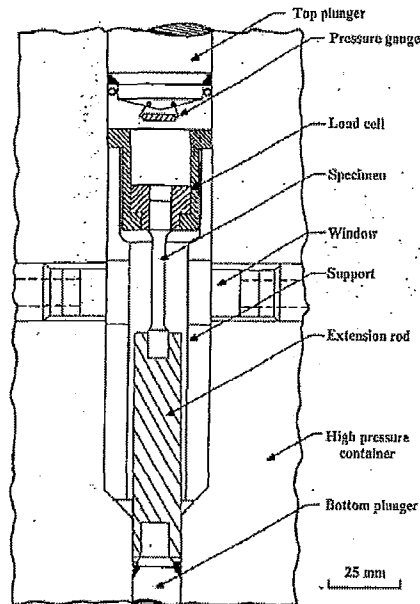


Figure 1.10: Schematic diagram of a typical fluid-based high pressure deformation apparatus. [Lewandowski and Lowhaphandu (1998)]

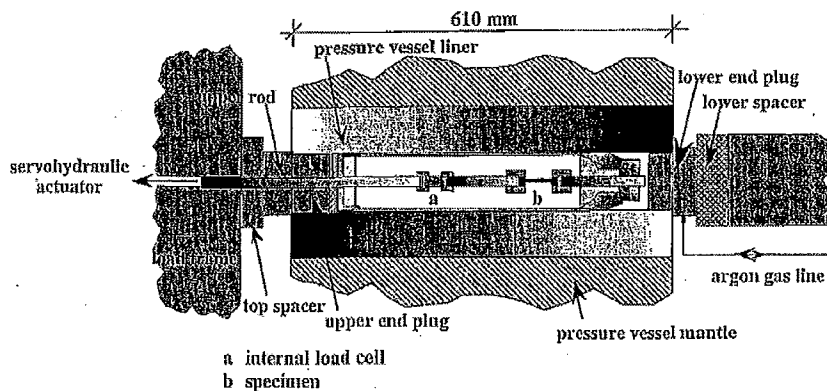


Figure 1.11: Schematic diagram of a typical gas-based high pressure deformation apparatus. [Lewandowski and Lowhaphandu (1998)]

Kao et al. (1990) studied tensile fracture and fractographic analysis of 1045 spheroidized steel under superimposed hydrostatic pressure. They found the transition

of the fracture surface of round tensile bars from a cup-cone fashion under atmospheric pressure to a slant structure under superimposed hydrostatic pressure (see Fig. 1.10), which is further explained on the basis of the void development leading to fracture and its corresponding change in fracture mechanism. It was pointed that void nucleation is suppressed and the rate of void generation with strain is decreased in round tensile bars under superimposed hydrostatic pressure. Moreover, subsize microvoids which assist the linkage of large voids by generating void-sheets are reduced in number as well.

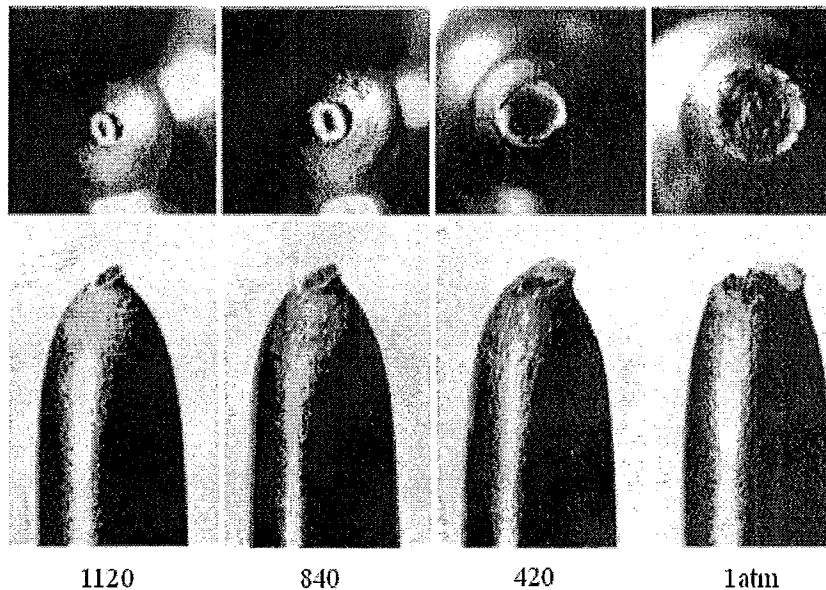


Figure 1.12: The appearance of the fractured tensile bars tested under applied pressure, Kao et al. (1990).

Gimple et al. (2001) examined the evolution of damage by performing uniaxial tensile tests on metal sheets under superimposed hydrostatic pressure. They found that the application of hydrostatic pressure decreased the amount of damage present in all samples tested and universally increased the observed ductility. When tested under sufficient pressure, some samples would change fracture modes and fail by ductile rupture with the damage processes suppressed or completely eliminated (see Fig. 1.11).

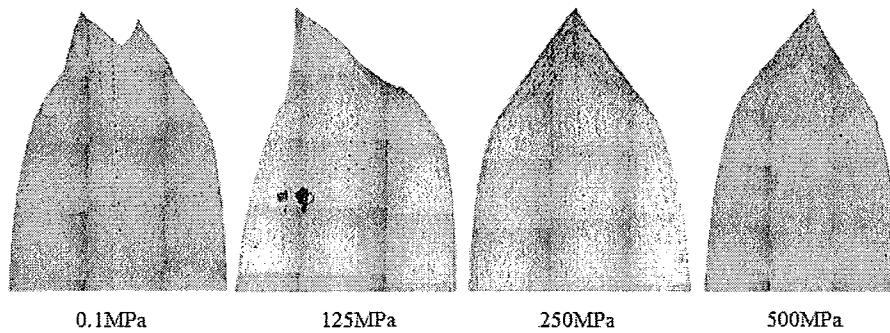


Figure 1.13: High-Fe5754 sample tested at various superimposed hydrostatic pressures. [Gimple et al. (2001)]

Korbel et al. performed experiments to show the influence of applied pressure on the formation of localized shear bands in an aluminum alloy. They concluded from experimental results that the onset of localization is insensitive to applied pressure but that the development of the bands is pressure sensitive, which indicates that dilational damage occurs during the growth of bands.

### 1.3.3 Numerical work

Numerous experimental works were conducted by researchers studying the effects of superimposed hydrostatic pressure on the mechanical behavior of monolithic materials, however very few numerical works have been reported on this topic. Recently, Wu et al. (2008) have studied the effect of superimposed hydrostatic pressure on sheet metal formability through both analytical and numerical methods. By employing classical isotropic plasticity theory, it is demonstrated that the superimposed hydrostatic pressure,  $p$ , lowers the true tensile stress level at yielding while the material work-hardening is independent of  $p$ . The forming limit diagram (FLD) based on the M-K approach is constructed to assess the superimposed hydrostatic pressure on sheet metal formability. It is reported that the superimposed hydrostatic pressure delays the initiation of necking for any strain path. Moreover, Peng et al. (2009) have numerically reproduced the experimentally observed transition of the fracture surface, from a cup-cone mode under atmospheric pressure to a slant fracture under high pressures by employing the Gurson-Tvergaard-Needleman (GTN) damage model. From their investigation, it is also reported that superimposed hydrostatic pressure has no effect on necking for a damage-free round bar under tension.

## **1.4 Thesis outline**

Based on the highly improved metal clad composites with a “clean” interface processed by “Novelis Fusion Technology”, finite element numerical models are developed to investigate the enhanced ductility of both clad round tensile bars and clad tensile sheets. Numerical investigation and finite element models are conducted in studying the superimposed hydrostatic pressure on monolithic tensile sheets. Effects of clad materials and superimposed hydrostatic pressure on improvement of ductility in monolithic material are presented.

Chapter 2 is mainly devoted to the description of the Gurson model. Chapter 3 presents numerical simulation and analysis of clad round bars under axisymmetric tensile loading. Chapter 4 describes work done on the investigation of numerically simulated clad tensile sheets under plane strain tension. Chapter 5 discusses the numerical model and finite element analysis of tensile sheets under superimposed hydrostatic pressure. Finally, Chapter 6 summarizes the major findings and conclusions in this research work.

## Chapter 2 Gurson damage model

Fracture is the local separation of the material into pieces. Usually, two types of fracture are defined: brittle fracture and ductile fracture. In brittle fracture, materials do not undergo apparent plastic deformation before failure whereas extensive plastic deformation is usually found in ductile fracture. The ductile failure of structures usually consists of three stages: damage accumulation, fracture initiation and crack propagation.

In ductile fracture, microscopically, material damage is associated with void nucleation, growth and coalescence, shear band movement and micro-crack propagation. Macroscopically, the deterioration of material is reflected by the decrease of material stiffness, strength, and ductility. Classical elasticity and plasticity theories are usually sufficient in dealing with many practical engineering problems. However in some industrial applications, for example, in sheet metal forming, materials usually undergo large deformation by rolling, extrusion, deep drawing processes etc., in which the microstructure of materials are often changed. The change in material microstructure is able to be more accurately described by introducing a damage model than by relying solely on classical elasticity and plasticity theory.

In the investigation of the mechanical behavior of engineering materials, two approaches are often used. The macroscopic approach represents the aggregate response of the material while the microscopic approach models the evolution of microscopic structures. In this chapter, several classical damage models based on either macroscopic or microscopic approaches will be briefly introduced. Particularly, the Gurson-like microscopic damage model will be analyzed in detail. Moreover, the existing Gurson damage model and its implementation in finite element software ABAQUS will be presented.

## 2.1 Damage models

In sheet metal forming, the plastic deformation is usually significant so that the damage effect on the material strength is profound. Therefore, the damage and the plasticity should be coupled and their combined effects have to be described in constitutive model to predict material ductile fracture.

### 2.1.1 Macroscopic damage models

Macroscopic models are constructed based on the macroscopic field variables such as stress/strain tensors and their increments, temperature or strain rate. Experiments show that the damaging process that eventually leads to fracture of material has strong dependence on the loading history, which has to be taken into account by using damage variables. Historically, many models consider the damaging process as being independent of the material plasticity behavior, which means that plasticity properties of the material do not change during damage accumulation in the material. A separate damage variable is used to represent fracture initiation in these models, among which the Johnson-Cook model is one of the widely used representative material constitutive models. Johnson and Cook present the failure function, which takes the form of a product of three factors, stress triaxiality (defined as mean stress divided by effective stress), strain rate, and temperature. The Johnson-Cook model is popularly used in simulation of strain rate sensitive problems, for instance, metal cutting problems, in which high strain rate and temperature effect are highly significant and cannot be ignored in the local area between cutting tool and workpiece. The Johnson-Cook model is empirical and its equivalent stress,  $\bar{\sigma}$ , is defined as Eq. 2.1:

$$\bar{\sigma} = \left[ \underset{\text{Item 1}}{A + B(\bar{\varepsilon}^{pl})^n} \right] \left[ \underset{\text{Item 2}}{1 + C \ln\left(\frac{\dot{\varepsilon}^{pl}}{\dot{\varepsilon}_0}\right)} \right] \left[ \underset{\text{Item 3}}{1 - \left(\frac{\theta - \theta_{transition}}{\theta_{melt} - \theta_{transition}}\right)^m} \right], \quad (2.1)$$

where  $\bar{\varepsilon}^{pl}$  is the equivalent plastic strain,  $\theta$  is the current temperature and  $\dot{\varepsilon}^{pl}$  is the equivalent plastic strain rate;  $\dot{\varepsilon}_0$  is the plastic strain rate,  $\theta_{melt}$  is the material melting

temperature,  $\theta_{transition}$  is the transition temperature at or below which there is no temperature dependence on the expression of the yield stress;  $A, B, C, n, m$  are material parameters measured at or below the transition temperature. Items 1-3 in Eq. 2.1 account for isotropic strain hardening, strain rate hardening and temperature softening, respectively.

The fracture criterion used in the Johnson-Cook model is a weighted integral with respect to the effective strain, see Eq. 2.2:

$$D = \int_0^{\epsilon^c} \frac{d\epsilon^{pl}}{\epsilon^{ef}(\sigma_m/\sigma_e, \dot{\epsilon}^{pl}, \theta)}, \quad (2.2)$$

where  $\sigma_m/\sigma_e$  is stress triaxiality defined as mean stress divided by effective stress,  $\epsilon^{ef}$  is the effective failure strain defined as Eq. 2.3:

$$\epsilon^{ef} = \left[ D_1 + D_2 \exp\left(D_3 \frac{\sigma_m}{\sigma_e}\right) \right] \left[ 1 + D_4 \log\left(\frac{\dot{\epsilon}^{pl}}{\dot{\epsilon}_0}\right) \right] \left[ 1 + D_5 \left(\frac{T - T_{transition}}{T_{melt} - T_{transition}}\right) \right], \quad (2.3)$$

where  $D_1 \sim D_5$  are material constants.

The advantage of the macroscopic damage models is that the damage evolution and the plasticity evolution are uncoupled. For example, in the Johnson-Cook model high strain rate and temperature effect are able to be taken into consideration when their influences are significant. The disadvantage is that the mechanical response of the material is over simplified by modeling a sudden drop of stress-strain response due to damage. Another main disadvantage for the application of this macroscopic damage model is that it requires a lot of experimental tests to calibrate the damage parameters.



### 2.1.2 Microscopic damage models

Compared with macroscopic or phenomenological damage models, microscopic or micromechanical damage models are constructed based on the complex microstructure of materials which contain multiphase materials, such as grains, second phase particles, precipitates and voids. The microscopic damage models treat materials as a cluster of inhomogeneous cells, which is different than macroscopic damage models that are based on homogeneous assumptions.

According to metallurgical observation, porous materials are defined when fracture of ductile solids is observed to start with nucleation, growth and coalescence of voids. A great deal of research work was focused on fracture prediction based on the microscopic mechanism of void nucleation, growth and coalescence. Due to the versatile combination of size, shape, orientation, and spacing of the voids, a lot of simplification and assumptions have been made to make the tracking of void evolution mathematically possible. The pioneering work was done by McClintock (1968) and Rice and Tracey (1969) who modeled an isolated cylindrical or spherical shape of void subjected to uniform remote stressing. The McClintock model analyzed a long cylindrical cavity in a non-hardening material pulled in the axial direction while subjected to transverse tensile stresses. The Rice-Tracey model considered the growth of a spherical void in non-hardening material and found that a spherical void subjected to a remote uniaxial tension strain rate field not only grows in radial direction, but also changes shape. More profoundly, research work was published by Gurson (1977) who introduced the influence of micro-voids to the plastic flow in a constitutive model. Tvergaard (1981) and Tvergaard and Needleman (1984) further extended the original Gurson model by including void growth acceleration.

## 2.2 Gurson damage model

The Gurson damage model and its modified form, the GTN model is a great success as a microscopic damage model in the prediction of fracture in many applications.

### 2.2.1 Original form of Gurson yield function

Before Gurson, there were no constitutive laws for engineering materials taking into consideration the effect on yielding of the hydrostatic component of stress, although a material's bulk dilatancy was already commonly observed. Gurson introduced a new yield function by analyzing an isolated cylindrical or spherical void in a continuum that is regarded as dilatational, pressure-sensitive and elasto-plastic. The introduction of Gurson model related plasticity and damage accounting for the nucleation and growth of micro voids. The approximate yield function for a porous ductile material was derived by Gurson in the form of Eq. 2.4 based on a rigid-perfectly plastic upper bound solution for spherically symmetric deformations around a single spherical void.

$$\phi(\boldsymbol{\sigma}, \bar{\sigma}, f) = \frac{\sigma_e^2}{\bar{\sigma}^2} + 2f \cosh\left(\frac{3\sigma_H}{2\bar{\sigma}}\right) - (1 + f^2) = 0 \quad (2.4)$$

Where  $\boldsymbol{\sigma}$  is the macroscopic Cauchy stress tensor;  $\bar{\sigma}$  is the matrix flow strength;  $f = \frac{V_{void}}{V_{total}}$  is the void volume fraction;  $\sigma_e = \sqrt{\frac{3}{2}\boldsymbol{\sigma}':\boldsymbol{\sigma}'}$  is the macroscopic von Mises stress;  $\boldsymbol{\sigma}'$  is the stress deviator;  $\bar{\sigma} = \bar{\sigma}(\bar{\epsilon}^{pl})$  is an equivalent tensile flow stress representing undamaged material;  $\bar{\epsilon}^{pl}$  is the equivalent plastic strain of material;  $\sigma_H = \mathbf{I}:\boldsymbol{\sigma}$  is the macroscopic mean stress. Interestingly, when  $f$  equals to zero  $\sigma_e/\bar{\sigma}$  will be constant (see Fig. 2.1) and the Gurson yield function results in the well-known von Mises yield function. Meanwhile,  $f = 1$  represents a fully void condition.

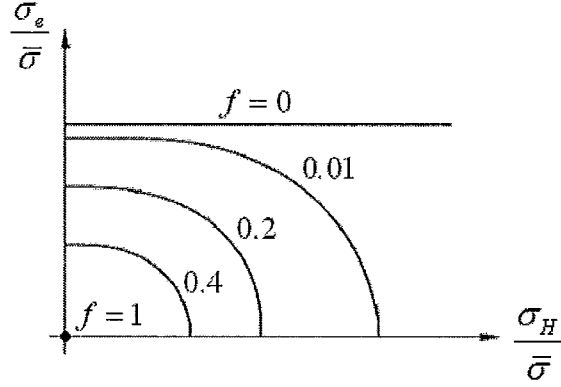


Figure 2.1: Yield surface dependence on the hydrostatic tension for various void volume fractions  $f$

According to  $J_2$  theory, the plastic flow function is the same as the yield function, therefore, the equivalent plastic strain is able to be derived through normality rule as shown in Eq. 2.5:

$$\mathbf{D}^p = \dot{E} \frac{\partial \phi}{\partial \boldsymbol{\sigma}}, \quad (2.5)$$

where  $\mathbf{D}^p$  and  $\boldsymbol{\sigma}$  are the equivalent strain rate and stress tensors respectively;  $\dot{E}$  is determined by the macroscopic equivalent plastic work rate and the microscopic plastic dissipations; Upper dot (') denotes time derivative. Therefore, the equivalent strain rate and the equivalent plastic strain rate are linked in the form of Eq. 2.6:

$$\boldsymbol{\sigma} : \mathbf{D}^p = (1-f) \bar{\sigma} \dot{\epsilon}^{pl}, \quad (2.6)$$

In the original Gurson yield function Eq. 2.4, the complete loss of load carrying capacity occurs when the modeled spheroid is fully void  $f=1$ . However, this is not true and is unrealistically larger than experimental observations. Tvergaard (1981) and Tvergaard and Needleman (1984) then introduced several parameters to describe the complete loss of load carrying capacity at a realistic level and taking void growth acceleration effect into consideration.

### 2.2.2 Gurson-Tvergaard-Needleman (GTN) damage model

In the original Gurson model, the expression of void evolution rate is able to be characterized by Eq. 2.7:

$$\dot{f} = (\dot{f})_{growth} + (\dot{f})_{nucleation}, \quad (2.7)$$

where  $(\dot{f})_{nucleation}$  represents the nucleation of new voids and  $(\dot{f})_{growth}$  describes the growth rate of existing voids. The experimental studies discussed by Brown and Embury (1973) and Goods and Brown (1979) show that the voids begin to coalesce when the void volume fraction reaches a certain value. The experimental work also indicates that coalescence of two neighboring voids occurs approximately when their length has grown to the order of magnitude of their spacing. Void coalescence largely accelerates the increase of void volume fraction. Tvergaard and Needleman (1984) introduced void coalescence into the original form of Gurson equation by adding an additional term  $(\dot{f})_{coalescence}$  as in Eq. 2.8, which limits the direct application of the Gurson model to a void volume fraction below a critical value  $f_c$ .

$$\dot{f} = (\dot{f})_{growth} + (\dot{f})_{nucleation} + (\dot{f})_{coalescence}, \quad (2.8)$$

Figure 2.2 shows the schematic diagram of the typical process of void nucleation and void evolution due to void growth and void coalescence.

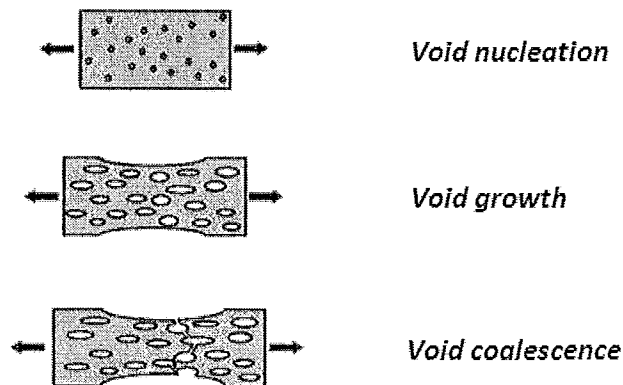


Figure 2.2: Schematic diagram of void nucleation, void growth and void coalescence

Numerically, Tvergaard (1981) introduced two material parameters  $q_1$  and  $q_2$  as calibration coefficients to improve the agreement with numerical studies of materials containing periodically distributed circular cylindrical or spherical voids. The modified GTN constitutive model is characterized in the form of Eq. 2.9:

$$\phi(\sigma, \bar{\sigma}, f) = \frac{\sigma_e^2}{\bar{\sigma}^2} + 2f^* q_1 \cosh\left(\frac{3q_2 \sigma_H}{2\bar{\sigma}}\right) - \left[1 + (q_2 f^*)^2\right] = 0, \quad (2.9)$$

where the function  $f^*(f)$  is to present the loss of stress carrying capacity accompanying void coalescence, which is in the form of Eq. 2.10:

$$f^* = \begin{cases} f, & \text{for } f \leq f_c \\ f_c + \frac{f_u^* - f_c}{f_f - f_c} (f - f_c), & \text{for } f > f_c \end{cases}, \quad (2.10)$$

where  $f_c$  is the critical void volume fraction at which void coalescence commences;  $f_f$  is the final void volume fraction at fracture;  $f_u^* = 1/q_1$  represents that material experiences a complete loss of strength when  $f$  reaches final void volume fraction.

In Eq. 2.8,  $(\dot{f})_{growth}$  can be expressed as a function of the plastic strain rate tensor  $\mathbf{D}^p$  as shown in Eq. 2.11:

$$(\dot{f})_{growth} = (1 - f) \mathbf{I} : \mathbf{D}^p, \quad (2.11)$$

And  $(\dot{f})_{nucleation}$  can be presented in the following form:

$$(\dot{f})_{nucleation} = a \dot{\bar{\epsilon}}^{pl} + A \dot{\bar{\sigma}} + \frac{1}{3} B \mathbf{I} : \overset{\nabla}{\bar{\sigma}}, \quad (2.12)$$

where  $\overset{\nabla}{\bar{\sigma}} = \mathbf{L} : (\mathbf{D} - \mathbf{D}^p)$  is the Jaumann rate;  $\mathbf{L}$  is the elastic moduli tensor;  $\mathbf{D}$  is the equivalent strain tensor.

Furthermore, Chu and Needleman (1980) considered strain-controlled void nucleation in a statistical way and proposed an expression of  $(\dot{f})_{coalescence}$  as shown in Eqs. 2.13 and 2.14 describing that the nucleation follows a normal distribution with respect to the plastic strain of the matrix material.

$$(\dot{f})_{nucleation} = \bar{A} \dot{\bar{\epsilon}}^{pl}, \quad (2.13)$$

$$\bar{A} = \frac{f_N}{s_N \sqrt{2\pi}} \exp \left[ -\frac{1}{2} \left( \frac{\bar{\epsilon}^{pl} - \epsilon_N}{s_N} \right)^2 \right], \quad (2.14)$$

where  $\epsilon_N$  is the mean value of the distribution of the plastic strain;  $f_N$  is the volume fraction of void nucleating particles;  $s_N$  is the standard deviation of void nucleating strain.

Even though the Gurson model is one of the most popular damage models in predicting material fracture, it has several drawbacks: 1) The governing parameters of void size, shape, orientation and spacing should be determined stochastically but the distributions of these parameters are often unknown; 2) The Gurson model fails to consider viscoplastic materials which display significant rate-dependence; 3) The Gurson model fails to consider the void shearing mechanism which has been observed as one of the important fracture mechanisms in some circumstances. A great deal of research work was focused on improving the modified Gurson damage model and will be presented in the next section.

### 2.3 Recent development of the Gurson model

Gologanu et al. (1998) extended Gurson's equation by incorporating void shape effects into the model. The modification by Wen et al. (2004) accounted for the void size effect. Chen et al. (2004) established a constitutive model for viscoplastic materials containing microvoids following Gurson's approach. Currently, extensive interests [Nahshon and Hutchinson (2008), Nahshon and Xue (2009), Xue (2007, 2008)] have been focused on modifying the Gurson model to include the shearing fracture mechanism.

### 2.3.1 A dilatational plasticity theory for viscoplastic materials

Gurson developed a rate-independent dilatational plasticity theory for voided, dilating materials to incorporate the effect of hydrostatic stress. However, some metallic materials may display significant rate-dependence, viscoplastic behavior, particularly at high temperatures. Following Gurson's approach, Chen et al. (2004) proposed their constitutive model by homogenizing the microvoids in a viscoplastic matrix in order to determine the macroscopic stress in terms of the macroscopic strain-rate and void volume fraction. In their research work, they generalize the Gurson dilatational plasticity theory for voided, dilating viscoplastic materials based on the same unit cell model. Their constitutive model is able to be degenerated to the Gurson model when the rate-sensitivity disappears. The approximate analytical constitutive relations have been proposed for voided, dilating viscoplastic materials and have the correct asymptotic limits which agree well with the unit-cell model. They also proposed that the void growth rate in viscoplasticity depends on the mean stress via a power law  $(\Sigma_m)^m$  where  $m$  is the rate sensitivity exponent.

### 2.3.2 Modification of Gurson model for shearing effect in ductile fracture

During the process of void coalescence, the voids have grown to a certain extent so that they begin to interact with another. In general, void linkage can occur at any orientation. Particularly, voids ligament are often broken either perpendicular to the loading directions or in the localized shear direction. The first case results in "intervoid ligament necking" while the second case is "void shearing". Most recent experimental work clearly showing both of the two mechanisms of void linkage in pure copper samples (see Fig. 2.3) was presented by Weck et al. (2006). Both samples are voided with a square array of holes with respect to the tensile axis before testing. Fig. 2.3(a) shows the result of an initially  $15^\circ$  orientation void array, which fails by intervoid ligament necking while Fig. 2.3(b) shows the result of an initially  $45^\circ$  orientation void array, which fails by void shearing.

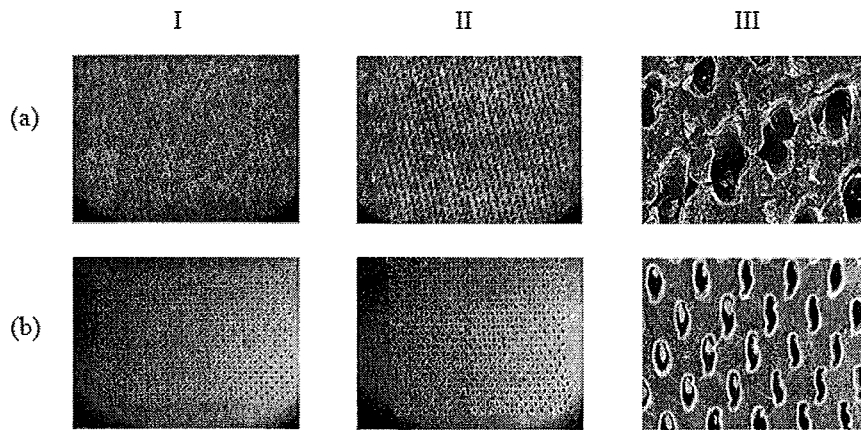


Figure 2.3: Deformation sequence for a copper sample with a rectangular array of holes oriented at (a)  $15^\circ$  (b)  $45^\circ$  with respect to the tensile axis. I(a) and I(b): Underformed sample; II(a) and II(b): Sample right at the coalescence event; III(a): Coalescence occurring by internal necking between the voids; III(b): Strong shearing between the voids and its effect on the shape of the holes. [Weck et al. (2006)]

Other experiments show that many metallic materials are susceptible to shear fracture under low triaxiality. Bao and Wierzbicki (2004) presented data and emphasized that the relation between the effective plastic strain at fracture and mean stress is not generally monotonic. Barsoum and Faleskog (2007a) tested circumferentially notched tubes in combined tension and torsion with the specific purpose of delineating the roles of stress triaxiality and Lode parameter. They also reported susceptibility to fracture under low triaxiality shearing. Due to the fact that the Gurson model fails to include the possibility of shear localization and fracture under the low triaxiality condition, several theoretical studies and extension of the Gurson model have been proposed to incorporate damage growth under triaxiality straining for shear-dominated states [McClintock et al. (1966), Barsoum and Faleskog (2007b), Gao and Kim (2006), Nahshon and Hutchinson (2008), Nahshon and Xue (2009) and Xue (2007, 2008)].



Nahshon and Hutchinson (2008) modified the Gurson model by introducing a new parameter  $k_w$  to set the rate of damage development in shear. Their modified model is capable of modeling localization and fracture in shear-dominated stress states with low triaxiality due to void rotation and distortion. Nahshon and Xue (2009) further extended the model and developed the corresponding numerical implementation method by creating a VUMAT user material in the finite element software ABAQUS/Explicit. Several benchmark tests were developed as well to verify the code. From their research work, the new parameter  $k_w$  is calibrated by comparing numerical and experimental results for quasi-static punch-out experiments.  $k_w = 2$  was proposed as the value of the new parameter for DH35 steel according to their study.

Meanwhile, Xue (2007, 2008) extended the Gurson model by including the dependence of ductile fracture on the third stress invariant. He proposed two methods for void shearing damage: “the damage counter” and “the damage associated yielding model”. The first proposal describes yielding based on the void volume fraction and predicts the onset of fracture using a separate damage indicator. The second proposal considers yielding directly from the damage indicator. Both models are able to predict the fracture in simple shear.

## 2.4 Gurson model in finite element software ABAQUS

The Gurson model is in the category of porous metal plasticity in the current version of finite element software ABAQUS. The existing Gurson model [ABAQUS/Explicit User's Manual (2005)] is strain-controlled taking void nucleation, void growth and void coalescence into consideration, however, excluding the void shearing effect. The Gurson model is available in both implicit and explicit versions of ABAQUS; However ABAQUS/Implicit doesn't include void coalescence  $f_c$  and  $f_f$  which is otherwise available in ABAQUS/Explicit. Material parameters  $\varepsilon_N$ ,  $s_N$ ,  $f_0$ ,  $f_c$ ,  $f_f$ ,  $q_1$ ,  $q_2$ , and  $q_3 = q_1^2$  are required in implementing damage simulation via the Gurson model in ABAQUS/Explicit. A comparison of the Gurson damage model defined in ABAQUS/Implicit and ABAQUS/Explicit has been investigated by using a unit cell model. The normalized force and true strain curves of both methods match very well before the peak of normalized force. The load drops more sharply in the ABAQUS/Implicit Gurson model than that in the ABAQUS/Explicit Gurson model. This is because ABAQUS/Explicit introduces void coalescence  $f_c$  and  $f_f$  that much better matches experimental observation. In the numerical simulation, elements will be deleted when the void volume fraction at final fracture  $f_f$  meets the assumed value. More specifically, a job using ABAQUS/Implicit will be terminated when the nucleation strain  $\varepsilon_N$  reaches the input value while a job using ABAQUS/Explicit will continue until the specimen is fully fractured. In the current research work, considering the fact that void coalescence has to be included, ABAQUS/Explicit was selected to develop the finite element analysis. However, to ensure that the problems investigated are under a quasi-static condition, a small velocity was defined.

## Chapter 3 Enhanced ductility in clad round tensile bars

### 3.1 Introduction

Composite clad rods or round bars consisted of two or more different materials have their applications in diverse fields such as in electronic, nuclear and chemical industry. Commercial applications are, for example, super-conductor cables with NbTi or NbSn as cores and pure copper as outer cladding and fuel rod with Zircaloy-4 cladding. Composite clad rods/round bars are usually made by extrusion, by which technically the cross-section profile can be round or any arbitrary shape [Wu and Hsu (1999)]. Microstructural study of laminated round bar was presented by Jimenez et al. (1991). However, very few papers discussed the mechanical behavior of composite clad round bars. Most research work of investigation of enhanced formability or ductility focused on the laminated sheet structures [Kim et al. (2003), Li and Suo (2006), Wagstaff et al. (2006), Xue and Hutchinson (2007)]. Considering that the demands for composite clad rods or round bars have accelerated in many applications, it is worthwhile to study the mechanical behavior of laminated round bar structures.

In this chapter, we are going to carry out a detailed numerical study of the influence of a clad ductile ring/tube on fracture in round bar structure under tension (see Fig. 3.1). All simulations are performed using finite element software package ABAQUS/Explicit.

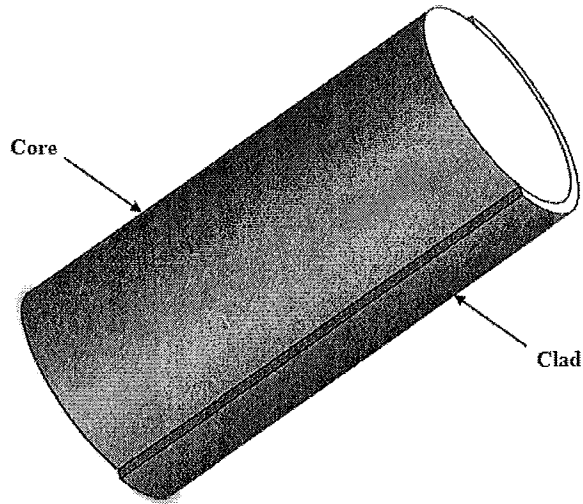


Figure 3.1: 3D view of a bilayer clad round bar

### 3.2 Problem formulation and method of solution

All simulations in this chapter are based on Gurson-Tvergaard-Needleman (GTN) damage model, which has been introduced in Chapter 2. The uniaxial true stress  $\sigma$  and true strain  $\varepsilon$  curve for the matrix material conforms to power-law as shown in Eq. 3.1:

$$\varepsilon = \begin{cases} \frac{\sigma}{E}, & \text{for } \sigma \leq \sigma_y \\ \frac{\sigma_y}{E} \left( \frac{\sigma}{\sigma_y} \right)^n, & \text{for } \sigma > \sigma_y \end{cases}, \quad (3.1)$$

where  $\sigma_y$  is the yield stress, and  $n$  is the strain hardening exponent.

We consider a round tensile bar, with initial length  $2L_0$  and initial radius  $R_0$ , as shown in Fig. 3.2a. We assume that the bar consists of a core cylinder, with radius  $\bar{R}_0$ , and a co-axial cladding tube, with outer radius  $R_0$  and inner radius  $\bar{R}_0$ . The thickness fraction of cladding  $\Gamma$  is thus defined as Eq. 3.2:

$$\Gamma = \frac{R_0 - \bar{R}_0}{R_0}, \quad (3.2)$$

The corresponding cladding volume fraction  $\Lambda$  can be presented as Eq. 3.3:

$$\Lambda = 2\Gamma - \Gamma^2, \quad (3.3)$$

Due to the symmetry, only half of the tensile bar is investigated. More specifically,  $Z = 0$  is a symmetric plane, and  $Z = L_0$  is a shear-free end. A tensile displacement  $U$  (or velocity  $\dot{U}$ ) is applied at  $Z = L_0$  (see Fig. 3.2b). The average tensile strain is defined as  $\varepsilon = \ln(1 + U/L_0)$ . To trigger necking at the middle-plane  $Z = 0$ , a small initial thickness inhomogeneity  $\Delta R$  is assumed in the form of

$$\Delta R = -\xi R_0 \cos\left(\frac{\pi Z}{L_0}\right), \quad (3.4)$$

The minimum cross-sectional areas of the entire bar and the core only at the middle-plane are calculated by Eqs. 3.5 and 3.6:

$$A_{\min} = \pi R_{\min}^2, \quad (3.5)$$

$$A_{\min}^{\text{core}} = \pi \bar{R}_{\min}^2, \quad (3.6)$$

The overall response of the bar under uniaxial tension is presented in terms of the normalized force  $F^*$  and normalized minimum cross-sectional area  $A^*$ :

$$F^* = \frac{F}{\sigma_y^{\text{core}} \pi \bar{R}_0^2 + \sigma_y^{\text{clad}} \pi (R_0^2 - \bar{R}_0^2)}, \quad (3.7)$$

$$A^* = \frac{A_{\min}}{A_0} = \left(\frac{R_{\min}}{R_0}\right)^2, \quad (3.8)$$

where  $F$  is the applied force, and  $\sigma_y^{\text{core}}$  and  $\sigma_y^{\text{clad}}$  are the yield stresses of core and clad materials, respectively. The ductility of the bar is measured in terms of the fracture strain:

$$\varepsilon_f = \ln\left(\frac{A_0}{A_f}\right), \quad (3.9)$$

where  $A_0$  is the original cross-sectional area and  $A_f$  the final cross-sectional area at the neck. The gain in ductility  $\varepsilon_f^*$  due to cladding is defined as a function of the thickness fraction of cladding  $\Gamma$ :

$$\varepsilon_f^*(\Gamma) = \frac{\varepsilon_f(\Gamma) - \varepsilon_f(0)}{\varepsilon_f(0)}, \quad (3.10)$$

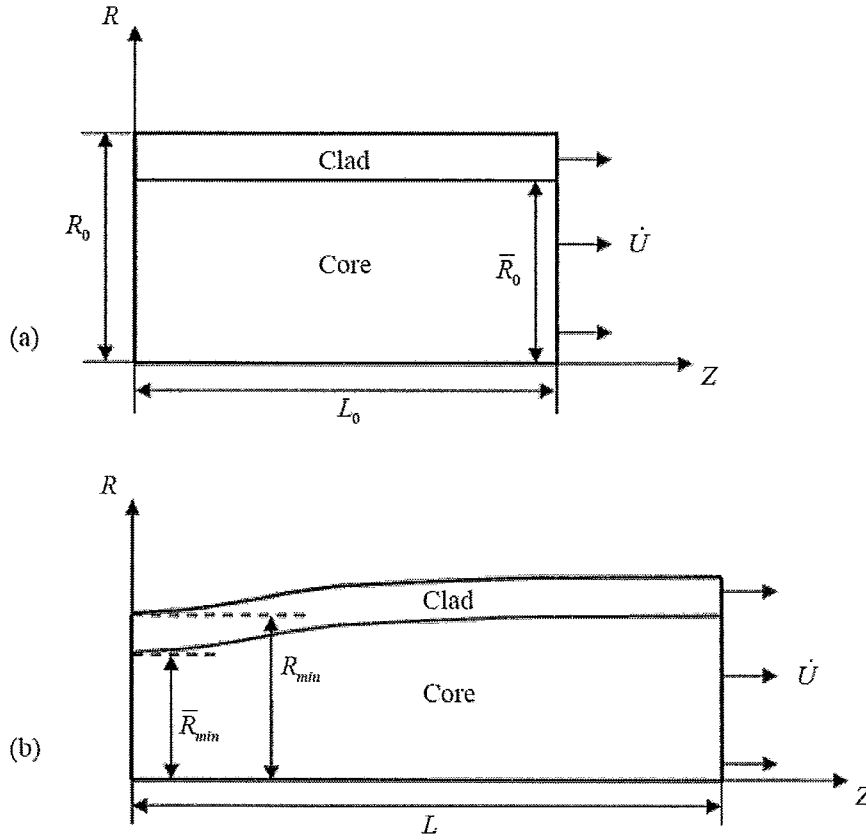


Figure 3.2: Schematic representation of a round tensile bar with a ductile cladding ring. (a) Undeformed state, and (b) deformed state.

### 3.3 Results and discussions

The elastic-plastic properties of the matrix material of the core cylinder are specified by  $\sigma_y = 1$ ,  $\sigma_y/E = 0.0033$ ,  $\nu = 0.3$  and  $n = 10$ . We assume that there are no initial voids, and the parameters  $q_1 = 1.0$  and  $q_2 = 1.5$  are used in the yield function Eq. 2.9. The void nucleation is assumed to be plastic strain controlled, with the volume fraction  $f_N = 0.04$  of void nucleating particles, the mean strain for nucleation  $\varepsilon_N = 0.3$ , and the corresponding standard deviation  $s_N = 0.1$ . The final failure is taken to be characterized by the parameters  $f_c = 0.15$  and  $f_f = 0.25$ . The values of the material parameters for the cladding tube are the same as those for the core cylinder except:  $\sigma_y = 0.6$ ,  $n = 5$  and  $\varepsilon_N = 0.5$ . Fig. 3.3 shows true stress and

true strain curves for the core and clad materials under homogeneous uniaxial tension. It is clear that, compared to the core material, the clad material has relatively lower yielding stress but higher hardening. We further assume that the ratio of initial length to radius is given by  $L_0/R_0 = 2$ , and the value of the initial imperfection in Eq. 3.2 is assumed to be  $\xi = 0.001$ . The applied velocity  $\dot{U} = 0.0001/s$ .

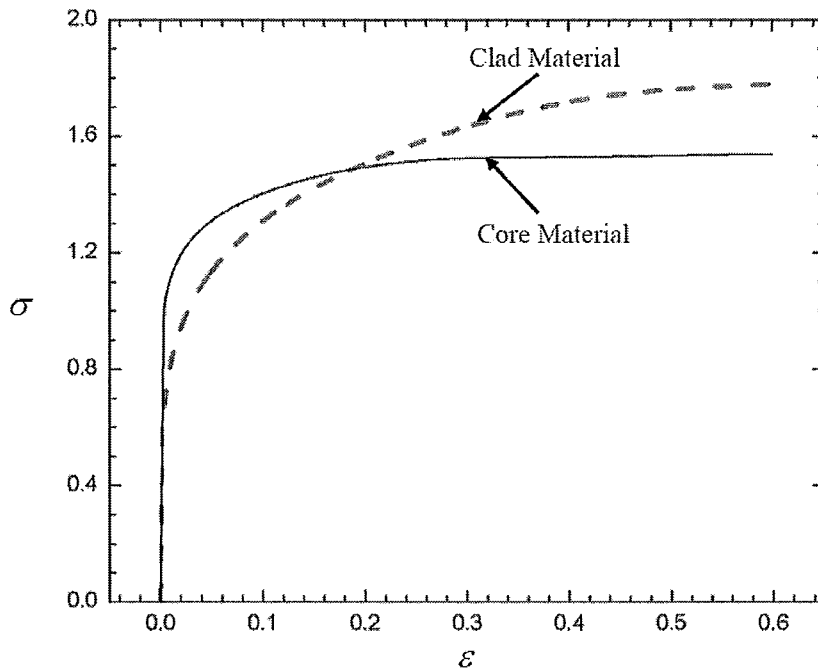


Figure 3.3: Uniaxial stress and strain curves of the core and clad materials.

It has been generally accepted that there is significant mesh sensitivity in a numerical simulation involving deformation localization and failure. In the present study, the cup-cone fracture mode, experimentally observed in monolithic ductile round tensile bars, is expected. As already mentioned by Tvergaard and Needleman (1984), the initial mesh design required for an analysis of final failure in a round tensile bar is essentially controlled by the first occurrence of fracture in the centre of the neck. Tvergaard and Needleman (1984) have carefully studied the mesh sensitivity in their analysis of the cup-cone fracture in a round tensile bar with mechanical properties being the same as the core material in the present study.

Figure 3.4 shows a mesh, Mesh A, with local refinement around the middle-plane, and with total of  $28 \times 42$  quadrilateral elements (28 in the radius direction and 42 in the axial direction), each built up with four linear triangular elements (CAX3 in ABAQUS/Explicit). The element aspect ratio, the element size in the radius direction to the element size in the axial direction, of Mesh A in the local refined area near the middle-plane is 2. Mesh A is very similar to the one used in Tvergaard and Needleman (1984) and Peng et al. (2009). The number of elements in Mesh B, 56 in the radius direction and 84 in the axial direction, is four times of that in Mesh A. Since deformation localization and fracture depend sensitively on not only the number of elements but also the element aspect ratio (see e.g. Besson et al., 2001), Mesh C, with the same number of elements as in Mesh B but with the element aspect ratio being 3, is designed. A much finer mesh, Mesh D, consisting of  $112 \times 168$  quadrilateral elements (112 in the radius direction and 168 in the axial direction) with local refinement near the middle-plane and with the element aspect ratio being 2 in the refined area, is also used in the present work but mainly for the mesh sensitivity study.

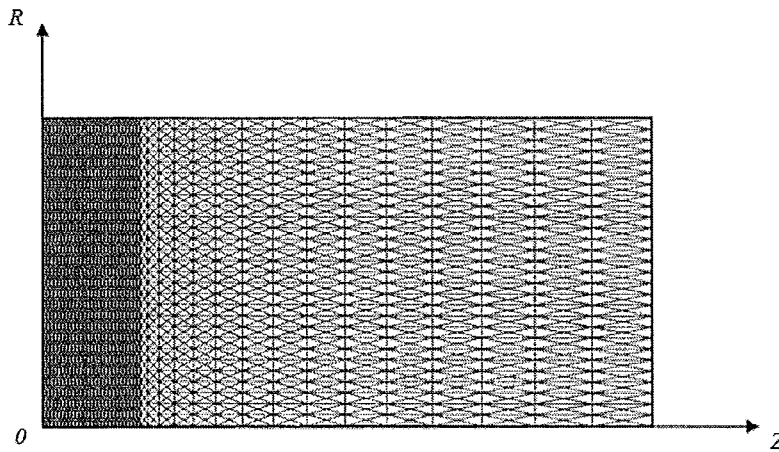


Figure 3.4: Mesh A with  $28 \times 42$  quadrilateral elements (28 in the radius direction and 42 in the axial direction), each built up with four linear triangular elements (CAX3 in ABAQUS/Explicit).

We first consider an extreme case: a round tensile bar without cladding ( $\Gamma = 0\%$  or  $\bar{R}_0 = R_0$ ). Figs. 3.5 and 3.6 present the normalized tensile force  $F^*$  and minimum cross-sectional area  $A^*$  as functions of the tensile true strain



$\varepsilon = \ln(1 + U/L_0)$ , for the round tensile bar with core cylinder only ( $\Gamma = 0\%$ ). For a comparison, the results based on the corresponding homogeneous deformation are also included. It is important to bear in mind that the main purpose of the present study is to assess the effects of cladding on fracture in a round tensile bar. Since the geometry and the values of the material parameters for the core material are exactly the same as used in Tvergaard and Needleman (1984) and Peng et al. (2009), we only briefly explain how the cup-cone fracture surface is formed in a round tensile bar without cladding. For details, we refer to Tvergaard and Needleman (1984) and Peng et al. (2009). It is found that the force increases linearly with the imposed straining when the deformation is very small and the material is essentially in the elastic state. With continued straining, the force gradually reaches its maximum at around  $\varepsilon = 0.1$  and then gradually decreases due to both the reduction of the cross-sectional area and the softening effect resulting from void nucleation and growth. Further straining results in a sharp “knee” on the force and axial strain curve, which is associated with reaching the critical value of the void volume fraction ( $f_c = 0.15$ ) in the centre of the neck. Immediately after the sharp knee, the burst of void nucleation and growth leads to a rapid drop in true stress which in turn results in a rapid loss of load carrying capacity for the tensile bar. The open triangles indicate the initiation of fracture. From Fig. 3.5, it is clear that necking and failure in the finer meshes (Mesh B, Mesh C and Mesh D) occur earlier than those based on the crude mesh (Mesh A). However, all the meshes predict quite similar necking and fracture processes. The development of necking and failure processes can be more evidently presented in terms of the minimum cross-section area  $A_{\min}$  and true strain  $\varepsilon$  curves (see Fig. 3.6). For the axisymmetric problem considered here,  $A_{\min} = \pi R_{\min}^2$  with  $R_{\min}$  being the minimum radius in the necked region (see Fig. 3.2b). Necking occurs where the curve deviates from that corresponding to the homogeneous tension. It is interesting to note that when fracture occurs, neck development essentially stops ( $R_{\min}$  is almost a constant). As already pointed out by Tvergaard and Needleman (1984), this implies that the reduction in area at fracture is a representative measure of the onset of macroscopic fracture in the tensile test. Fig. 3.6 also indicates that all the meshes predict quite

similar necking and failure process while finer meshes determine earlier necking and failure.

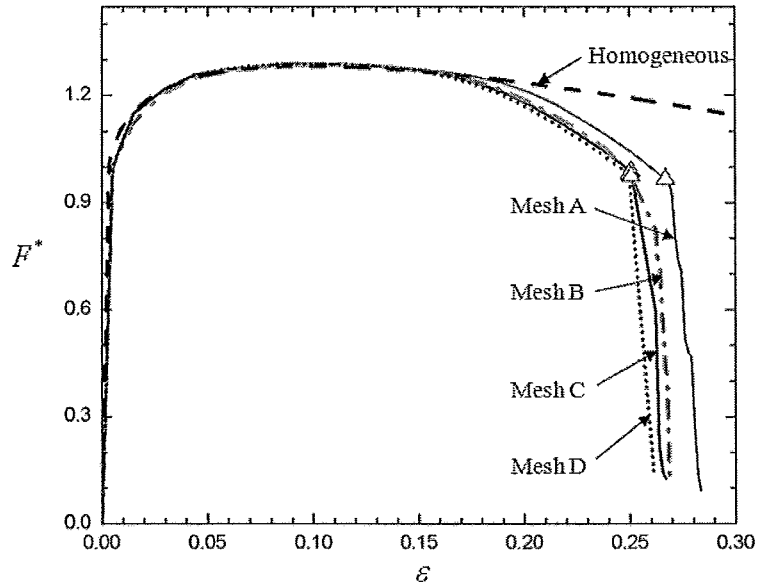


Figure 3.5: Predicted normalized force  $F^*$  and tensile strain  $\varepsilon = \ln(1 + U/L_0)$  curve for a round bar of the core material ( $\Gamma = 0$ ).

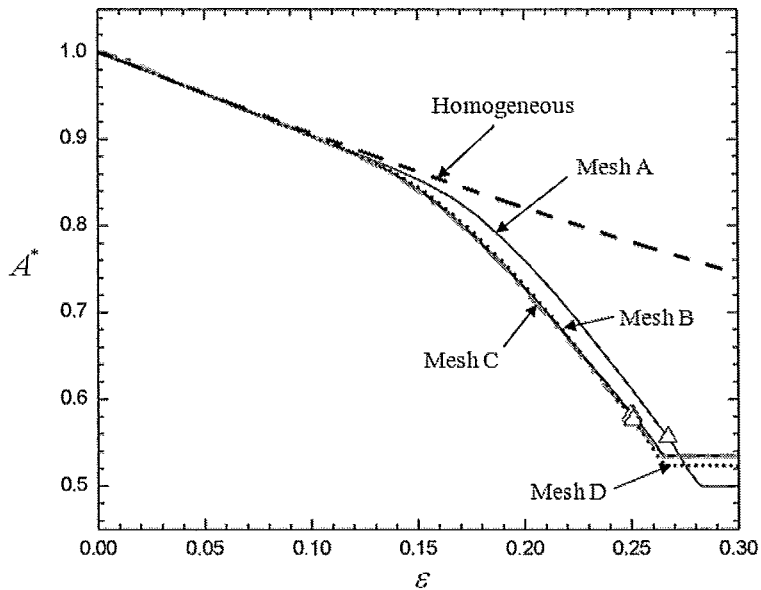


Figure 3.6: Predicted normalized minimum cross-sectional area at the middle-plane  $A^*$  and tensile strain  $\varepsilon = \ln(1 + U/L_0)$  curve for the round bar of the core material ( $\Gamma = 0$ ).

Deformed meshes at various deformation stages in the uniaxial tension of the round bar without cladding are shown in Fig. 3.7. Since Mesh B and Mesh C will be used in the rest of the present study, our explanations will mainly be based on these two meshes. Using Mesh B, it is found that, at the axial strain around 0.261, fracture initiates at the centre of the neck, where the maximum stress triaxiality is expected to occur. Due to the significant constraint resulting from the axisymmetry, the crack initially propagates almost vertically along the middle plane. This constraint becomes less and less with the distance from the centre of the neck. At an axial strain of 0.267, the crack has progressed half way through the bar and tends to move away from the middle-plane and along the shear bands (though relatively weak and not clearly exhibited in Fig. 3.7). With further straining, the inclined crack has stopped and begins to zig-zag. The amplitude of the zig-zag increases as the crack approaches the free surface, where the axisymmetry constraint has been reduced significantly. This crack perturbation produces the cone of the cup-cone fracture surface. It is clear that both meshes are able to show the cup-cone fracture mechanism. The main difference between Mesh C and Mesh B is that Mesh C does not show the zig-zag before the cone of the cup-cone has been formed. Although not shown here, it is found that the much finer mesh, Mesh D, detects fracture earlier and produces a relatively larger cone. Carefully examining the deformed meshes confirms that the initial zig-zag of the crack near the neck centre depicted in Fig. 13 of Tvergaard and Needleman (1984) was an artefact of the mesh they used. As mentioned by Tvergaard and Needleman (1984), it should be noted that the present study assumes symmetry about the middle-plane and thus two symmetrical conical fracture surfaces are predicted. However, in reality one of these cracks will finally dominate, which results in the cup-cone fracture observed experimentally (see also Besson et al. 2001). It is very important to be noted that the element aspect ratio of Mesh B is about one at the moment of the onset of cracking.

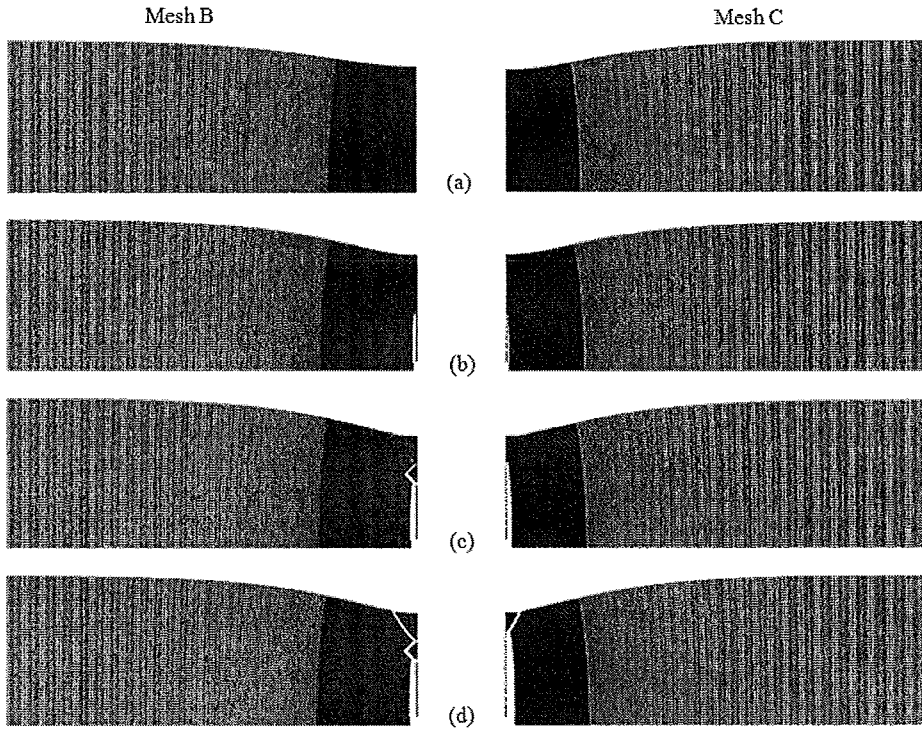


Figure 3.7: Deformed meshes at various deformation stages for the round bar of the core material ( $\Gamma = 0$ ). (a)  $\varepsilon = 0.227$ , (b)  $\varepsilon = 0.262$ , (c)  $\varepsilon = 0.268$ , and (d)  $\varepsilon = 0.271$ .

The mesh sensitivity is further studied by considering another extreme: a round tensile bar without core ( $\Gamma = 100\%$  or  $\bar{R}_0 = 0$ ). As mentioned previously, comparing to the core material, the clad material has relatively lower yield stress but higher hardening (see Fig. 3.3). It is expected that the process of necking and cracking in the tensile bar of the clad material will be noticeably delayed compared to that in the tensile bar made of the core material. Figs. 3.8 and 3.9 show the normalized tensile force  $F^*$  and normalized minimum cross-sectional area  $A^*$  as functions of the tensile true strain  $\varepsilon = \ln(1 + U/L_0)$ , for the round tensile bar made entirely of the clad material ( $\Gamma = 100\%$ ). It is observed that Mesh B and Mesh C predict very close overall tensile response in terms of the applied force and minimum cross-sectional area. However, the predicted fracture surfaces are quite different (see Fig. 3.10). More specifically, Mesh C shows a typical cup-cone fracture mode while Mesh B exhibits a very smooth fracture surface. It is noted that the element aspect ratio of Mesh C is

about one at the moment of the onset of cracking. The results based on Mesh D, though not shown here, are very similar to those based on Mesh B. The main difference between Mesh D and Mesh B is that Mesh D detects an earlier fracture.

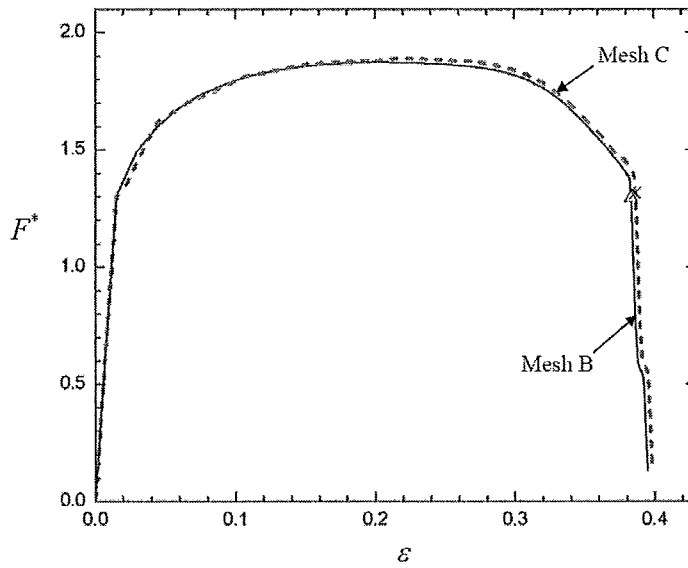


Figure 3.8: Predicted normalized force  $F^*$  and tensile strain  $\varepsilon = \ln(1 + U/L_0)$  curve for a round bar of the clad material ( $\Gamma = 100\%$ ).

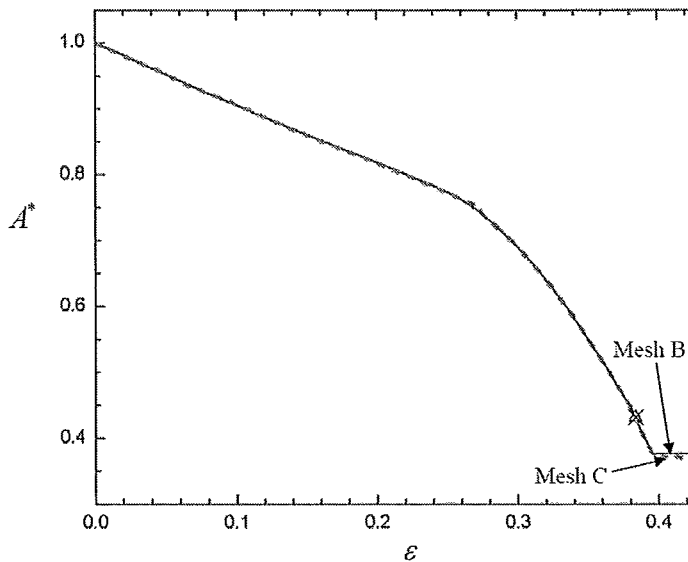


Figure 3.9: Predicted normalized minimum cross-sectional area  $A^*$  at the middle-plane and tensile strain  $\varepsilon = \ln(1 + U/L_0)$  curve for the round bar of the clad material ( $\Gamma = 100\%$ ).

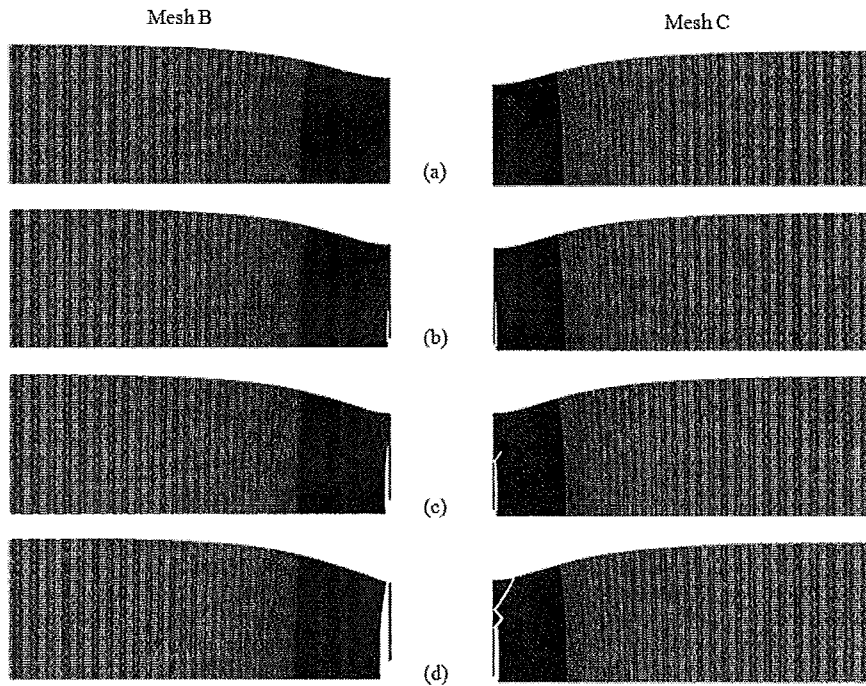


Figure 3.10: Deformed meshes at various deformation stages for the round bar of the clad material ( $\Gamma = 100\%$ ). (a)  $\varepsilon = 0.405$ , (b)  $\varepsilon = 0.407$ , (c)  $\varepsilon = 0.408$ , and (d)  $\varepsilon = 0.410$ .

Based on the above observations and the results reported in Peng et al. (2009), it becomes clear that while the overall/averaged response is predicted with confidence, the calculated subtle appearance of fracture surface could be very sensitive to the mesh used and may even be an artefact of the mesh. All the simulations reported in the rest of the present study will be based on both Mesh B and Mesh C. The effort is made by two piece of motivation. On one hand, Mesh B and Mesh C are respectively the best mesh, in the range considered, to predict the cup-cone fracture mode for the two extremes, and the responses of round tensile bars with cladding are expected to be in between the two extremes. On the other hand, the main purpose of the present study is to assess the effects of cladding on the initiation of cracking (the symbols shown in Figs. 3.5, 3.6, 3.8, 3.9) and the completion of fracture (the horizontal lines in Figs. 3.6 and 3.9), which are not very sensitive to the mesh used. Numerical results will be mainly reported according to Mesh B unless mentioned otherwise.

We proceed by studying the effects of cladding on fracture in the round tensile bars. Figs. 3.11 and 3.12 show the normalized force  $F^*$  and the normalized minimum cross-sectional area  $A^*$  versus the axial strain  $\varepsilon$  curves, respectively. The forces are calculated by summation of the reaction forces at  $Z = L_0$ . It is observed that cladding a ductile ring increases the flow stress and the strain at which the applied force reaches its maximum. This implies that cladding increases the strain when necking occurs. It is also found from Figs. 3.11 and 3.12 that cladding delays cracking (open triangles indicate the initiation of cracking). Furthermore, from Fig. 3.12, the maximum reduction in area, indicated by the horizontal  $A^*$  lines, increases with increasing cladding. This means that the ductility is enhanced by cladding.

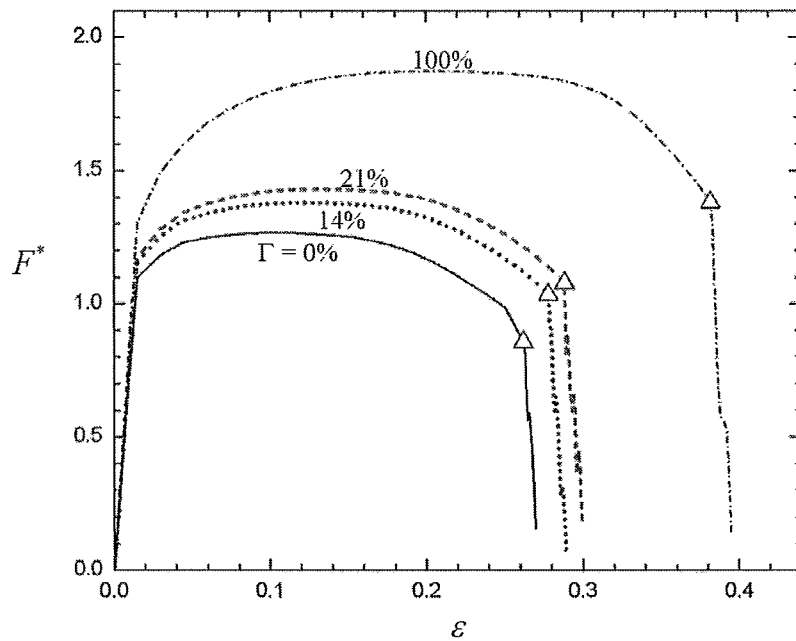


Figure 3.11: Predicted normalized force  $F^*$  and tensile strain  $\varepsilon = \ln(1 + U/L_0)$  curves for round tensile bars with various cladding thickness ratio  $\Gamma$ .

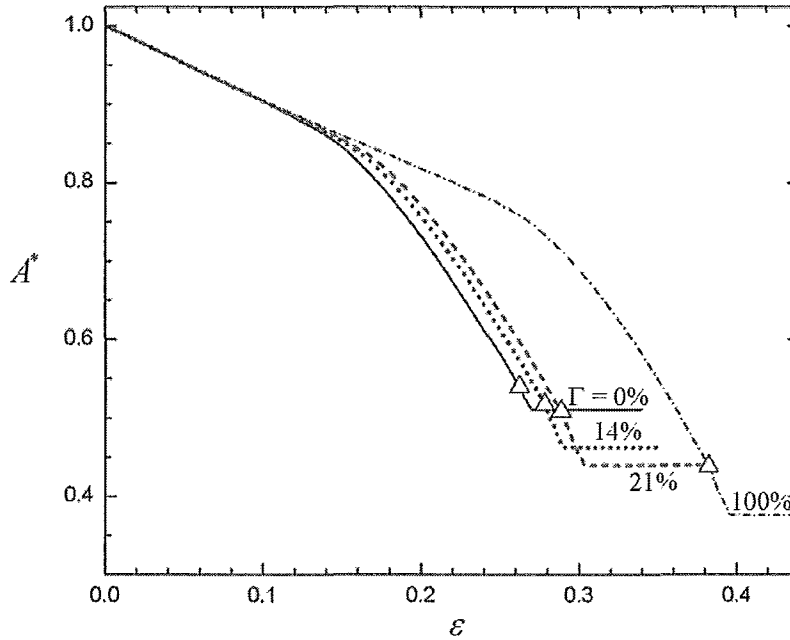


Figure 3.12: Predicted normalized minimum cross-sectional area  $A^*$  at middle-plane and tensile strain  $\varepsilon = \ln(1 + \Delta L/L_0)$  curves for round tensile bars with various cladding thickness ratio  $\Gamma$ .

The predicted effect of cladding on necking is more clearly shown in Fig. 3.13. Numerical results indicate that the predicted necking strain is not sensitive to the meshes used. Fig. 3.13 also includes the necking strains based on the Considère-type criterion:

$$\frac{d\bar{\sigma}_a}{d\varepsilon} = \bar{\sigma}_a, \quad (3.11)$$

Here, the averaged flow stress  $\bar{\sigma}_a$  for the round tensile bar is calculated from the rule of mixtures [Semiatin and Piehler (1979a)]:

$$\bar{\sigma}_a = (1 - \Lambda)\bar{\sigma}_{\text{core}} + \Lambda\bar{\sigma}_{\text{clad}}, \quad (3.12)$$

where  $\bar{\sigma}_{\text{core}}$  and  $\bar{\sigma}_{\text{clad}}$  are the flow stresses for the core cylinder and cladding tube, respectively. The excellent agreement between the theoretical prediction and the numerical simulations indicates that the overall hardening behaviour of a layered structure can be described well with the rule of mixtures, and that significant void growth has not occurred prior to necking. However, it has been generally accepted



that fracture in layered structures does not follow the rule of mixtures [Semiatin and Pichler (1979a), Lesuer et al. (1996)].

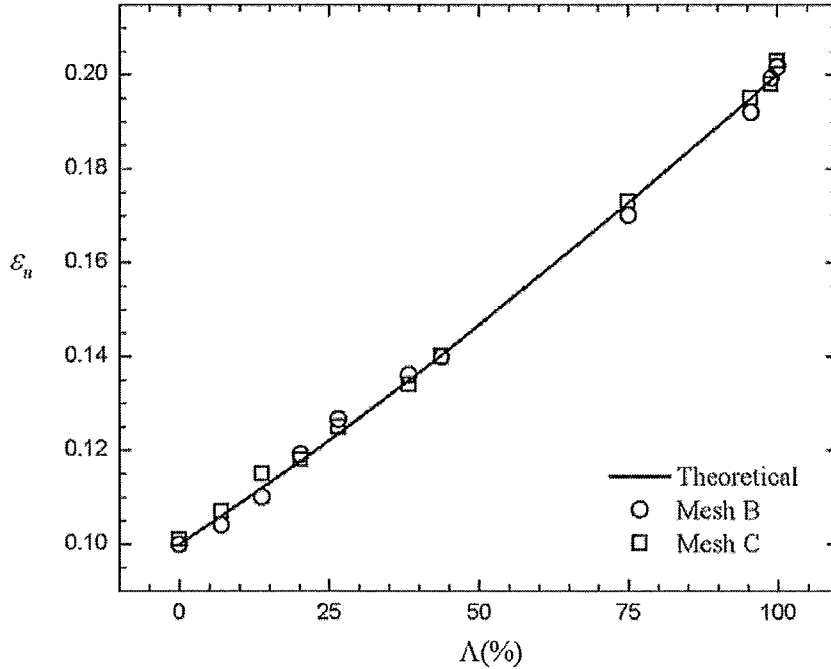


Figure 3.13: Predicted strain to necking  $\varepsilon_u$  for round tensile bars with various volume fraction of cladding  $\Lambda$ .

Figure 3.14 shows the predicted crack paths of the fractured tensile bars with various thickness fraction of cladding  $\Gamma$ , while Fig. 3.15 summarizes the simulated crack profiles. In Fig. 3.15, the thin black lines are those based on Mesh B and the thick red lines are those calculated from Mesh C. It is clear that the calculated subtle appearance of fracture surface is very sensitive to the mesh used and may even be an artefact of the mesh. However, the gain in fracture strain  $\varepsilon_f^*$  defined in Eq. 3.10, due to the cladding, is found to be not very sensitive to the mesh applied. Fig. 3.16 presents the predicted gain in fracture strain  $\varepsilon_f^*$  in round tensile bars with various cladding volume fraction  $\Lambda$ . It is observed that the increase in fracture strain is almost a linear function of the cladding volume fraction  $\Lambda$ . In Fig. 3.16, the gain curves in fracture strain for the layered round tensile bars are labelled as “Total” while “Core” is for those in the core cylinders only. It should be pointed out that the

predicted increase in ductility depends on the material and geometrical parameters used.

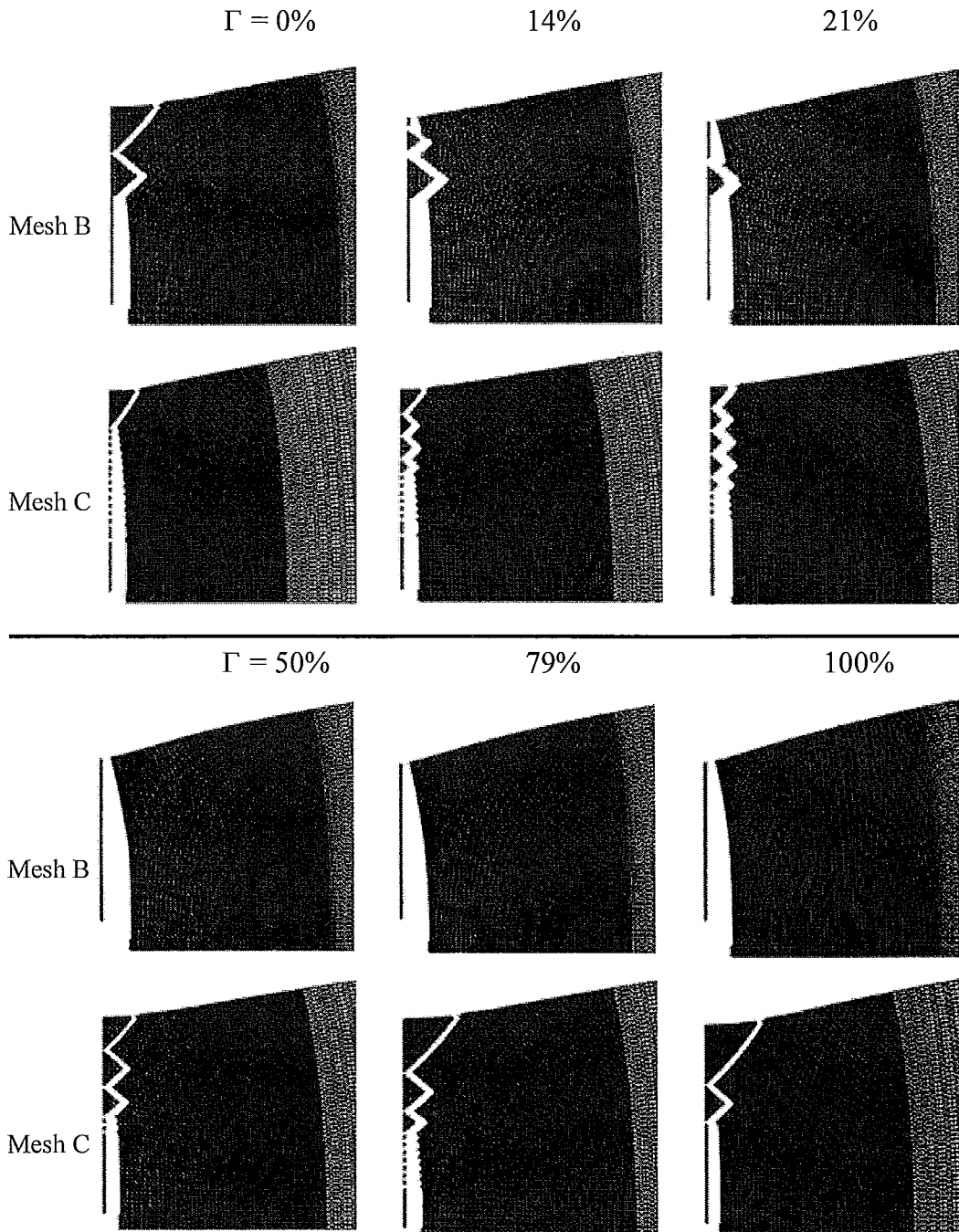


Figure 3.14: Predicted crack path of the fractured tensile bars with various thickness fraction of cladding  $\Gamma$ .

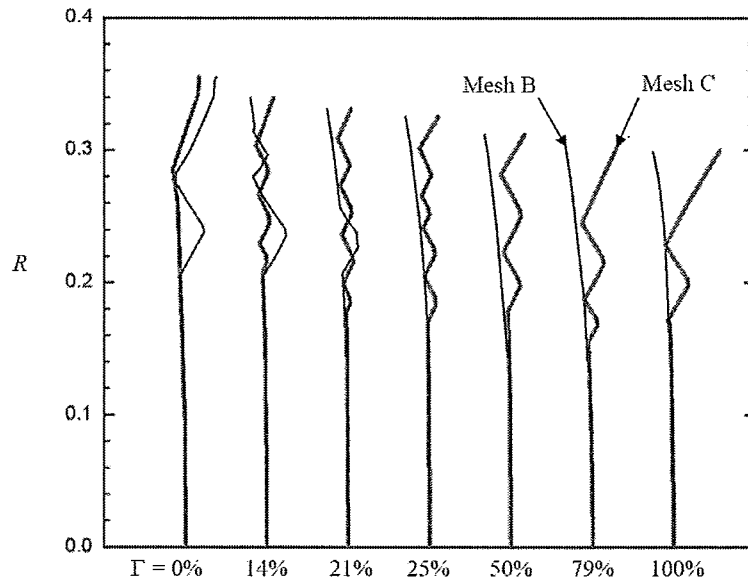


Figure 3.15: Predicted crack profile of fractured tensile bars with various thickness fraction of cladding  $\Gamma$ . Thin black lines are based on Mesh B while thick red lines are calculated from Mesh C.

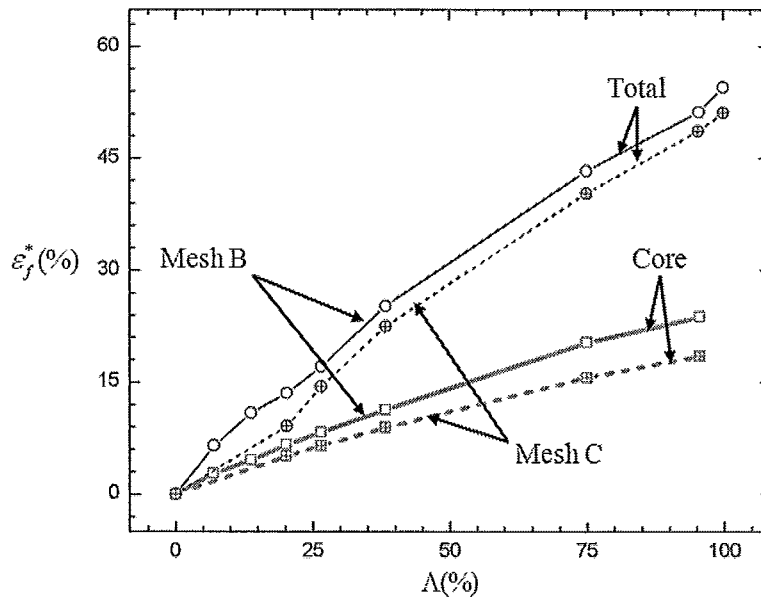


Figure 3.16: Predicted normalized fracture strain  $\varepsilon_f^*$  in round tensile bars with various volume fraction of cladding  $\Lambda$ .

The delay of fracture can be explained by showing how a cladding influences the hydrostatic/triaxial stress (see Eq. 3.13) inside the necked region.

$$\sigma_H = \frac{1}{3}(\sigma_{zz} + \sigma_{rr} + \sigma_{\theta\theta}), \quad (3.13)$$

Fig. 3.17 presents the hydrostatic/triaxial stress  $\sigma_H$  at the centre of the neck, where fracture initiates, as a function of axial strain  $\varepsilon$  in round tensile bars with various thickness fraction of cladding  $\Gamma$ . During tensile deformation, the triaxial tensile stress developed in the centre of neck is such as to assist the void growth. The greater the triaxial tensile stress the greater the degree of necking required. By cladding a ductile ring, necking is delayed which in turn slows down the development of the triaxial tensile stress  $\sigma_H$ . This implies that void nucleation is delayed until a sufficiently great degree of necking is developed. This results in a significantly larger strain which can be withstood before fracture. More specifically, triaxiality and true strain curves have been presented in Fig. 3.18. Triaxiality is defined as Eq. 3.14. Black thick dash line stands for triaxiality under homogeneous deformation.

$$T = \frac{\sigma_H}{\sigma_e}, \quad (3.14)$$

where  $\sigma_H$  is the hydrostatic stress,  $\sigma_e$  is the von Mises stress.

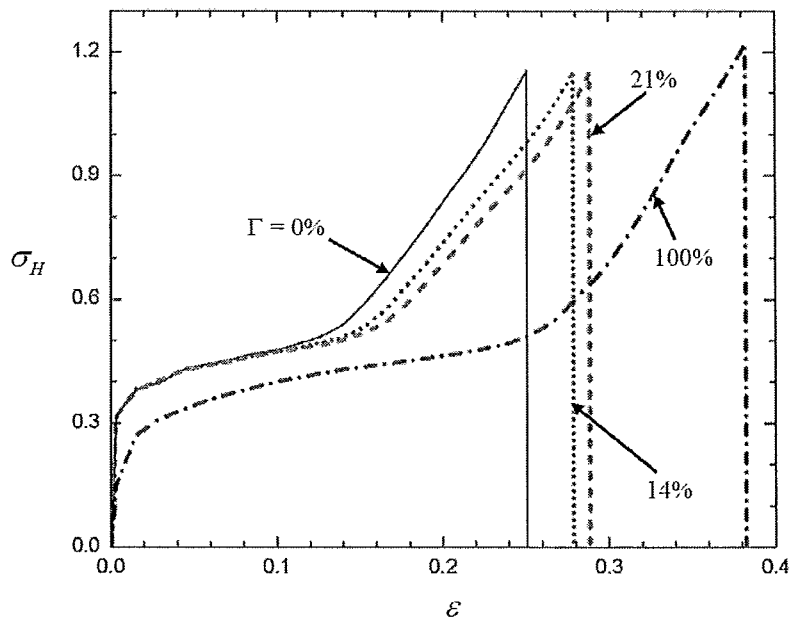


Figure 3.17: Predicted hydrostatic stress  $\sigma_H$  at the centre of neck in round tensile bars with various thickness fraction of cladding  $\Gamma$ .

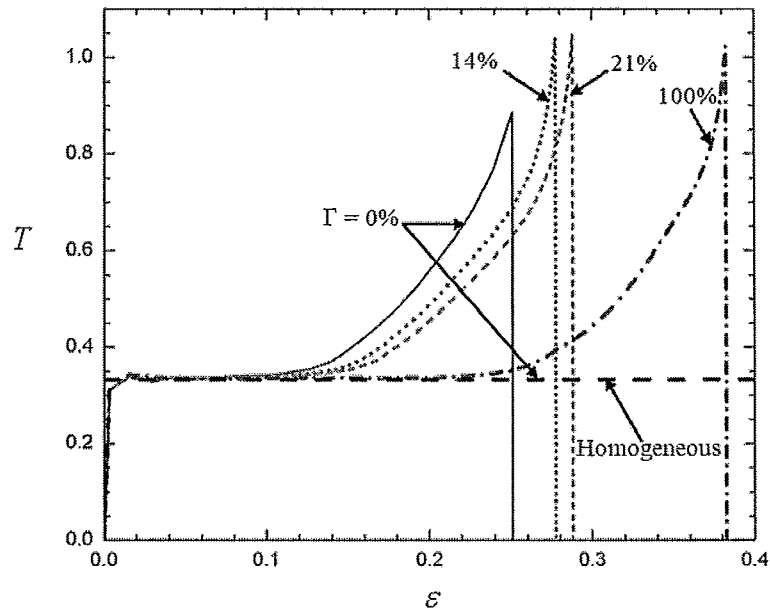


Figure 3.18: Predicted triaxiality  $T = \sigma_H / \sigma_e$  at the centre of neck under various thickness fraction of cladding  $\Gamma$ .

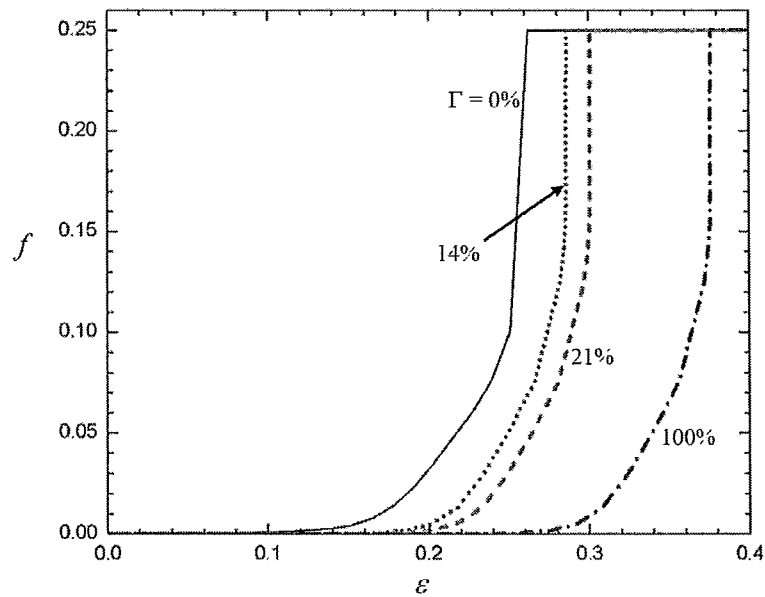


Figure 3.19: Predicted void volume fraction  $f$  at the centre of neck in round tensile bars with various thickness fraction of cladding  $\Gamma$ .

Figure 3.19 shows the predicted void volume fraction  $f$  at the centre of the neck under various claddings. It is clear that the claddings delay the nucleation, growth and coalescence of voids in the core cylinder.

In all the simulations reported above the ductile rings have been surrounded the core cylinders as shown in Fig. 3.2. In other words, the inner radius of a cladding tube always equals to the radius of the core cylinder. It is interesting to assess effects of topological arrangement of a cladding ring on the fracture strain in layered tensile bars. Fig. 3.20 presents the predicted effects of the cladding ring position  $R_i/R_0$  on fracture strain  $\varepsilon_f$  in round tensile bars with fixed cladding volume fraction  $\Lambda = 37.6\%$ . It is clear that the fracture strain in a layered tensile bar is sensitive to the topological arrangement of the cladding ring: The smaller the  $R_i/R_0$  is the greater the fracture strain  $\varepsilon_f$  can be reached. Numerical results in Fig. 3.20 indicate that the fracture strain could increase about 11% if the ductile ring is moved from the outmost to the innermost. It is interesting to note that for all the cases reported in Fig. 3.20, fracture is always initiated at the centre of the neck, regardless of the position of the ductile layer. This observation is mainly due to the significant constraint resulting from the axisymmetry, although it also depends on the values of the mechanical and geometrical parameters considered. As reported previously, the effects of cladding on necking can be accurately predicted based on the Considère criterion and the rule of mixtures (see Fig. 3.13). Since topological arrangement is not considered in the rule of mixtures, it is expected that topological arrangement should have no significant effect on necking. This observation is numerically confirmed by Fig. 3.21, which shows the predicted effect of cladding ring position  $R_i/R_0$  on necking strain  $\varepsilon_u$  in round tensile bars with fixed cladding volume fraction  $\Lambda = 37.6\%$ .

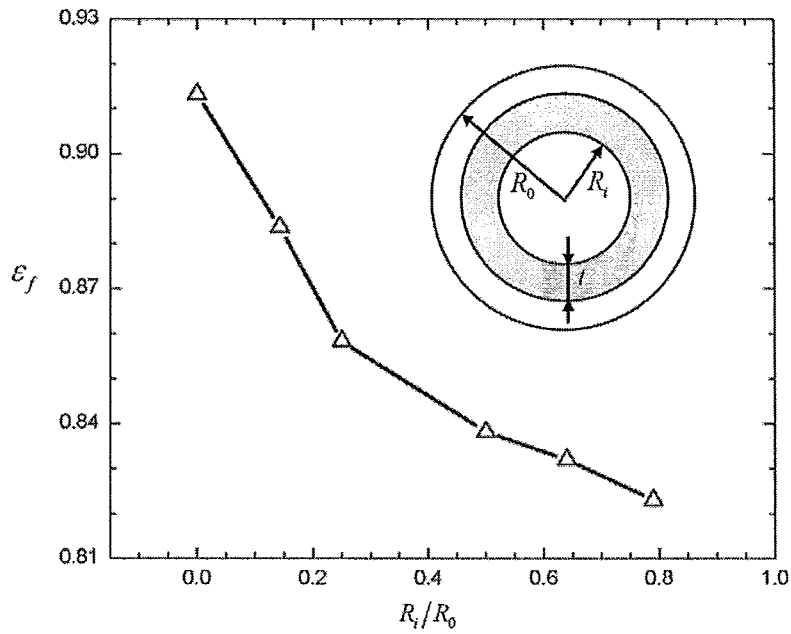


Figure 3.20: Predicted effect of cladding ring position  $R_i/R_0$  on fracture strain  $\epsilon_f$  in round tensile bars with fixed volume fraction of cladding  $\Lambda = 37.6\%$ . The inserted small figure shows the topological arrangement of the cladding ring (shaded area).

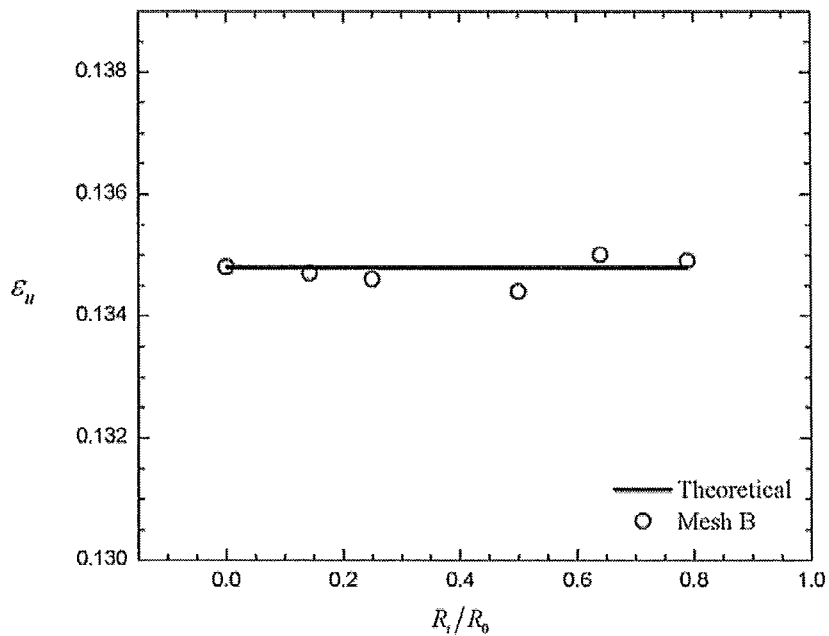


Figure 3.21: Predicted effect of cladding ring position  $R_i/R_0$  on necking strain  $\epsilon_n$  in round tensile bars with fixed volume fraction of cladding  $\Lambda = 37.6\%$ .

### 3.4 Summary

In this chapter, we have developed a detailed finite element analysis of co-axially layered round tensile bars. It has been demonstrated that cladding a ductile ring increases both the necking strain (see Fig. 3.13) and the fracture strain (see Fig. 3.16). The increase in necking strain has been found to be due to the fact that cladding a ductile ring enhances the overall work hardening for the layered round bars according to the rule of mixtures. Furthermore, the increase in necking strain slows down the development of the triaxial tensile stress (see Figs. 3.17 and 3.18), which delays the void nucleation and growth (see Fig. 3.19), and which in turn results in a significantly enhancement in ductility.

The effects of topological arrangement of cladding ring on necking and fracture have been investigated. It has been indicated that while a topological arrangement of cladding has no noticeable effect on necking (see Fig. 3.21), the topological arrangement of cladding significantly influences the fracture strain. More specifically, the smaller the  $R_i/R_0$  the greater the fracture strain  $\varepsilon_f$  can be reached (see Fig. 3.20).

We have carried out a detailed mesh sensitivity study. It should be pointed out that while the significant increase in both the necking strain and fracture strain is predicted with confidence, the calculated subtle change in appearance of fracture surface due to cladding is very sensitive to the mesh used (see Figs. 3.14 and 3.15) and may even be an artefact of the mesh.

While we have studied the effect of cladding on fracture only in round tensile bars, experimental work has shown that cladding increases the fracture strain under tension and enhances the ductility in sheet metals [Wagstaff et al. (2006)]. Numerical simulations of the effect of cladding on fracture in sheet metals will be presented in the next chapter.



## **Chapter 4 Enhanced ductility in clad tensile sheets**

### **4.1 Introduction**

Mechanical designs have been increasingly requiring that conflicting mechanical properties (such as strength and ductility) have to be simultaneously fulfilled. Therefore, it has been becoming more and more important to optimize microstructures to obtain specific combinations of properties for given applications. One approach for doing so has been to optimize the microstructure in a monolithic material either by developing a specific thermomechanical process or by modifying a precipitation sequence in terms of micro-additions. However, this traditional approach has been often limited by its flexibility and cost. A practical alternative to fulfil complex design requirements is to design composites in which the detailed microstructures and mechanical properties can be varied spatially in the overall structure. The strategy combining microstructural design and the spatial distribution of composition can provide a powerful tool for combining strength and ductility [Bouaziz et al. (2008)]. Among the wide range of composites, laminated composites have received a lot of attention. In this Chapter, we are going to carry out a detailed numerical study of the influence of cladding tensile sheets on fracture behavior. All simulations are performed by using ABAQUS/Explicit.

## 4.2 Problem formulation and method of solution

All simulations in this chapter are based on Gurson-Tvergaard-Needleman (GTN) damage model, which has been introduced in Chapter 2. The uniaxial true stress  $\sigma$  and true strain  $\varepsilon$  curve for the matrix material conforms to power-law as shown below:

$$\varepsilon = \begin{cases} \frac{\sigma}{E}, & \text{for } \sigma \leq \sigma_y, \\ \frac{\sigma_y}{E} \left( \frac{\sigma}{\sigma_y} \right)^n, & \text{for } \sigma > \sigma_y, \end{cases}, \quad (4.1)$$

where  $\sigma_y$  is the yield stress, and  $n$  is the strain hardening exponent.

We consider a plane strain tensile sheet, with initial length  $L_0$  and initial thickness  $t_0$  as shown in Fig. 4.1. We assume that the sheet consists of a core layer, with thickness  $\bar{t}_0$  and a clad layer, with thickness  $(t_0 - \bar{t}_0)$ . The thickness fraction of cladding  $\Gamma$  is thus defined as Eq. 4.2:

$$\Gamma = \frac{t_0 - \bar{t}_0}{t_0}, \quad (4.2)$$

The corresponding volume fraction of cladding  $\Lambda$  is the same as thickness fraction of cladding  $\Gamma$  due to the same width of both core and clad layers. Boundary conditions are set as Eq. 4.3 as followed :

$$\begin{cases} \dot{U}_x = \Delta U; \dot{U}_y = 0 & X = 0 \\ \dot{U}_x = -\Delta U; \dot{U}_y = 0 & X = L_0 \end{cases}, \quad (4.3)$$

where  $\Delta U$  is the displacement of left or right side. The average tensile strain is defined as Eq. 4.4:

$$\varepsilon = \ln(1 + \Delta L/L_0), \quad (4.4)$$

where  $L = 2\Delta U$  is the total displacement. The minimum cross-sectional areas of the whole specimen and core material only are calculated by Eqs. 4.5 and 4.6:

$$A_{min} = b \times t_{min}, \quad (4.5)$$

$$A_{min}^{core} = b \times \bar{t}_{min}, \quad (4.6)$$

where  $b$  is the unit width and set as '1'. The overall response of the tensile sheet under plane strain condition is presented in terms of the normalized tensile force  $F^*$  and normalized minimum cross-sectional area  $A^*$ :

$$F^* = \frac{F}{\sigma_y^{core} \times \bar{t}_0 + \sigma_y^{clad} \times (t_0 - \bar{t}_0)}, \quad (4.7)$$

$$A^* = \frac{A_{min}}{A_0} = \frac{t_{min}}{t_0}, \quad (4.8)$$

where  $F$  is the applied force, and  $\sigma_y^{core}$  and  $\sigma_y^{clad}$  are the yield stresses of core and clad materials, respectively. The ductility of the tensile sheet is measured in terms of the fracture strain:

$$\varepsilon_f = \ln \left( \frac{A_0}{A_f} \right), \quad (4.9)$$

where  $A_0$  is the original cross-sectional area and  $A_f$  is the minimum cross-sectional area at fracture. The gain in ductility  $\varepsilon_f^*$  due to cladding is defined as a function of the thickness fraction of cladding  $\Gamma$ :

$$\varepsilon_f^*(\Gamma) = \frac{\varepsilon_f(\Gamma) - \varepsilon_f(0)}{\varepsilon_f(0)}, \quad (4.10)$$

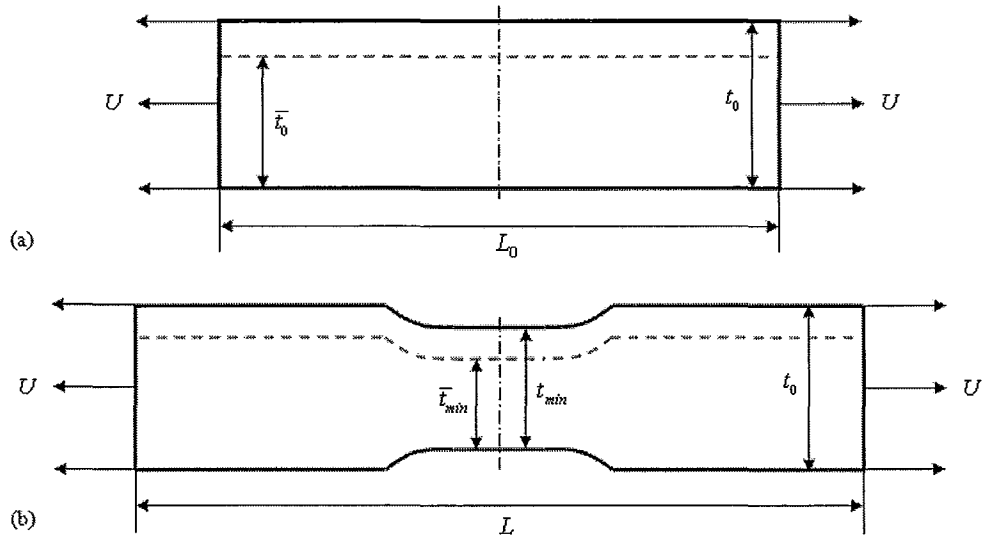


Figure 4.1: Schematic diagram of a sheet under plane strain tensile loading (a) Undeformed state; (b) Deformed state.

### 4.3 Results and discussions

The elastic-plastic properties of the matrix material of the core layer are specified by  $\sigma_y = 1$ ,  $\sigma_y/E = 0.0033$ ,  $\nu = 0.3$  and  $n = 10$ . We assume that there are no initial voids, and the parameters  $q_1 = 1.0$  and  $q_2 = 1.5$  are used in the yield function Eq. 2.9. The void nucleation is assumed to be plastic strain controlled, with the volume fraction  $f_N = 0.04$  of void nucleating particles, the mean strain for nucleation  $\varepsilon_N = 0.3$ , and the corresponding standard deviation  $s_N = 0.1$ . The final failure is taken to be characterized by the parameters  $f_c = 0.15$  and  $f_f = 0.25$ . The values of the material parameters for the clad layer are the same as those for the core layer except:  $\sigma_y = 0.6$ ,  $n = 5$  and  $\varepsilon_N = 0.5$ . Fig. 4.2 shows true stress and true strain curves for the core and clad materials under homogeneous uniaxial tension. It is clear that, compared to the core material, the clad material has relatively lower yielding stress but higher hardening. The aspect ratio of initial length to thickness is given by  $L_0/R_0 = 3$ . The applied velocity  $\Delta U = 0.0001/s$ .

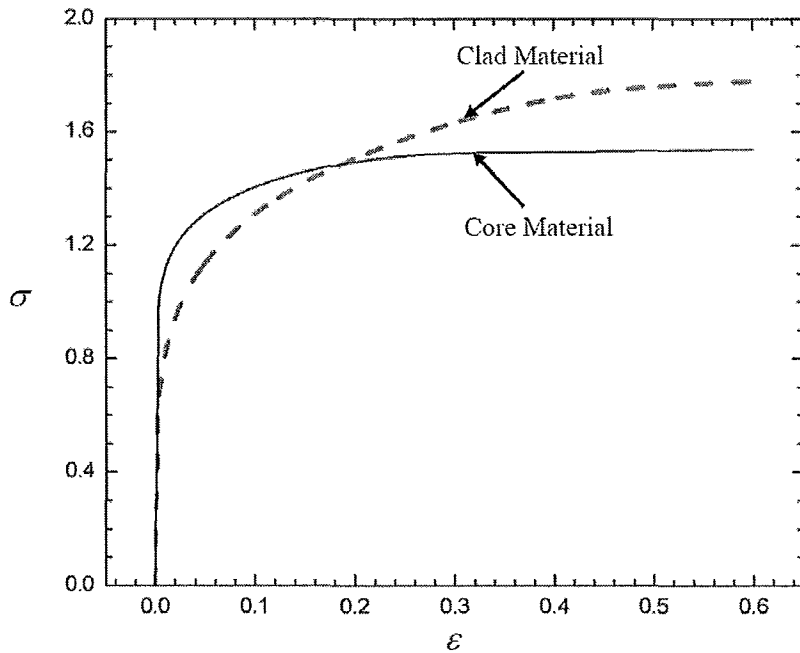


Figure 4.2: Uniaxial stress and strain curves of the core and clad materials.

It has been generally accepted that there is significant mesh sensitivity in a numerical simulation involving deformation localization and failure. In the present study, factors of mesh design including refined area, element aspect ratio, element type and total number of elements are of the most concern. We start with nailing down refined area by using coarse uniform meshes to approximately estimate how much length in tensile direction the shear bands will occupy before fracture. It is concluded that  $L_{refined}/L_0 = 0.2$  is sufficiently large to cover the critical deformation region. According to our investigation, final fracture pattern is very sensitive to element aspect ratio. It is investigated that the initial aspect ratios of element inside the refined area are set as 1.5, 2 and 2.5, respectively. For element type selection, considering the precision, efficiency and availability in element database of ABAQUS/Explicit, triangular plane strain element type is selected. In principle, the larger the number of elements, the higher the precision of the numerical results will be. However, considering the computational efficiency, total number of elements is limited to less than 50,000. Fig. 4.3 shows Mesh B with local refinement  $L_{refined}/L_0 = 0.2$  around the middle-plane, and with total of  $90 \times 60$  quadrilateral elements (90 in the  $X$ -direction and 60 in the  $Y$ -direction), each built up with four linear triangular elements (CPE3 in ABAQUS/Explicit). The initial aspect ratio of element in the refined area is 2. Likewise, mesh A consisting of  $70 \times 60$  quadrilateral elements (70 in the  $X$ -direction and 60 in the  $Y$ -direction) with local refinement and element aspect ratio 1.5; mesh C consisting of  $110 \times 60$  quadrilateral elements with local refinement and element aspect ratio 2.5; mesh D consisting of  $140 \times 80$  quadrilateral elements with local refinement and element aspect ratio 2.5; are also studied in the present work.

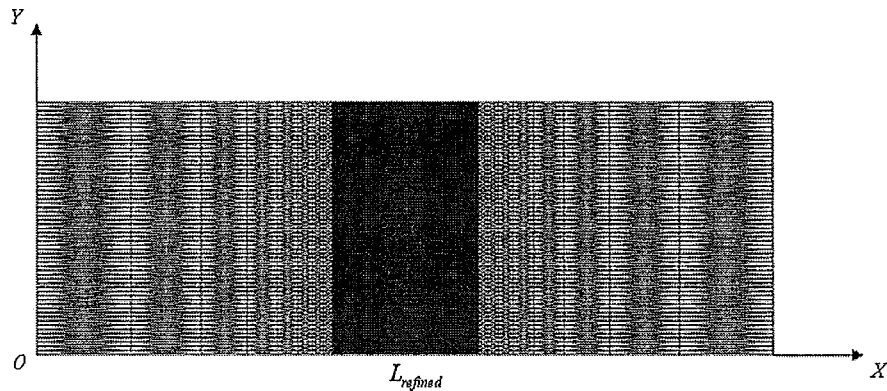


Figure 4.3: Mesh B with  $90 \times 60$  quadrilateral elements (90 in the  $X$ -direction and 60 in the  $Y$ -direction), each built up with four linear triangular elements (CPE3 in ABAQUS/Explicit); for bilayer baseline case, 48 in core layer and 12 in clad layer in the  $Y$ -direction.

Figure 4.4 shows a typical normalized tensile load and tensile strain curve and crack formation in a plane strain monolayer tensile sheet. It is noted that two strong shear bands are formed under straining followed by void nucleation at the intersection of shear bands and in the centre of the specimen. Open circles represent various stages of tensile strains 0.118, 0.122, 0.126, 0.127 and 0.128, respectively, which can be found in normalized minimum cross-sectional area  $A^*$  and tensile strain  $\varepsilon$  curve (see Fig. 4.5).

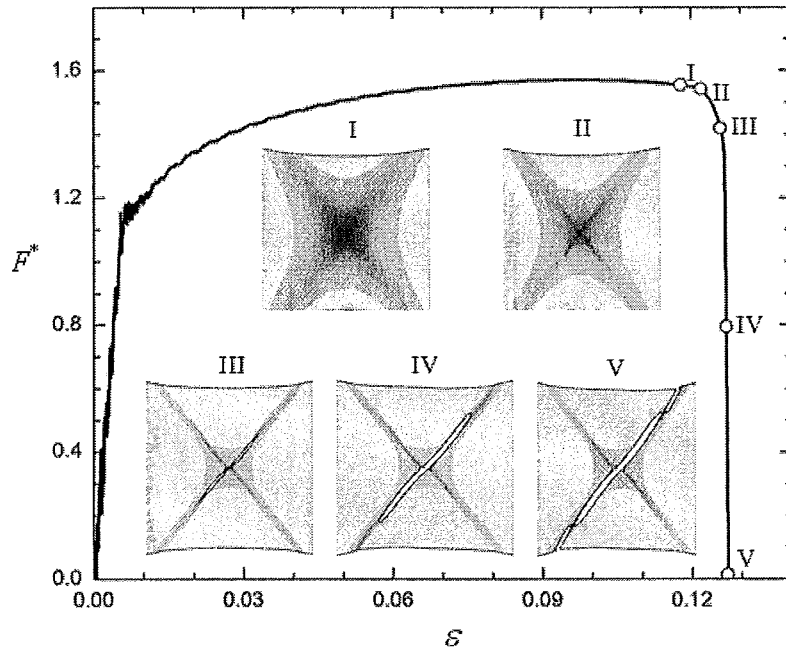


Figure 4.4: Normalized tensile force  $F^*$  and true strain  $\varepsilon$  curve; Crack formation in mono-layer sheet of core material ( $n=0.1$ ); Mesh B.

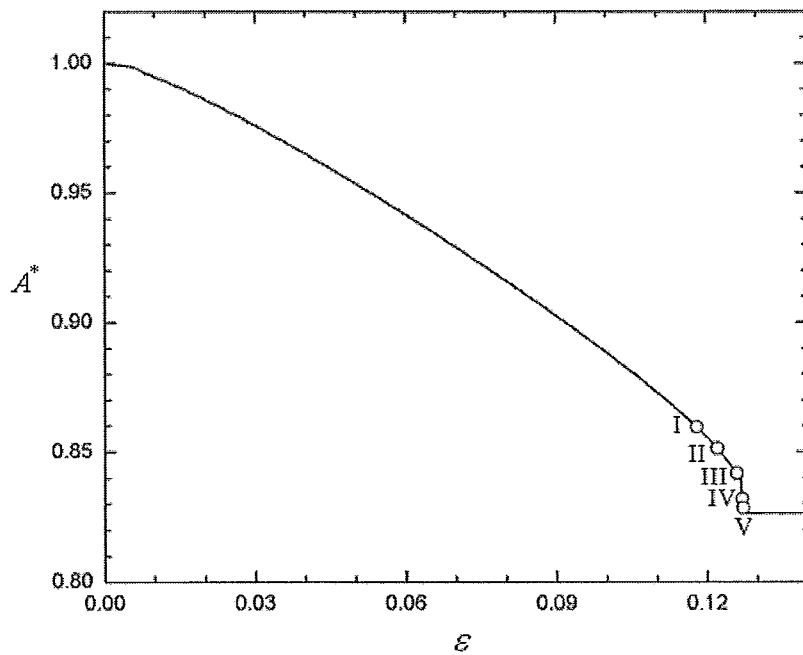


Figure 4.5: Normalized minimum cross-sectional area  $A^*$  and true strain  $\varepsilon$  curve; Tensile strains at various stage I, II, III, IV and V are 0.118, 0.122, 0.126, 0.127 and 0.128, respectively; Mesh B.

Figures 4.6, 4.7 and Figs. 4.8, 4.9 show the normalized tensile force  $F^*$  and normalized minimum cross-sectional area  $A^*$  as functions of the tensile strain  $\varepsilon = \ln(1 + \Delta L/L_0)$  for the tensile sheet with core material only ( $\Gamma = 0\%$ ) and clad material only ( $\Gamma = 100\%$ ). It is found that the force increases linearly with the imposed straining when the deformation is very small and the material is essentially in the elastic state. With continued straining, the force gradually reaches its maximum at around  $\varepsilon = 0.1$  in core material ( $\Gamma = 0\%$ ) only and  $\varepsilon = 0.2$  in clad material only ( $\Gamma = 100\%$ ) and then gradually decreases due to both the reduction of the cross-sectional area and the softening effect resulting from void nucleation and growth. Further straining results in a sharp “knee” on the force and strain curve. After the sharp knee, the burst of void nucleation and growth leads to a rapid drop in true stress which in turn results in a rapid loss of load carrying capacity for the tensile sheets. The development of necking and failure process can be more evidently presented in terms of the normalized minimum cross-sectional area and strain curve. When fracture occurs, neck development essentially stops as  $A_{min}$  is almost a constant, which confirmed Tvergaard and Needleman’s argument [Tvergaard and Needleman (1984)] that the reduction in area at fracture is a representative measure of the onset of macroscopic fracture in tensile test. Curves of tensile force and strain as well as normalized minimum cross-sectional area and strain by using Mesh B, Mesh C and Mesh D are observed to be very close, however Mesh B and Mesh D are finally determined to be used in the rest of the present study due to the fact that they have different element aspect ratios but similar fracture responses. Further explanation will be presented after studying fracture patterns of using various meshes.



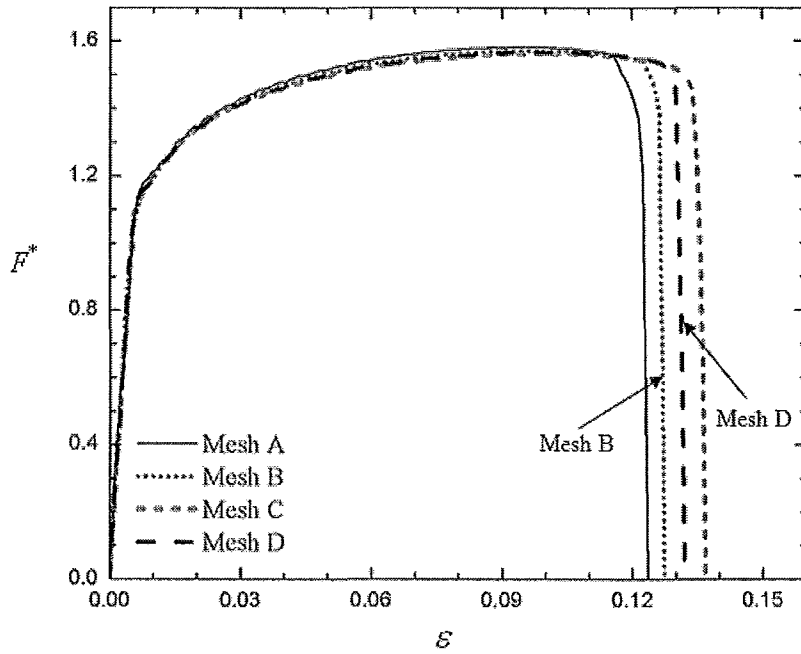


Figure 4.6 Predicted normalized force  $F^* = F/(\sigma_{y\_core} \times A_0)$  and tensile strain  $\varepsilon = \ln(1 + \Delta L/L_0)$  curve for monolayer sheet of core material ( $n=0.1$ ).

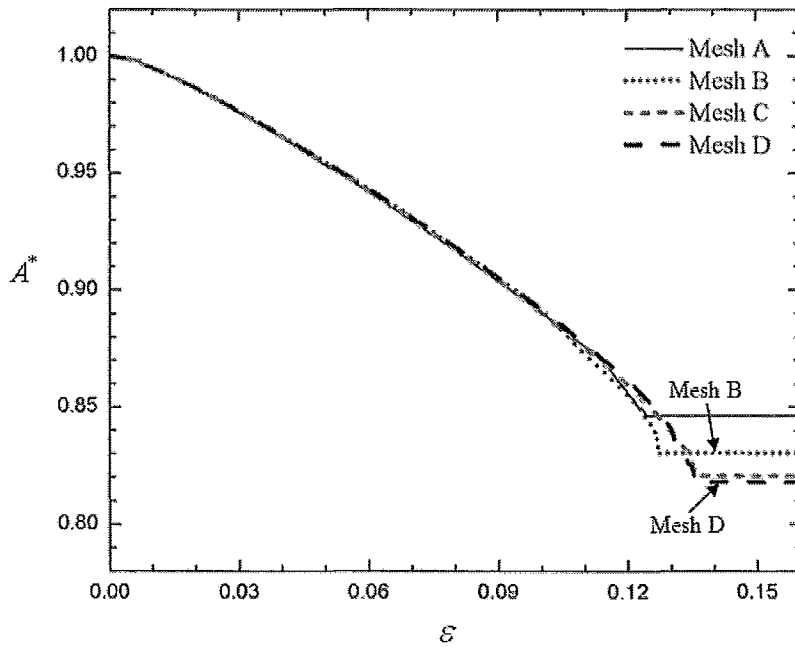


Figure 4.7: Predicted normalized minimum cross-sectional area  $A^* = A_{min}/A_0$  and tensile strain  $\varepsilon$  curve for monolayer sheet of core material ( $n=0.1$ ).

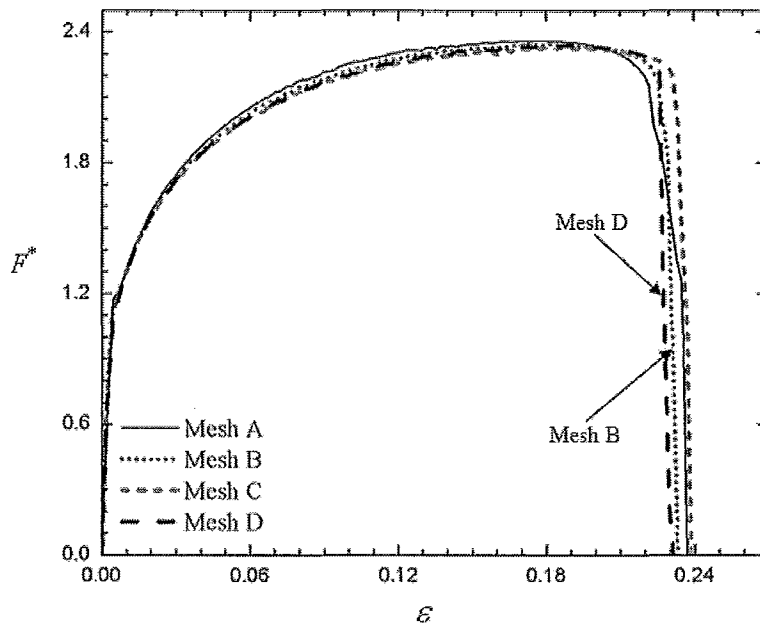


Figure 4.8: Predicted normalized force  $F^* = F / (\sigma_{y\_clad} \times A_0)$  and tensile strain  $\varepsilon$  curve for monolayer sheet of clad material ( $n=0.2$ ).

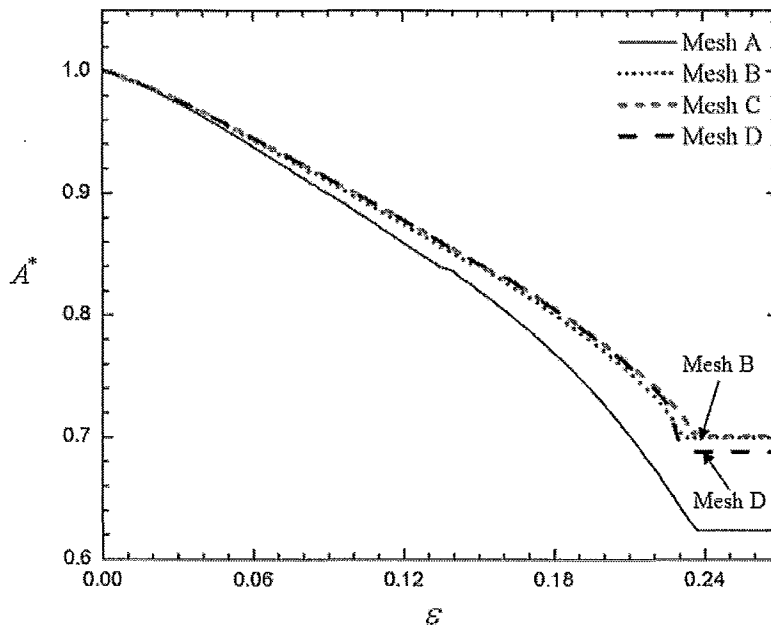


Figure 4.9: Predicted normalized minimum cross-sectional area  $A^*$  and tensile strain  $\varepsilon$  curve for monolayer sheet of clad material ( $n=0.2$ ).

Figure 4.10 presents different crack patterns by using various meshes. It is noted that two crossed shear bands are formed around middle plane and followed by void initiation at the center of the specimen. Crack propagates along one dominated shear band through the specimen until it is completely fractured.

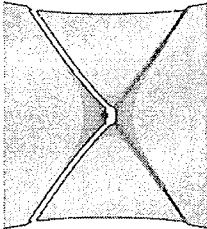
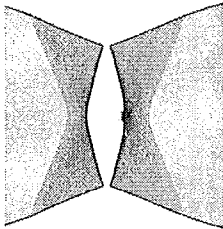
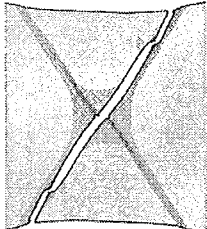
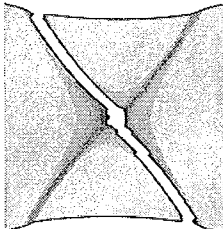
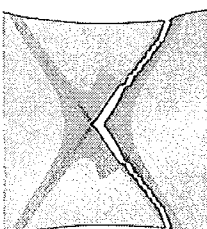
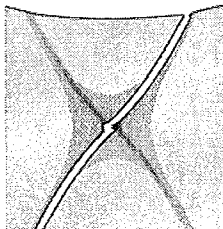
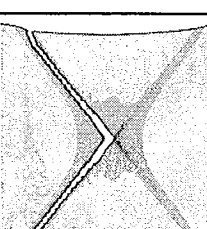
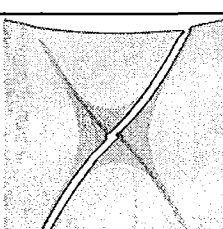
	Core material (n=0.1)	$\varepsilon_f$	Clad material (n=0.2)	$\varepsilon_f$
Mesh A		0.167		0.464
Mesh B		0.186		0.357
Mesh C		0.198		0.357
Mesh D		0.201		0.346

Figure 4.10: Predicted crack shapes of fractured tensile sheets by using different meshes.

We proceed by studying the effects of cladding on fracture in layered tensile sheets. Figs. 4.11 and 4.12 show the normalized tensile force  $F^*$  and normalized minimum cross-sectional area  $A^*$  versus tensile strain  $\varepsilon$  curves, respectively. The forces are calculated by summation of the reaction forces at  $X = 0$  or  $X = L_0$ . It is observed that cladding increases the normalized flow stress and the strain at which the applied force reaches its maximum. This implies that cladding increases the strain when necking occurs. It is also found from Figs. 4.11 and 4.12 that cladding delays crack initiation (open triangles indicate the initiation of crack). Furthermore, from Fig. 4.12, the maximum reduction in area, indicated by the horizontal  $A^*$  lines, increases with increasing cladding. This means that the ductility is enhanced by cladding a ductile layer on the monolithic material.

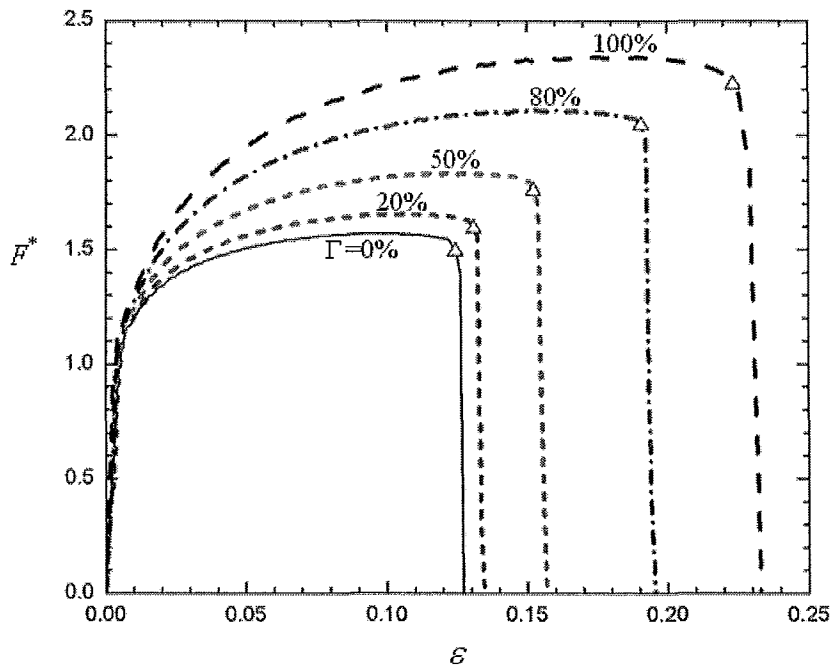


Figure 4.11: Predicted normalized force  $F^* = F / (A_0^{core} \times \sigma_y^{core} + A_0^{clad} \times \sigma_y^{clad})$  and tensile strain  $\varepsilon$  curve for various thickness fraction of cladding  $\Gamma$  by using Mesh B.

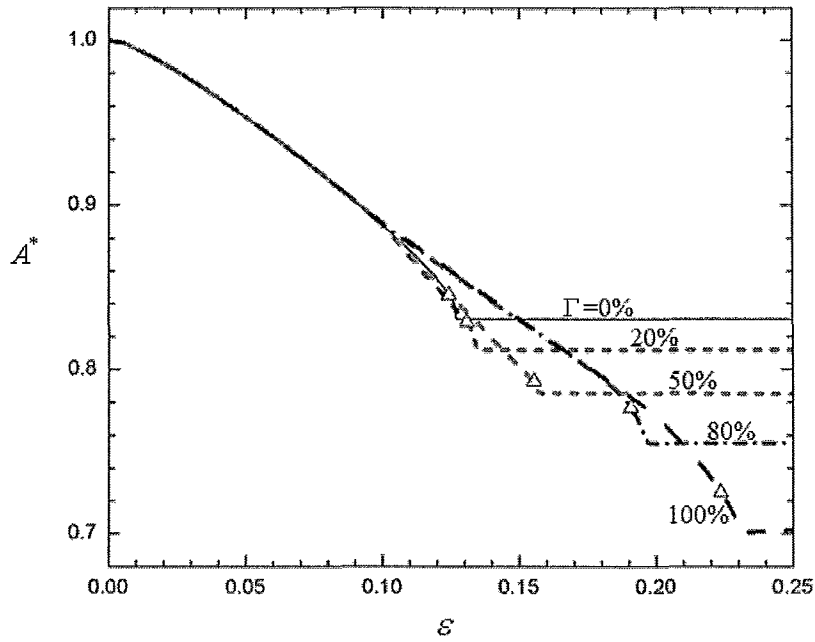


Figure 4.12: Predicted normalized minimum cross-sectional area  $A^*$  and tensile strain  $\varepsilon$  curve for various thickness fraction of cladding  $\Gamma$  by using Mesh B.

The predicted effect of cladding on necking is more clearly shown in Fig. 4.13. Numerical results indicate that the predicted necking strain is insensitive to the meshes used. Fig. 4.13 also includes the necking strains based on the Considère-type criterion:

$$\frac{d\bar{\sigma}_a}{d\varepsilon} = \bar{\sigma}_a, \quad (4.11)$$

Here, the averaged flow stress  $\bar{\sigma}_a$  for the tensile sheet is calculated from the rule of mixtures:

$$\bar{\sigma}_a = (1-\Gamma)\bar{\sigma}_{\text{core}} + \Gamma\bar{\sigma}_{\text{clad}}, \quad (4.12)$$

where  $\bar{\sigma}_{\text{core}}$  and  $\bar{\sigma}_{\text{clad}}$  are the flow stresses for the core layer and clad layer, respectively. The excellent agreement between the theoretical prediction and the numerical simulations indicates that the overall hardening behaviour of a layered structure can be described well with the rule of mixtures, and that significant void growth has not occurred prior to necking.

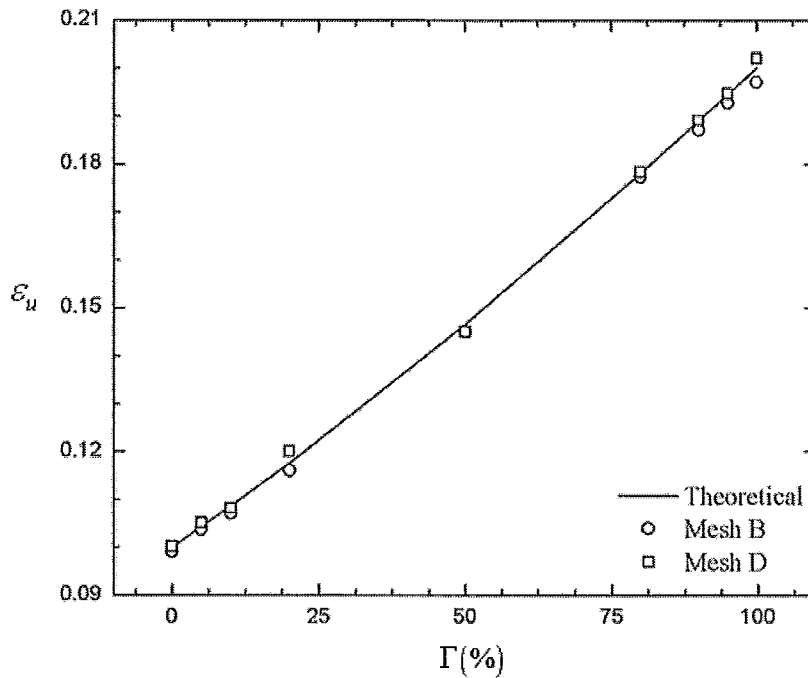


Figure 4.13: Predicted uniform strain and thickness fraction of cladding  $\Gamma$  curve.

Figures 4.14 and 4.15 present fracture formation under various thickness fraction of cladding. General conclusion is that crack always initiates from core material. More specifically, in monolayer structure, e.g.  $\Gamma = 0\%, 100\%$ , crack initiates at the centre of the specimen and propagates toward both top and bottom surfaces along one dominated shear band while in bilayer structure crack occurs in core material close to interface along one dominated shear band. The propagation of crack in bilayer structures has two steps: The crack first propagates in two directions along shear band until it propagates through the whole core layer and then it further walks into clad layer until the specimen is fully fractured.

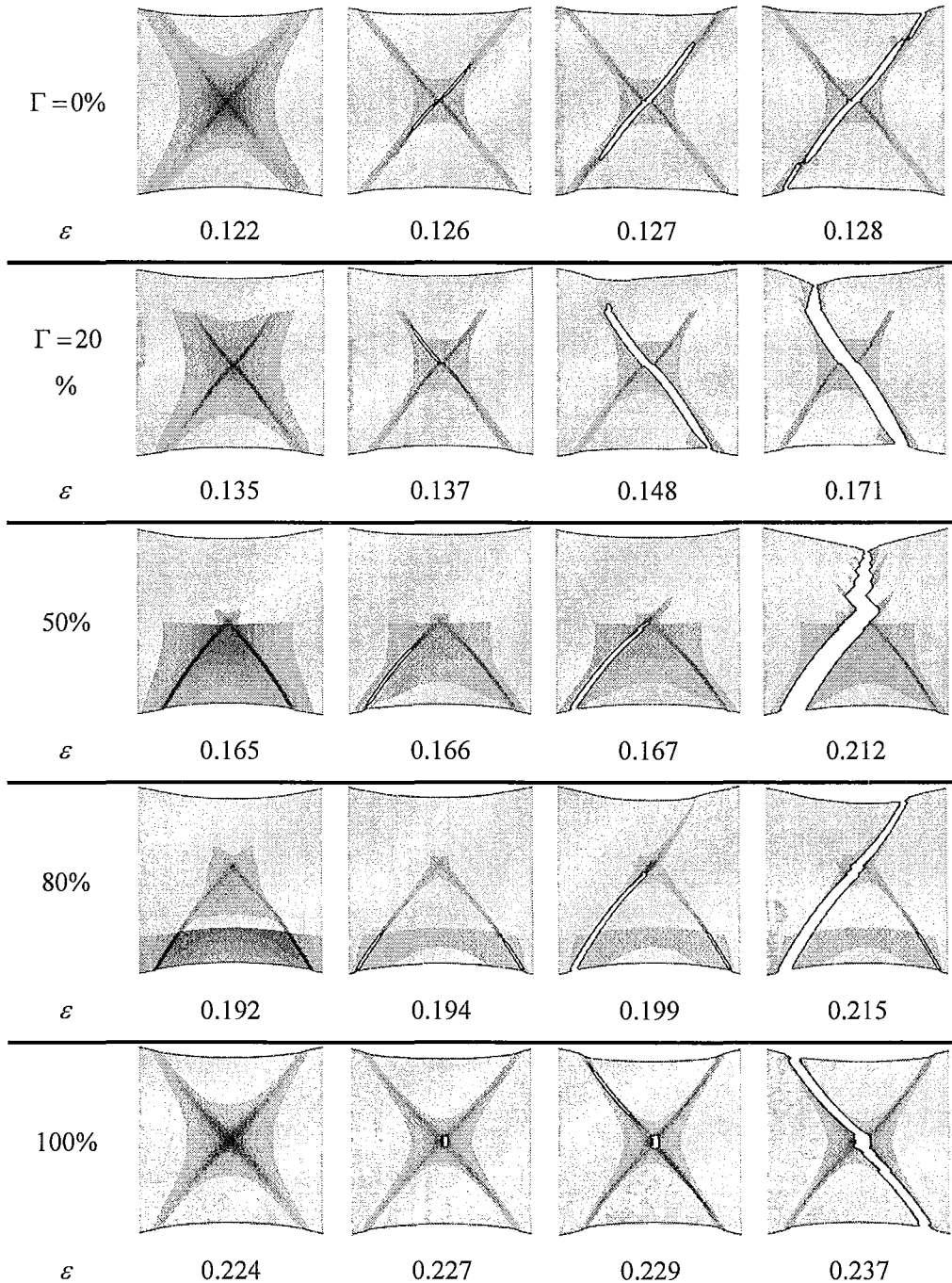


Figure 4.14: Predicted crack formation under various thickness fraction of cladding  $\Gamma$  curve by using Mesh B.

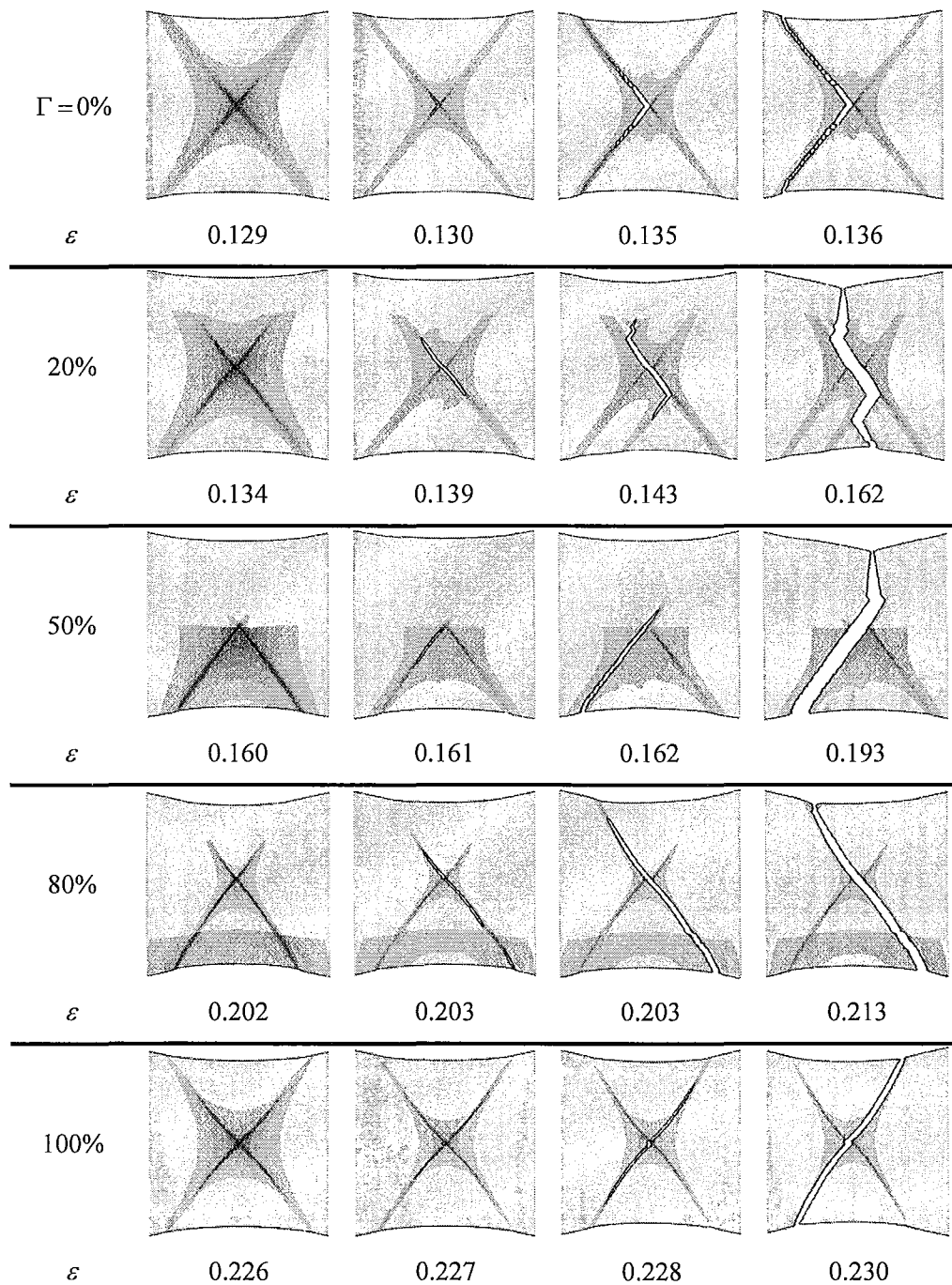


Figure 4.15: Predicted crack formation under various thickness fraction of cladding  $\Gamma$  curve by using Mesh D.



The gain curves in fracture strain for the layered tensile sheets by using Mesh B and Mesh D are presented in Fig. 4.16, in which “Total” and “Core” are labeled as whole specimen and core layer only. It is observed that when the thickness fraction of cladding is less than 50%, the gain fracture strain curves are almost linear according to our study. Also noted is that when thickness fraction of cladding is 20%, fracture strain is gained 10% by using mesh B and 20% by using Mesh D.

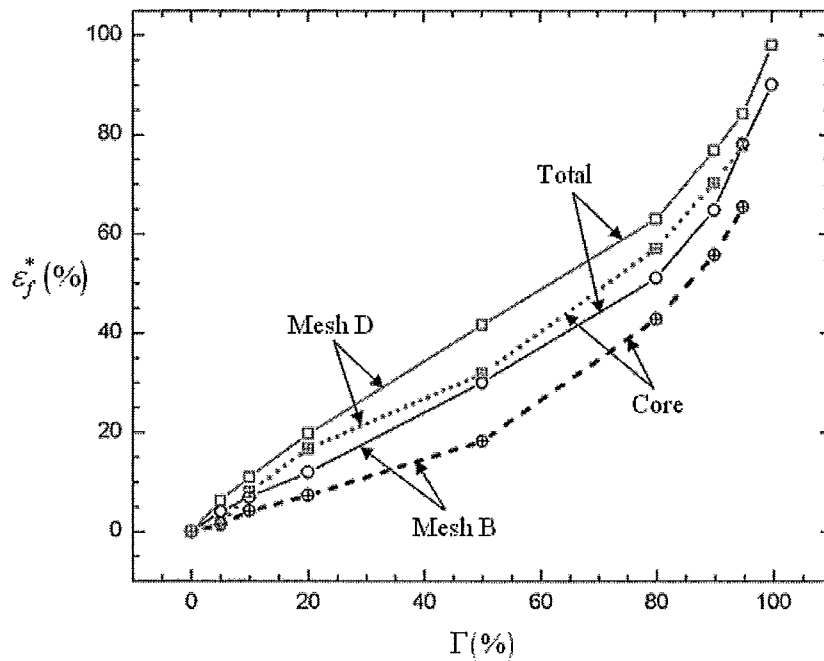


Figure 4.16: Predicted gained fracture strain  $\varepsilon_f^*$  and thickness fraction of cladding  $\Gamma$  curve.

#### 4.4 Summary

We have carried out a detailed finite element analysis of clad tensile sheets. It has been demonstrated that cladding increases both necking strain and fracture strain. The necking strain is predicted quite well by using Considère criterion and the rule of mixtures. The increase of necking strain further delays void nucleation and void growth and thus results in enhancement in ductility.

## Chapter 5 Effects of superimposed hydrostatic pressure on fracture in tensile sheets

### 5.1 Introduction

Extensive experiments have been conducted to study the effects of superimposed hydrostatic pressure on the deformation and fracture mechanisms in monolithic metals, most of which are of circular cross-section under tension [Bridgeman, (1952), Pugh and Green (1964), French and Weinrich (1973, 1975, 1977), French, et al. (1973), Brownrigg, et al. (1983), Korbel, et al. (1984), Spitzig and Richmond (1984), Ashby, et al. (1985), Kao, et al. (1989,1990)] and reviewed by Lewandowski and Lowhaphandu (1998). Very recently, numerical work was investigated on effects of superimposed hydrostatic pressure on fracture in round bars under tension by Peng et al. (2009). From their study, it is demonstrated that superimposed hydrostatic pressure  $p$  increases the fracture strain and changes the fracture surface from cup and cone mode to a slant structure. Although there is a lot of attention focused on superimposed hydrostatic pressure effect on tensile round specimens, very little experimental work was conducted on sheet metals, which are more commercially valuable in industry. Also, there is no numerical work reported on effects of superimposed hydrostatic pressure on tensile sheets according to our investigation. Due to the fact that the predicted results obtained from round tensile bars under superimposed hydrostatic pressure cannot be used to predict the deformation and fracture behavior of tensile sheets because the geometries and stress states are quite different in between a round bar and a sheet metal, it is important to study the mechanisms of fracture in sheet specimens under superimposed hydrostatic pressure both experimentally and numerically. Weinrich and French (1976) published their research on the influence of superimposed hydrostatic pressure on tensile sheet specimens of  $\alpha$ -brass,  $\alpha$ - $\beta$  brass and copper and found that at low pressures common fracture mode occurred in all materials with formation of intense shear deformation followed by fracture due to development of void-sheets while at high pressure a “V-shape” trough along one face of the specimen was formed and extended through the specimen leading to fracture. Gimple, et al. (2001) examined the damage evolution

and fracture behavior of two aluminum automotive alloys AA5754 and AA6111 under superimposed hydrostatic pressure. They found that the application of pressure decreased the amount of damage present in all samples and increased the ductility. Fig. 5.1 shows a transition of the fracture surface from P-type mode under atmospheric pressure to C-type mode under high pressure. In this chapter, we will carry out a detailed numerical study of the influence of superimposed hydrostatic pressure on fracture in tensile sheets by using finite element software ABAQUS/Explicit.

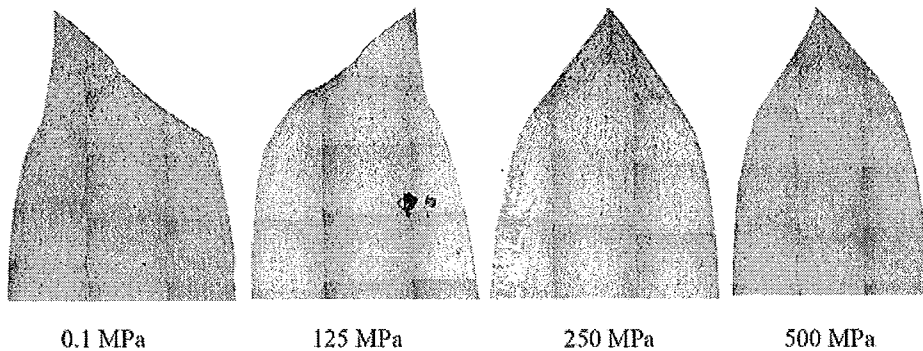


Figure 5.1: The appearance of the fractured tensile AA5754-O sheets under applied pressure, Gimple (2001).

## 5.2 Problem formulation and method of solution

All simulations in this chapter are based on Gurson-Tvergaard-Needleman (GTN) damage model, which has been introduced in Chapter 2. The uniaxial true stress  $\sigma$  and true strain  $\varepsilon$  curve for the matrix material conforms to power-law as shown in Eq. 5.1:

$$\varepsilon = \begin{cases} \frac{\sigma}{E}, & \text{for } \sigma \leq \sigma_y, \\ \frac{\sigma_y}{E} \left( \frac{\sigma}{\sigma_y} \right)^n, & \text{for } \sigma > \sigma_y, \end{cases}, \quad (5.1)$$

where  $\sigma_y$  is the yield stress, and  $n$  is the strain hardening exponent.

We consider a plane strain tensile sheet, with initial length  $L_0$  and initial thickness  $t_0$ , under superimposed hydrostatic pressure as shown in Fig. 5.2.  $X = \frac{L_0}{2}$  is the middle plane. Tensile displacements are applied at  $X = 0, L_0$ .  $X = 0, L_0$  are set as y-direction fixed and necking is correspondingly triggered at the middle plane  $X = \frac{L_0}{2}$ .

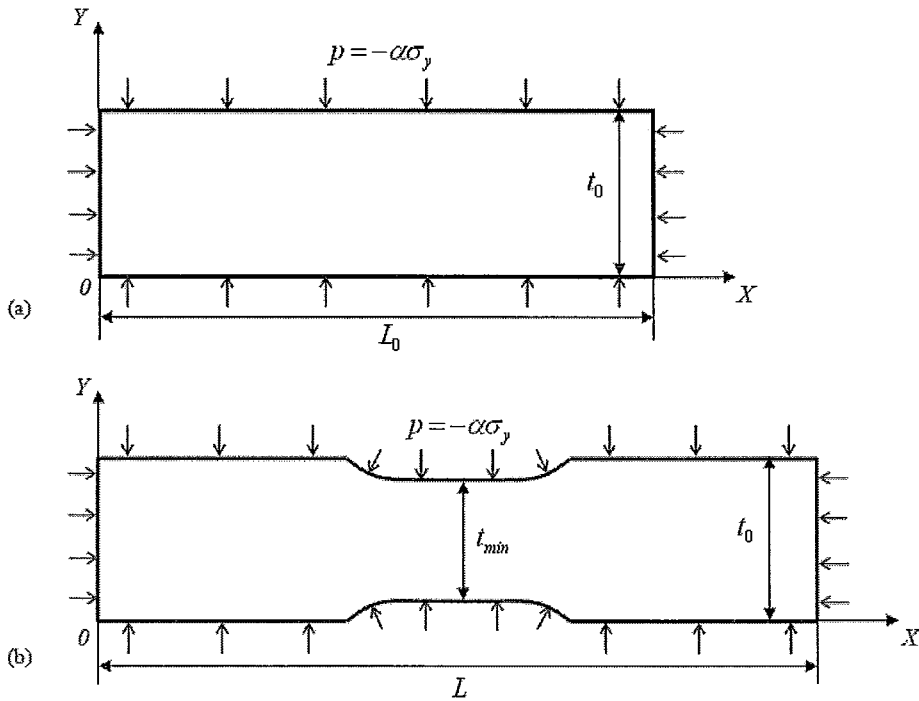


Figure 5.2: Schematic diagram of a sheet under plane strain tensile loading (a) Undeformed state; (b) Deformed state.

The sequence of plane strain tension under superimposed hydrostatic pressure is modeled as a two-step process. The first step is pressurization (see Fig. 5.2a). During this step the pressure fluid has access to all surfaces of the specimen, and the magnitude of the pressure is gradually increased up to a desired level.

$$p = -\alpha\sigma_y, \quad (5.2)$$

where  $\alpha$  is a positive value,  $\sigma_y$  is yield stress of matrix material. The second step is to apply tensile displacement  $\Delta L$  (or velocity  $V$ ) at  $X=0, L_0$  at the desired level of superimposed hydrostatic pressure  $p = -\alpha\sigma_y$  (see Fig. 5.2b).

### 5.3 Results and discussions

The elastic-plastic properties of the matrix material are specified by  $\sigma_y = 1$ ,  $\sigma_y/E = 0.0033$ ,  $\nu = 0.3$  and  $n = 10$ . We assume that there are no initial voids, and the parameters  $q_1 = 1.0$  and  $q_2 = 1.5$  are used in the yield function Eq. 2.9. The void nucleation is assumed to be plastic strain controlled, with the volume fraction  $f_N = 0.04$  of void nucleating particles, the mean strain for nucleation  $\varepsilon_N = 0.3$ , and the corresponding standard deviation  $s_N = 0.1$ . The final failure is taken to be characterized by the parameters  $f_c = 0.15$  and  $f_f = 0.25$ . We further assume that the initial length to thickness ratio is given by  $L_0/t_0 = 3$ . The applied velocity  $V = 0.0001/s$ .

Significant mesh sensitivity is usually expected in a numerical simulation involving deformation localization and failure. In the present study, factors of mesh design including refined area, element aspect ratio, element type and total number of elements are of the most concern. We start with nailing down refined area by using coarse uniform meshes to approximately estimate how much length in tensile direction the shear bands will occupy before fracture. It is concluded that  $L_{refined}/L_0 = 0.2$  is sufficiently large to cover the critical deformation region. According to our investigation, final fracture pattern is very sensitive to element aspect ratio. It is investigated that the initial aspect ratios of elements inside the refined area are set as 2 and 2.5. For element type selection, considering the precision, efficiency and availability in element database of ABAQUS/Explicit, plane strain triangular element type is selected. In principle, the larger the number of elements, the higher the precision of the numerical results will be. However, considering the computational efficiency, total number of elements is limited to less than 50,000. Fig. 5.3 shows Mesh A with local refinement  $L_{refined}/L_0 = 0.2$  around the middle-plane, and with total of  $90 \times 60$  quadrilateral elements (90 in the  $X$ -direction and 60 in the  $Y$ -direction), each built up with four linear triangular elements (CPE3 in ABAQUS/Explicit). The initial aspect ratio of element in the refined area is 2.

Likewise, mesh B, consisting of  $140 \times 80$  quadrilateral elements (140 in the  $X$ -direction and 80 in the  $Y$ -direction) with local refinement and element aspect ratio 2.5 is also studied in the present work.

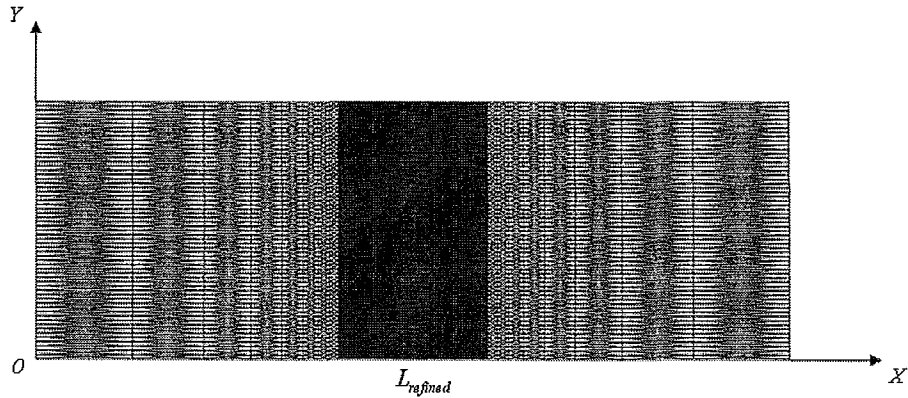


Figure 5.3: Mesh A with  $90 \times 60$  quadrilateral elements (90 in the  $X$ -direction and 60 in the  $Y$ -direction), each built up with four linear triangular elements (CPE3 in ABAQUS/Explicit).

We first consider the tensile sheet under plane strain tension without a superimposed hydrostatic pressure ( $p = 0$ ). Fig. 5.4 presents the calculated normalized tensile force  $F^*$  as a function of the tensile true strain  $\varepsilon = \ln(1 + \Delta L/L_0)$ , where  $\Delta L$  is the displacement.

$$F^* = F / (\sigma_y A_0), \quad (5.3)$$

where  $A_0$  is the initial cross-sectional area. In plane strain tension  $A_0$  is equal to  $t_0$ . It is found that the force increases linearly with the imposed straining when the deformation is very small and the material is essentially in the elastic state. With continued straining, the force gradually reaches its maximum at around  $\varepsilon = 0.1$  and then decreases due to both the reduction of the cross-sectional area and the softening effect resulting from void nucleation and growth.

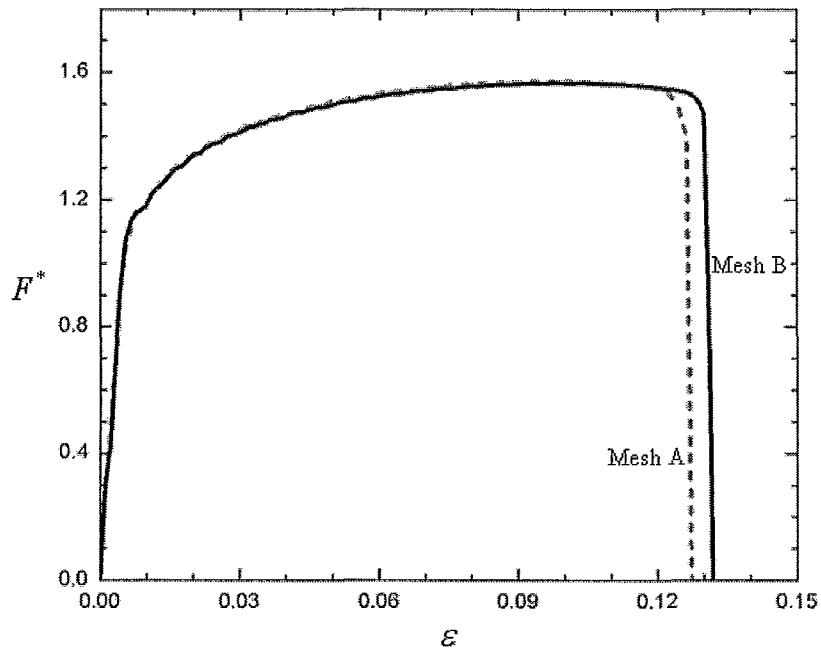


Figure 5.4: Predicted normalized force  $F^* = F/(\sigma_y A_0)$  and tensile strain  $\varepsilon = \ln(1 + \Delta L/L_0)$  curve for the monolayer sheet under atmospheric pressure ( $p = 0$ ).

The development of necking and failure processes can be more evidently presented in terms of the normalized minimum cross-sectional area  $A_{min}$  versus tensile strain  $\varepsilon$ . In plane strain tension  $A_{min}$  is equal to  $t_{min}$ . Fig. 5.5 shows the calculated normalized minimum cross-sectional area  $A_{min}$  and tensile strain  $\varepsilon$  curve. It is interesting to note that when fracture occurs, neck development essentially stops as a constant value.



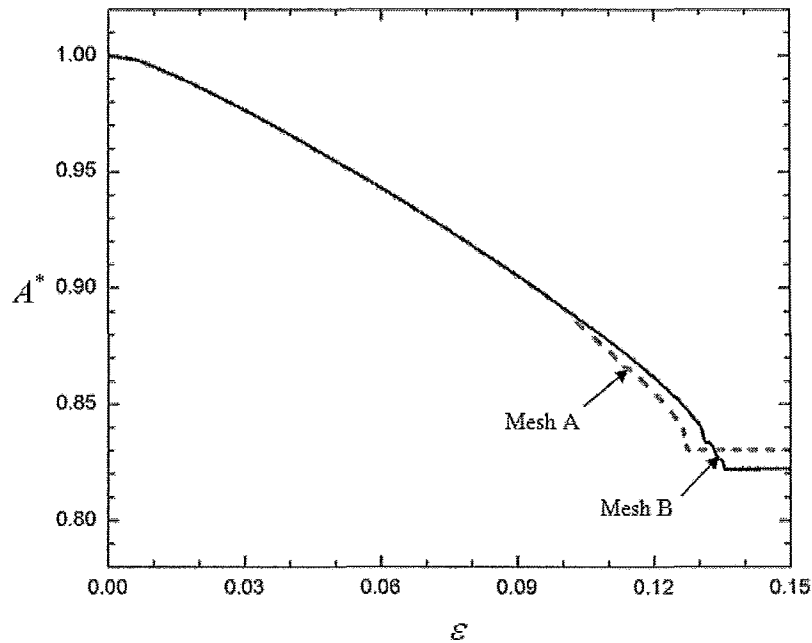


Figure 5.5: Predicted normalized minimum cross-sectional area  $A^* = A_{min}/A_0$  and tensile strain  $\varepsilon = \ln(1 + \Delta L/L_0)$  curve for the monolayer sheet under atmospheric pressure ( $p = 0$ ).

Crack patterns of Mesh A and Mesh B at various deformation stages under atmospheric pressure  $p = 0$  are shown in Fig. 5.6. Figs. 5.7 and 5.8 present crack evolution under various superimposed hydrostatic pressures using Mesh A and Mesh B, respectively. Our numerical results show that shear band formation is delayed due to superimposed hydrostatic pressure which indicated that the applied pressures influence the onset of localization. Furthermore, fracture initiation is also delayed due to the retardation of shear band formation.

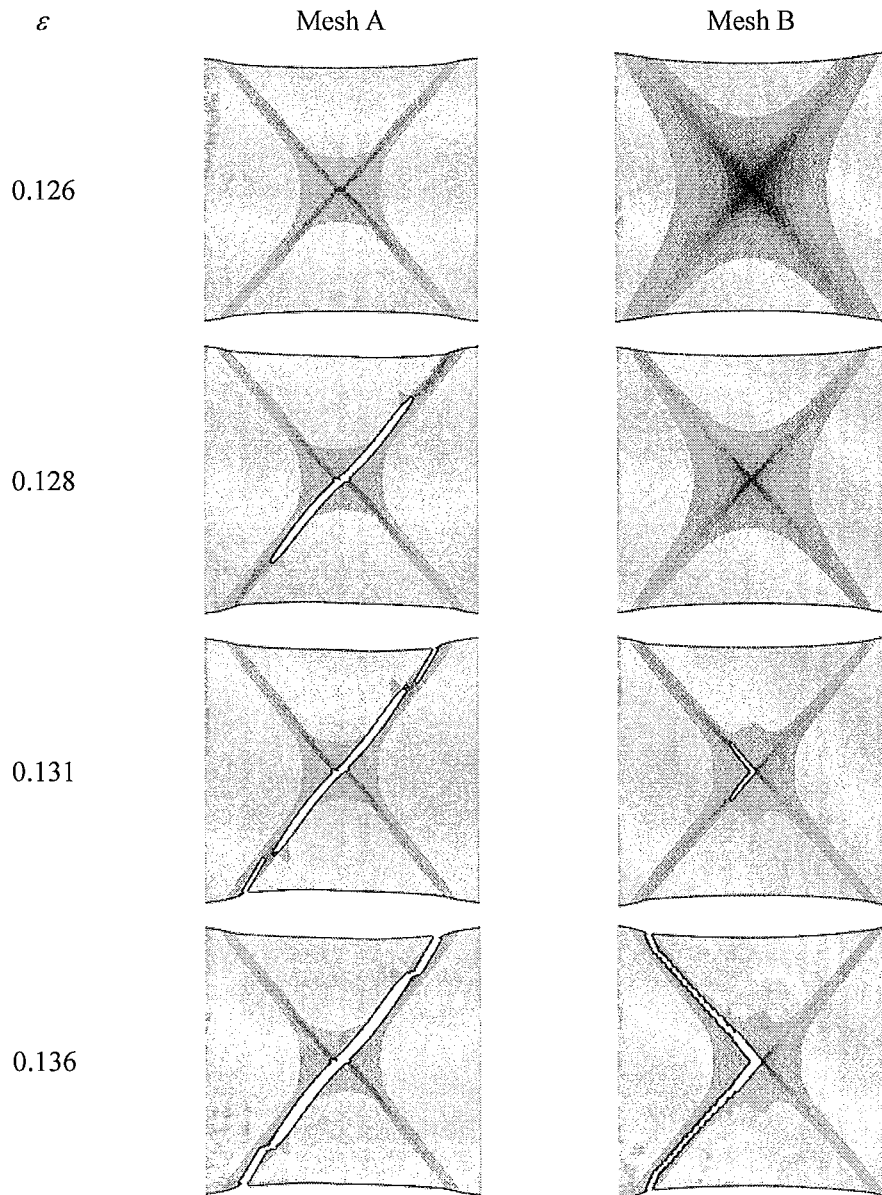


Figure 5.6: Predicted crack evolution of monolayer sheet by using Mesh A and Mesh B under atmospheric pressure  $p = 0$ .

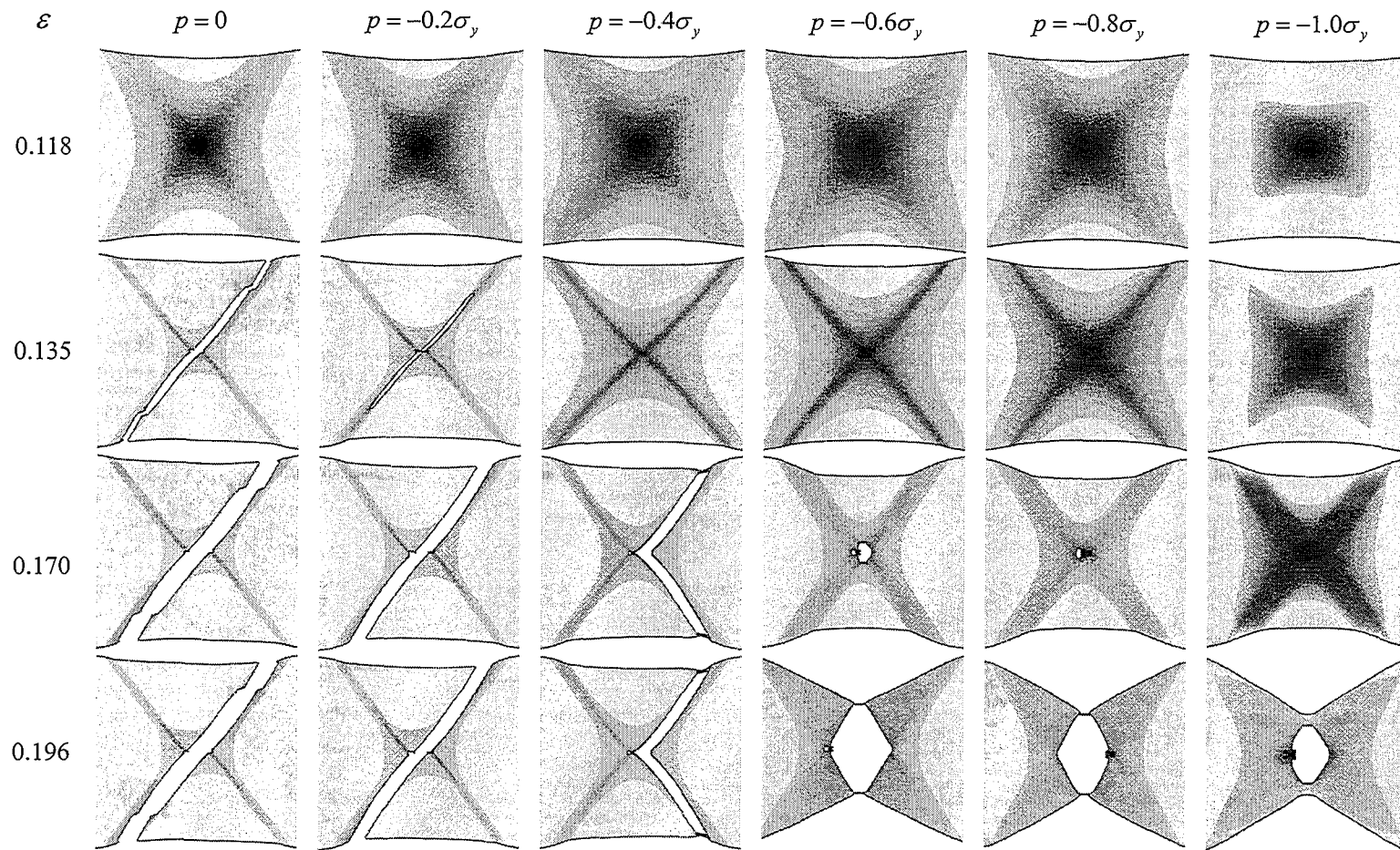


Figure 5.7: Predicted crack evolution of monolayer sheet by using Mesh A under various superimposed hydrostatic pressure

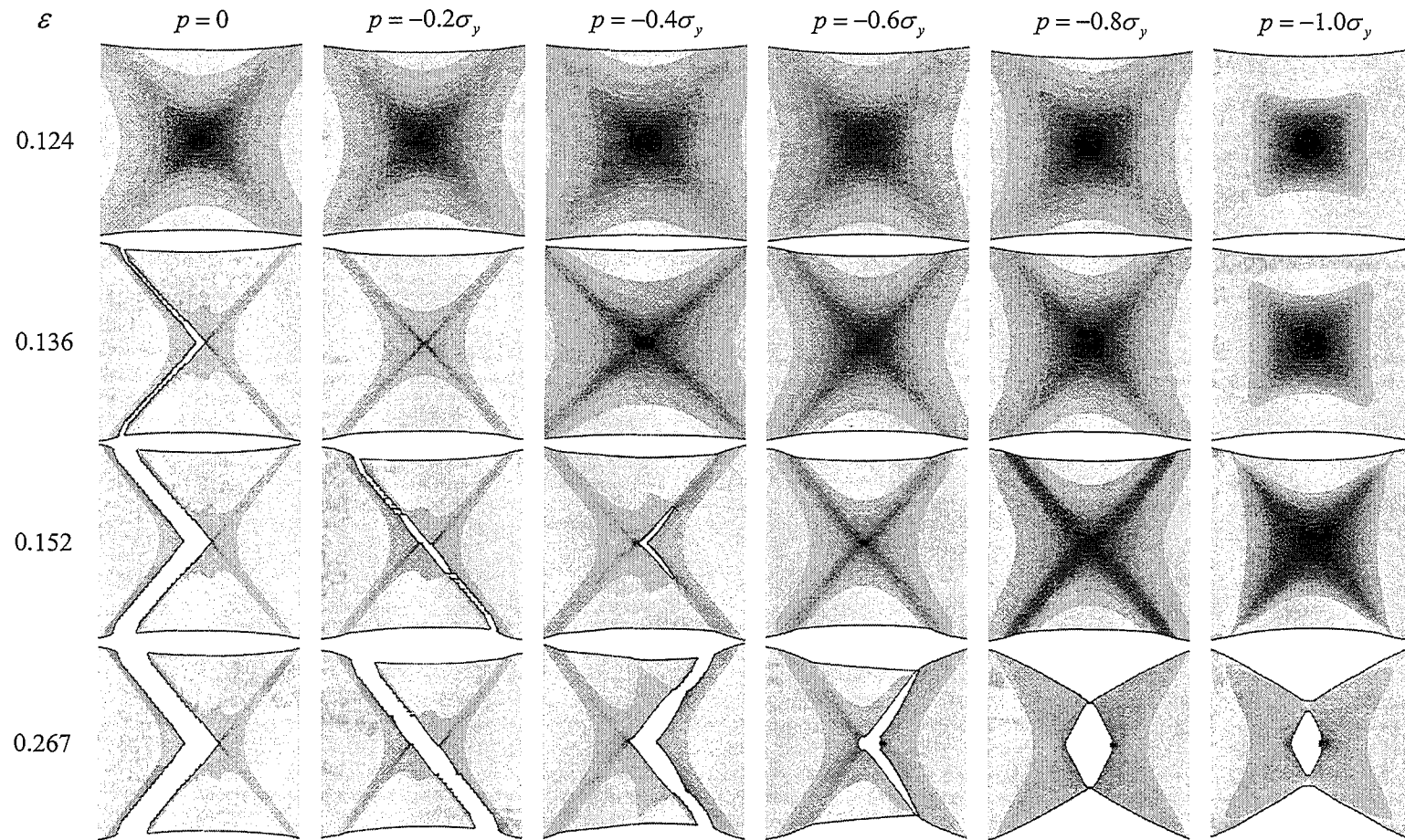


Figure 5.8: Predicted crack evolution of monolayer sheet by using Mesh B under various superimposed hydrostatic pressure

It is presented by Gimple et al. (2001) that extensive shear bands were observed within the necked region across the entire sample of low-Fe AA5754 at 298K under superimposed hydrostatic pressure 0.1MPa and 125MPa. In our numerical investigation, similar phenomenon was found that shear band is broadened under superimposed hydrostatic pressure (see Fig. 5.9). The presence of extensive shear bands or shear band broadening indicates that localization is delayed due to the effect of superimposed hydrostatic pressure.

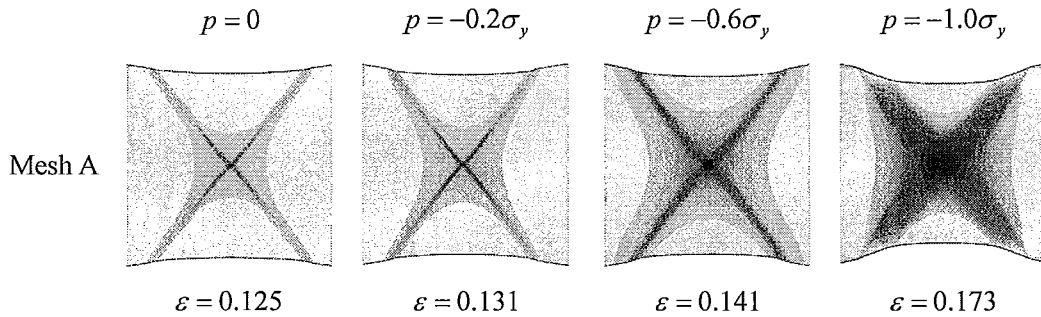


Figure 5.9: Predicted shear bands under various superimposed hydrostatic pressures before fracture by using Mesh A.

We continue to study the effects of superimposed hydrostatic pressure  $p = -\alpha\sigma_y$  on fracture in the tensile sheets. Fig. 5.10 shows the normalized applied/measured tensile force  $F^*$  versus tensile strain  $\varepsilon$  curve. They are calculated by summation of the reaction forces at  $X = 0$  or  $X = L_0$ . From Fig. 5.10, it is found that the hydrostatic pressure does not affect the maximum applied force point (the magnitude of the maximum force and the strain at which the maximum force is reached). However, the hydrostatic pressure clearly delays the sharp knee on the applied force versus tensile strain curve, and the sharpness of the knee reduces significantly with increasing hydrostatic pressure. At a higher pressure  $p = -\sigma_y$ , the knee disappeared and the applied force decreases gradually to zero. Also from Fig. 5.10, it seems that the hydrostatic pressure has no noticeable effect on necking but only affects the deformation behavior after necking has started. As mentioned

previously, the development of necking and failure can be very effectively assessed in terms of the calculated normalized minimum cross-sectional area versus tensile strain curve, which is now presented in Fig. 5.11. In the figure, the open circles represent the fracture initiation, while the open triangles indicate the completion of the fracture. It is found that the reduction in area at completed failure increases significantly with increasing hydrostatic pressure. It is noted that without superimposed hydrostatic pressure fracture initiates at 0.129 and the failure process is completed at 0.136. Under the hydrostatic pressures  $\alpha = 0.4, 0.6$ , these numbers become 0.145, 0.167 and 0.168, 0.189, respectively. Therefore, the superimposed hydrostatic pressure not only delays the initiation of crack but also extends the failure process (from initiation of crack to completely fracture).

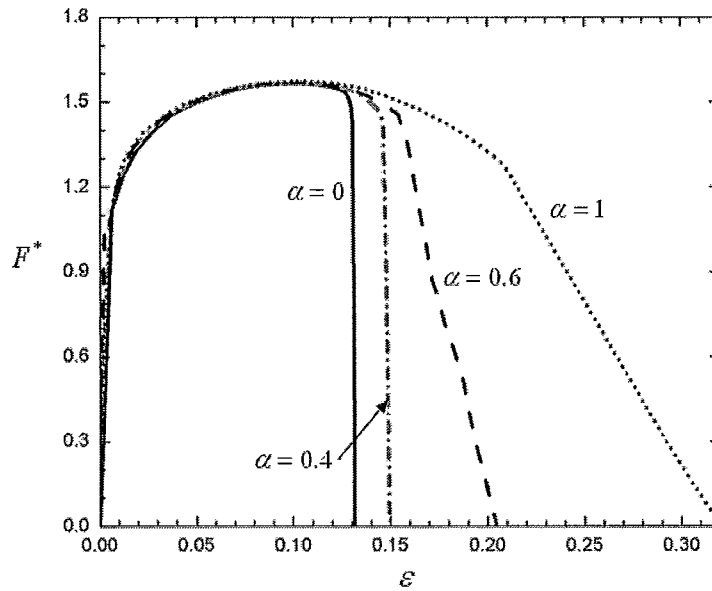


Figure 5.10: Predicted normalized applied force  $F^* = F/(\sigma_y A_0)$  and tensile strain  $\varepsilon = \ln(1 + \Delta L/L_0)$  curves for monolayer sheet under superimposed hydrostatic pressure  $p = -\alpha\sigma_y$ , by using Mesh B.

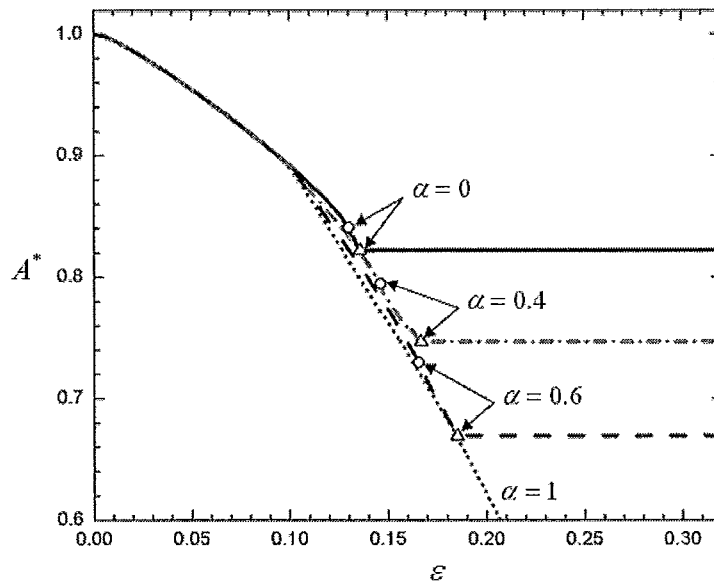


Figure 5.11: Predicted normalized minimum area  $A^* = A_{min}/A_0$  and tensile strain  $\varepsilon = \ln(1 + \Delta L/L_0)$  curves for monolayer sheet under superimposed hydrostatic pressure  $p = -\alpha\sigma_y$ , by using Mesh B.

Figure 5.12 presents the hydrostatic/ triaxial stress  $\sigma_H = \frac{1}{3}(\sigma_{11} + \sigma_{22} + \sigma_{33})$  at the centre of the neck, where fracture initiates, as a function of tensile strain  $\varepsilon$  at atmospheric pressure  $p = 0$  and superimposed hydrostatic pressure  $p = -0.4\sigma_y$  and  $p = -\sigma_y$ . During tensile deformation at room pressure  $p = 0$ , the triaxial tensile stress developed in the centre of neck is such as to assist the void growth. However, under a superimposed hydrostatic pressure  $p = -\alpha\sigma_y$ , the triaxial stress  $\sigma_H$  is initially compressive ( $\sigma_H = p = -\alpha\sigma_y$ ). This implies that void nucleation is delayed until a sufficiently large tensile component of stress is introduced. Fig. 5.13 shows the predicted void volume fraction  $f$  at the centre of the neck under various superimposed hydrostatic pressures. It is clear that a superimposed pressure delays or could even completely eliminate the nucleation, growth and coalescence of voids. In Fig. 5.14, under superimposed hydrostatic pressure  $p = -2\sigma_y$ , void nucleation was not observed until sufficient large plastic deformation  $\varepsilon = 0.332$ . Therefore, it is concluded that superimposed hydrostatic pressure suppress void nucleation and void growth which in reality increases material's ductility.



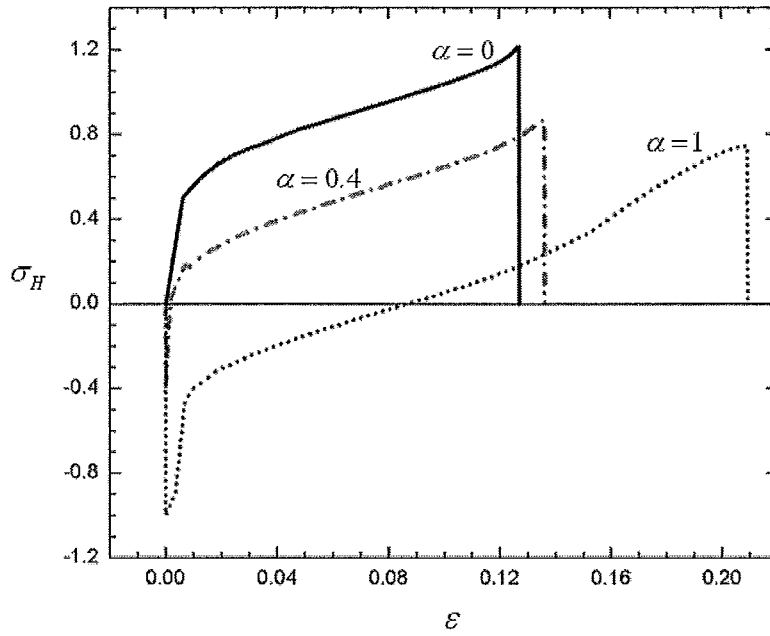


Figure 5.12: Predicted hydrostatic stress  $\sigma_H$  at the centre of the neck under superimposed hydrostatic pressure  $p = -\alpha\sigma_y$  by using Mesh B.

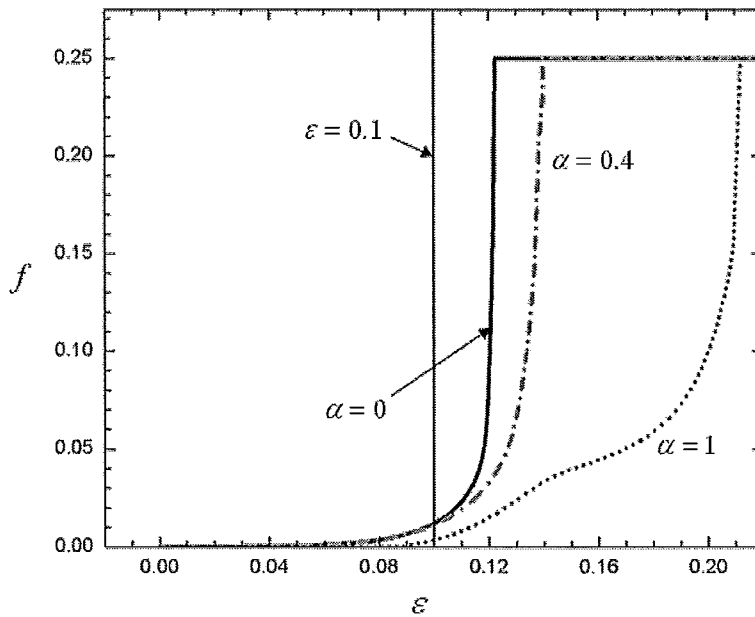


Figure 5.13: Predicted void volume fraction  $f$  at the centre of the neck under superimposed hydrostatic pressure  $p = -\alpha\sigma_y$  by using Mesh B.

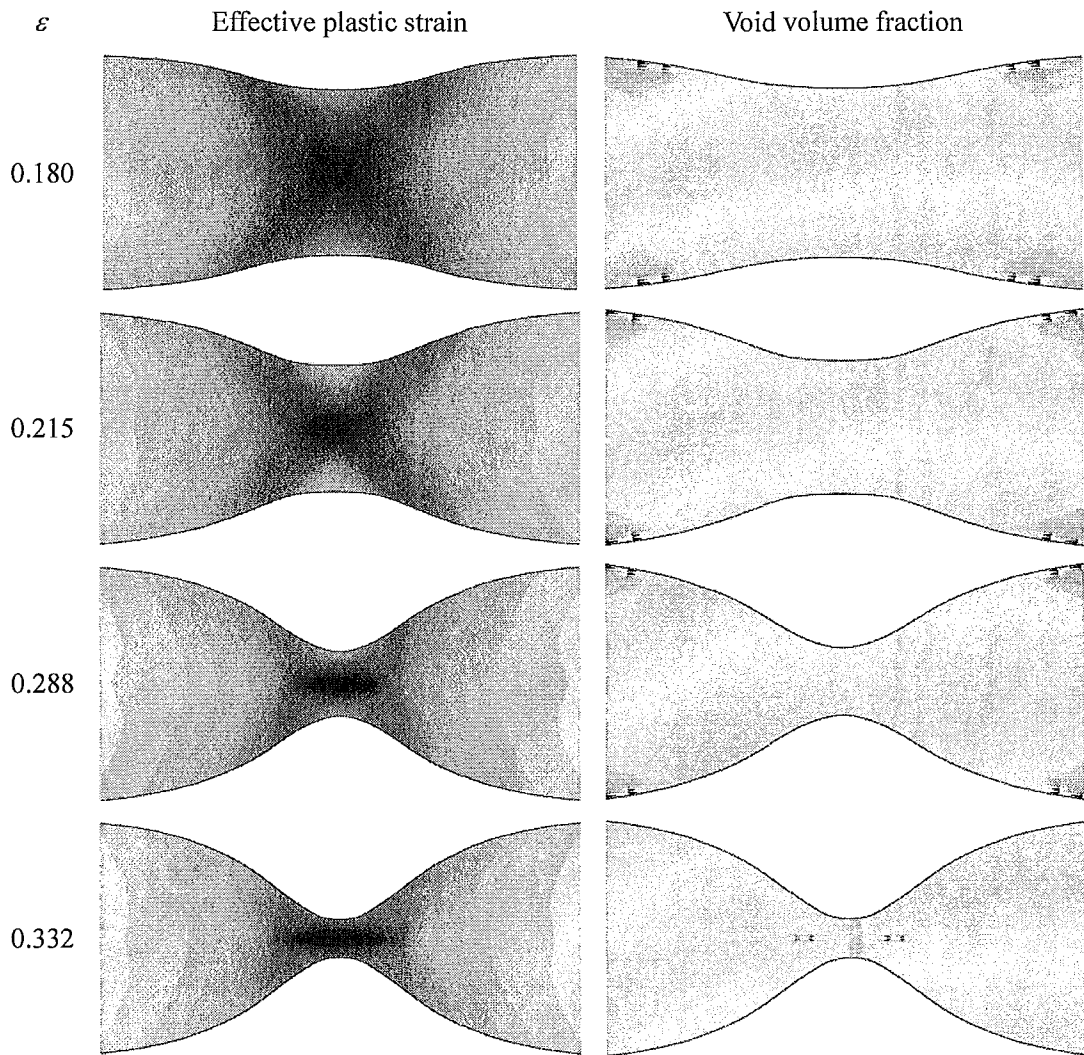


Figure 5.14: Predicted contour plots of effective plastic strain and void volume fraction by using Mesh A.

Figure 5.15 presents the calculated effect of superimposed hydrostatic pressure on the fracture strain. The fracture strain is defined as  $\varepsilon_f = \ln(A_0/A_f)$ , where  $A_0$  is the initial cross-sectional area and  $A_f$  is the minimum cross-sectional at fracture. It is found that the fracture strain  $\varepsilon_f$  increases with pressure almost linearly at low pressures but at an increasing rate at high pressures. Also, it is noted that at low pressure, the predicted fracture strain by Mesh A and Mesh B are almost identical. However, at high pressures the results based on Mesh A are not acceptable because the elements in the centre of the neck are distorted significantly at fracture initiation.

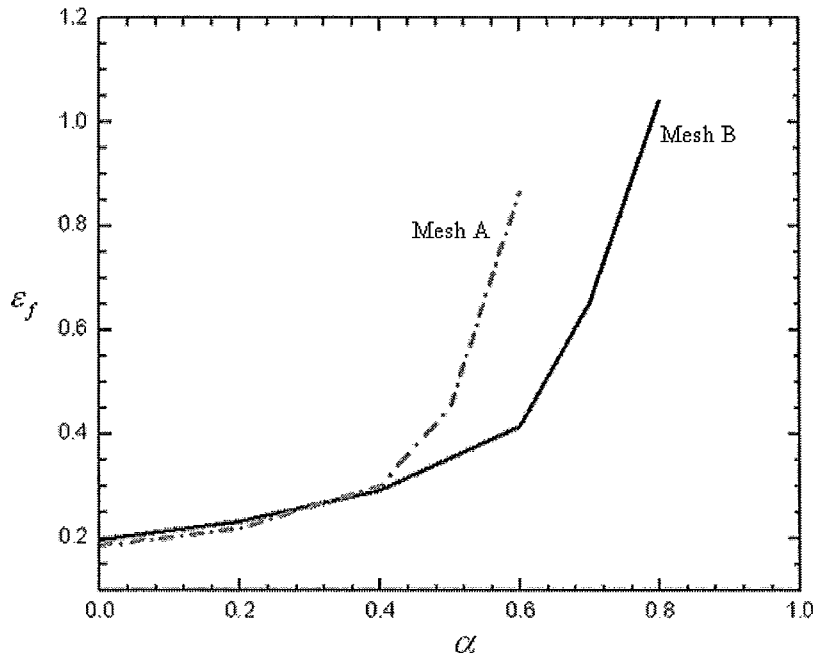


Figure 5.15: Predicted effect of superimposed hydrostatic pressure  $p = -\alpha\sigma_y$  on fracture strain  $\varepsilon_f$ .

Figure 5.16 presents the uniform or necking strain  $\varepsilon_u$  versus superimposed hydrostatic pressure. It shows that superimposed hydrostatic pressure has no significant effect on necking, which has been documented for most monolithic metals [Lewandowski and Lowhaphandu (1998)]. The uniform strain is the strain at which diffuse necking is initiated.

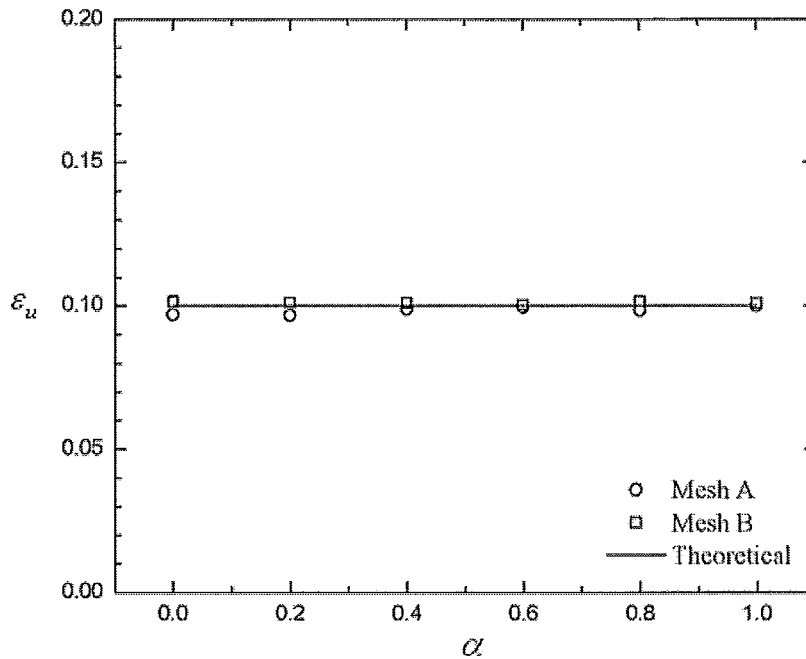


Figure 5.16: Predicted uniform strain under various superimposed hydrostatic pressure  $p = -\alpha\sigma_y$ .

#### 5.4 Summary

In this chapter, we have carried out a detailed finite element analysis of plane strain tensile sheets under superimposed hydrostatic pressure. It has been demonstrated that a superimposed hydrostatic pressure has no noticeable effect on necking because significant void growth has not occurred prior to necking, while the superimposed hydrostatic pressure significantly increases the fracture strain. The conclusion of the enhancement in ductility is due to the fact that superimposed hydrostatic pressure delays or completely eliminates the nucleation, growth and coalescence of microvoids or microcracks.

## **Chapter 6 Conclusions and future work**

The objective of this study is to carry out detailed numerical investigations on how cladding and superimposed hydrostatic pressure affect necking and fracture responses in round bars and metal sheets under tension.

It has been demonstrated that cladding increases both the necking strain and the fracture strain. The increase in necking strain has been found to be due to the fact that cladding enhances the overall work hardening for the layered round bars or metal sheets according to the rule of mixtures. Furthermore, the increase in necking strain delays the void nucleation and growth, and which in turn results in a significantly enhancement in ductility. Topological arrangement of cladding is found have no noticeable effect on necking but significantly increases the fracture strain.

Superimposed hydrostatic pressure has no noticeable effect on necking but significantly increases the fracture strain. Superimposed hydrostatic pressure enhances material's ductility due to the fact that superimposed hydrostatic pressure delays or completely eliminates the nucleation, growth and coalescence of microvoids or microcracks.

For future work, we are going to investigate the effects of superimposed hydrostatic pressure as well as cladding on fracture under bending. More realistic values of the material constants for describing hardening and Gurson model will be used in these simulations.

## BIBLIOGRAPHY

- ABARE. <http://www.abare.gov.au>
- ABAQUS/Explicit User's Manual, Version 6.5, 2005. ABAQUS Inc., Providence, Rhode Island, USA
- Alexander, D.J., Bernstein, I.M., 1987. Microstructural control of flow and fracture in pearlitic steels. *Metall. Trans.A* 20A, 2321-2335.
- Anderson, M.D., Kubo, K.T., Bischoff, T.F., Fenton, W.J., Reeves, E.W., Spendlove, B., Wagstaff, R.B., 2005. Method for casting composite ingot. US Patent Filing 20050011630.
- Ashby, M.F., J.D. Embury, Cooksley, S.H., Teirlinck, D., 1985. Fracture maps with pressure as a variable. *Scripta Metall.* 19, 385-390.
- ASM Handbook, 1987. Vol. 13, 887-890; 1993. Vol. 6, 961-963.
- Bao, Y., Wierzbicki, T., 2004. On fracture locus in the equivalent strain and stress triaxiality space. *Int. J. Mech. Sci.* 46, 81-98.
- Barsoum, I., Faleskog, J., 2007a. Rupture in combined tension and shear: Experiments. *Int. J. Solids Structure Sci.* 44, 1768-1786.
- Barsoum, I., Faleskog, J., 2007b. Rupture in combined tension and shear: Micromechanics. *Int. J. Solids Structure Sci.* 44, 5481-5498.
- Besson, J., Steglich, D., Brocks, W., 2001. Modeling of crack growth in round bars and plane strain specimens. *Int. J. Solids Structures* 38, 8259-8284.
- Botelho, E.C., Silva, R.A., Pardini, L.C., Rezende, M.C., 2006. A review on the development and properties of continuous fiber epoxy aluminum hybrid composites for aircraft structures. *Mater. Res.* 9, 247-256.
- Bouaziz, O., Brechet, Y., Embury, J.D., 2008. Heterogeneous and architected materials: A possible strategy for design of structural materials. *Adv. Eng. Mat.* 10, 24-36.
- Bridgman, P.W., 1952. *Studies in Large Plastic Flow and Fracture – With Special Emphasis on the Effects of Hydrostatic Pressure*, New York, McGraw-Hill.
- Brown, L.M., Embury, J.D., 1973. The initiation and growth of voids at second phase particles. In *Proceeding of the Third International Conference of the Strength of Metals and Alloys* 1, 164-169.
- Brownrigg, A., Spitzig, W.A., Richmond, O., Teirlinck, D., Embury, J.D., 1983. The influence of hydrostatic pressure on the flow stress and ductility of a spheroidized 1045 steel. *Acta Metall.* 31, 1141-1150.
- Carpentier, D., Contre, M., 1970. Description of an apparatus allowing mechanical tests under hydrostatic pressure up to 15 kilobars. *Rev. Sci. Instr.* 41, 189-192.
- Chen, A.Y., Zhang, J.B., Lu, J., Lun, W., Song, H.W., 2007. Necking propagated deformation behaviour of layer-structured steel prepared by co-warm rolled

- surface nanocrystallized 304 stainless steel. *Mater. Letters* 61, 5191-5193.
- Chen, B., Huang, Y., Liu, C., Wu, P.D., MacEwen, S.R., 2004. A dilatational plasticity theory for viscoplastic materials. *Mech. Mater.* 36, 679-689.
- Chen, L.C., Yang, Z.G., Jha, B.J., Xia, G.G., Stevenson, J.W., 2005. Clad metals, roll bonding and their applications for SOFC interconnects. *J. Power Sources* 152, 40-45.
- Chen, X.X., Wu, P.D., Embury, J.D., Huang, Y.G., 2009. Enhanced ductility in round tensile bars by cladding a ductile ring. *Int. J. Solids Structures* (submitted).
- Chu, C.C., Needleman, A., 1980. Void nucleation effects in biaxially stretched sheets. *J. Eng. Mater. Technol.* 102, 249-256.
- Dietz, A.G.H., 1969. *Composite engineering laminates*. Book, MIT Press.
- Feucht, M., Sun, D.Z., Erhart, T., Frank, T., 2006. Recent development and applications of the Gurson model. *LS-DYNA Anwender Forum*, Ulm.
- Fleck, N.A., Hutchinson, J.W., Tvergaard, V., 1989. Softening by void nucleation and growth in tension and shear. *J. Mech. Phys. Solids*. 37, 515-540.
- French, L.E., Weinrich, P.F., 1973. The effect of hydrostatic pressure on the tensile fracture of  $\alpha$ -brass. *Acta Metall.* 21, 1533-1537.
- French, L.E., Weinrich, P.F., 1975. The influence of hydrostatic pressure on the tensile deformation and fracture of Copper. *Metall. Trans. A* 6A, 785-790.
- French, L.E., Weinrich, P.F., 1977. The tensile fracture mechanisms of FCC metals and alloys – A review of the influence of pressure. *J. Aust. Inst. Met.* 22, 40-50.
- French, L.E., Weinrich, P.F., Weaver, C.W., 1973. Tensile fracture of free machining Brass as a function of hydrostatic pressure. *Acta Metall.* 21, 1045-1049.
- Gimple, J.L., 2001. MASC Thesis. Materials Science and Engineering. McMaster University.
- Gimple, J.L., Wilkinson, D.S., Embury, J.D., Lewandowski, J.J., 2001. Effect of Superimposed Pressure on the Fracture Behaviour of Aluminum Automotive Alloys. In: Das, S.K., Kaufman, J.G., Lienert, T.J. (Eds.), *Aluminum 2001- Proceedings of the TMS 2001*, TMS, 2001, pp. 17-29.
- Gologanu, M., Leblond, J.B., Perrin, G., Devaux, J., 1997. Recent extensions of Gurson's model for porous ductile metals. *Continuum Micromechanics, CISM Courses and Lectures No. 377*, 61-130.
- Goods, S.H., Brown, L.M., 1979. The nucleation of cavities by plastic deformation. *Acta Metall.* 27, 1-15.
- Gurson, A., 1977. Continuum theory of ductile rupture by void nucleation and growth. Part I-Yield criteria and flow rules for porous ductile media. *J. Eng. Mater. Technol.* – T. ASME 99, 2-15.
- Hu, L.W., 1956. An experimental study on the fracture of metals under hydrostatic pressure. *J. Mech. Phys. Solids* 4, 96-103.
- Huang, Y., Hutchinson, J.W., Tvergaard, V., 1991. Cavitation instabilities in elastic

- plastic solids. *J. Mech. Phys. Solids* 39, 223-241.
- Jimenez, J.A., Ruano, O.A., Smirnov, O.M., Sherby, O.D., 1991. Microstructural studies of a roll-bonded laminated ultrahigh carbon steel bar. *Mater. Charact. (UK)* 27, 141-145.
- Johnson, G.R., Cook, W.H., 1985. Fracture characteristics of three metals subjected to various strains, strain rates, temperature and pressures. *Eng. Fract. Mech.* 21, 31-48.
- Kao, A.S., Kuhn, H.A., Richmond, O., Spitzig, W.A., 1989. Workability of 1045 spheroidized steel under superimposed hydrostatic pressure. *Metall. Trans. A* 20A, 1735-1741.
- Kao, A.S., Kuhn, H.A., Richmond, O., Spitzig, W.A., 1990. Tensile fracture and fractographic analysis of 1045 spheroidized steel under hydrostatic pressure. *J. Mater. Res.* 5, 83-91.
- Kim, J.K., Yu, T.X., 1997. Forming and failure behaviour of coated, laminated and sandwiched sheet metals: a review. *J. Mater. Process. Technol.* 63, 33-42.
- Kim, K.J., Kim, D., Choi, S.H., Chung, K., Shin, K.S., Barlat, F., Oh, K.H., Youn, J.R., 2003. Formability of AA5182/polypropylene/AA5182 sandwich sheets. *J. Mater. Processing Technology* 139, 1-7.
- Koplik, J., Needleman, A., 1988. Void growth and coalescence in porous plastic solids. *Int. J. Solids Struct.* 24, 835-853
- Korbel, A., Raghunathan, V.S., Teirlinck, D., Spitzig, W.A., Richmond, O., Embury, J.D., 1984. A structural study of the influence of pressure on shear band formation. *Acta Metall.* 32, 511-519.
- Kum, D.W., Oyama, T., Wadsworth, J., Sherby, O.D., 1983. The impact properties of laminated composites containing ultrahigh carbon (UHC) steels. *J. Mech. Phys. Solids* 31, 173-186.
- Le Roy, G., Embury, J.D., Edwards, G., Ashby, M.F., 1981. A model of ductile fracture based on the nucleation and growth of voids. *Acta Metall.* 29, 1509-1522.
- Lesuer, D.R., Syn, C.K., Sherby, O.D., Wadsworth, J., Lewandowski, J.J., Hunt, W.H. Jr., 1996. Mechanical behaviour of laminated metal composites. *Int. Mater. Reviews* 41, 169-197.
- Lesuer, D.R., Syn, C.K., Wadsworth, J.D., Sherby, O.D., 2002. Flow stresses in metal laminates and pure metals during high temperature extrusion. *Int. J. Plasticity* 18, 155-184.
- Lewandowski, J.J., Lowhaphandu, P., 1998. Effects of hydrostatic pressure on mechanical behaviour and deformation processing of materials. *Int. Mater. Reviews* 43, 145-187.
- Li, T., Suo, Z., 2006. Deformability of thin metal films on elastomer substrates. *Int. J. Solids Structures* 43, 2351-2363.
- Liu, D.S., Lewandowski, J.J., 1993. The effects of superimposed hydrostatic pressure on deformation and fracture: Part I. Monolithic 6061 Aluminum. *Metall. Trans. A*



- 24A, 601-608.
- Manoharan, M., Ellis, L., Lewandowski, J.J., 1990. Laminated composites with improved toughness. *Scripta Metall. Mater.*, 24, 1515-1519.
- McClintock, F.A., 1968. A criterion for ductile fracture by growth of holes. *J. Appl. Mech.* – T. ASME 35, 363-371.
- McClintock, F.A., Kaplan, S.M., Berg, C.A., 1966. Ductile fracture by hole growth in shear bands. *Int. J. Fract.* 2, 614-627.
- Mear, M.E., Hutchinson, J.W., 1985. Influence of yield surface curvature on flow localization in dilatant plasticity. *Mech. Mater.* 4, 395-407.
- Nahshon, K., Hutchinson, J.W., 2008. Modification of the Gurson model for shear failure. *Eur. J. Mech. A/Solids* 27, 1–17.
- Nahshon, K., Xue, Z., 2009. A modified Gurson model and its application to punch-out experiments. *Eng. Fract. Mech.* (in press).
- Pardoen, T., Hutchinson, J.W., 2000. An extended model for void growth and coalescence. *J. Mech. Phys. Solids* 48, 2467-2512.
- Peng, J., Wu, P.D., Huang, Y., Chen, X.X., Lloyd, D.J., Embury, J.D., Neale, K.W., 2009. Effects of superimposed hydrostatic pressure on fracture in round bars under tension. *Int. J. Solids Structures* (submitted).
- Prat, F., Besson, J., Grange, M., Andrieu, E., 1998. Behavior and rupture of hydrided ZIRCALOY-4 tubes and sheets. *Metall. Mater. Trans.* – A 29, 1643-1651.
- Pugh, H.L.D., Green, D., 1964. The effect of hydrostatic pressure on the plastic flow and fracture of metals. *Proc. Inst. Mech. Eng.*, 179, 415-437.
- Ragab, A.R., 2004. A model for ductile fracture based on internal necking of spheroidal voids. *Acta Mater.* 52, 3997-4009.
- Rice, J.R., Tracey, D.M., 1969. On the ductile enlargement of voids in triaxial stress fields. *J. Mech. Phys. Solids* 17, 201-217.
- Ritchie, R.O., 1988. Mechanisms of fatigue crack-propagation in metals, ceramics and composites – role of crack tip shielding. *Mater. Sci. Eng. A103*, 15-28.
- Sauer, J.A., Mears, D.R., Pae, K.D., 1970. Effects of hydrostatic pressure on the mechanical behaviour of Polytetrafluoroethylene and Polycarbonate. *European Polymer Journal* 6, 1015-1032.
- Semiatin, S.L., Pichler, H.R., 1979a. Deformation of sandwich sheet materials in uniaxial tension. *Metall. Trans.* 10A, 85-96.
- Semiatin, S.L., Pichler, H.R., 1979b. Formability of sandwich sheet materials in plane strain compression and rolling. *Metall. Trans.* 10A, 97-107.
- Spitzig, W.A., Richmond, O., 1984. The effect of pressure on the flow stress of metals. *Acta Metall.* 32, 457-463.
- Sturgell, B.W., 2006. Breaking the barriers: Unlocking new possibilities for aluminum. Handouts, CRU 11th world aluminum conference.

- Thomason, P.F., 1990. Ductile fracture of metals. Oxford: Pergamon.
- Tvergaard, V., 1981. Influence of voids on shear band instabilities under plane strain conditions. *Int. J. Fract.* 17, 237-252.
- Tvergaard, V., 1982. Influence of void nucleation on ductile shear fracture at a free surface. *J. Mech. Phys. Solids* 30, 399-425.
- Tvergaard, V., 1982. On localization in ductile materials containing spherical voids. *Int. J. Fract.* 18, 389-407.
- Tvergaard, V., 1990. Material failure by void growth to coalescence. *Adv. Appl. Mech.* 27, 83-151.
- Tvergaard, V., Needleman, A., 1984. Analysis of the cup-cone fracture in a round tensile bar. *Acta Metall.* 32, 157-169.
- Vermeeren, C.A.G.H., 2003. An historic overview of the development of fibre metal laminates. *Appl. Compos. Mater.* 10, 189-205.
- Wadsworth, J., Lesuer, D.R., 2000. Ancient and modern laminated composites — from the Great Pyramid of Gizeh to Y2K. *Materials Characterization* 45, 289-313.
- Wagstaff, R.B., Lloyd, D.J., Bischoff, T.F., 2006. Direct chill casting of CLAD ingot. *Materials Science Forum* 519-521, 1809-1814.
- Weck, A., Wilkinson, D.S., Hiroyuki, T., Maire, E., 2006. 2D and 3D Visualization of Ductile Fracture. *Adv. Eng. Mater.* 8, 469-472.
- Weinrich, P.F., French, L.E., 1976. The influence of hydrostatic pressure on the fracture mechanisms of sheet tensile specimens of Copper and Brass. *Acta Metall.* 24, 317-322.
- Wen, J., Huang, Y., Hwang, K.C., Liu, C., Li, M., 2004. The modified Gurson model accounting for the void size effect. *Int. J. Plast.* 21, 381-395.
- Wikipedia, 2001. Wikipedia Foundation. [www.wikipedia.org](http://www.wikipedia.org)
- Wilkins, M.L., Streit, R.D., Reaugh, J.E., 1980. Cumulative-strain-damage model of ductile fracture: Simulation and prediction of engineering fracture tests. Technical Report UCRL-53058, Lawrence Livermore National Laboratory.
- Wu, C.W., Hsu, R.Q., 1999. Theoretical analysis of extrusion of rectangular, hexagonal and octagonal composite clad rods. *Int. J. Mech. Sci.* 42, 473-486.
- Wu, P.D., Chen, X.X., Lloyd, D.J., Embury, J.D., 2009. Effects of superimposed hydrostatic pressure on fracture in sheet metals under tension. *Int. J. Mech. Sci.* (submitted).
- Wu, P.D., Embury, J.D., Lloyd, D.J., Huang, Y., Neale, K.W., 2009. Effects of superimposed hydrostatic pressure on sheet metal formability. *Int. J. Plasticity* (in press).
- Xue, L., 2007. Ductile fracture modeling - Theory, experimental investigation and numerical verification. Ph.D. thesis, Massachusetts Institute of Technology.
- Xue, L., 2008. Constitutive modeling of void shearing effect in ductile fracture of

porous materials. *Eng. Fract. Mech.* 75, 3343-3366.

Xue, Z., Hutchinson, J.W., 2007. Neck retardation and enhanced energy absorption in metal-elastomer bilayers. *Mech. Mater.* 39, 473-487.

Zhang, Z.L., Thaulow, J., Ødegård 2001. A complete Gurson model approach for ductile fracture. *Eng. Fract. Mech.* 67, 155-168.